UNIVERSITY OF CALIFORNIA,
IRVINE

Single molecules at plasmonic nanojunctions interrogated through space, time and frequency domain Raman scattering

DISSERTATION

submitted in partial satisfaction of the requirements
for the degree of

DOCTOR OF PHILOSOPHY

in Chemistry

by

Kevin T. Crampton

Dissertation Committee:
Professor V. Ara Apkarian, Chair
Professor Eric O. Potma
Professor Robert M. Corn

2018

DEDICATION

To my family.

TABLE OF CONTENTS

LIST OF FIGURES

Page

LIST OF TABLES

Page

ACKNOWLEDGMENTS

I would like to express my sincere gratitude to my research advisor and dissertation committee chair, Prof. V. Ara Apkarian for his resolute dedication to my graduate research and pedagogical development. I am continuously inspired by his unwavering drive and capacity to pursue physics and chemistry at the frontier.

I thank my dissertation committee members for their contributions to this work, especially Prof. Eric O. Potma, who has made a significant investment in helping me convert scientific observations into wisdom. I thank Dr. Dmitry Fishman for taking an early interest in my development, both personally and professionally. He has shown me that science is equal parts knowledge and humility and for that I am very grateful. I thank Dr. Steven Yampolsky for guiding me into the realm of non-linear optics and for his continued friendship. I thank my colleagues-turned-friends Dr. Elizabeth Foreman and Dr. Alexander Fast for their support in my graduate studies and beyond.

I thank all of my colleagues and friends at UCI and elsewhere, many of which have made direct contributions to this work including Dr. Joonhee Lee, Dr. Mayukh Banik, Dr. Aram Zeytunyan, Dr. Faezah Tork Ladani and Dr. Alba Alfonso-Garcia.

I gratefully acknowledge the support of the National Science Foundation through the Center for Chemistry at the Space-Time Limit (Award #: CHE-1414466) for funding this research in its entirety. I also acknowledge the skillful assistance of the staff at the UC Irvine Materials Research Institute for their aid in electron microscopy experiments. I would like to thank the American Chemical Society and the Optical Society of America for allowing me to incorporate my published work in this dissertation.

With much enthusiasm, I thank Bryan Solem for his love, support, and patience. I thank all that have made graduate life a pleasure especially my dear friends Paulina Temple Yampolsky and Yulia Davydova.

Finally, I owe a debt of gratitude to my family for their unwavering support of my endeavors in science and in life. I thank my parents, Jim and Kate, my siblings Matt, and Dan, and Jamie, their children and my siblings-in-law, Krisi and Stephanie for believing in me at every turn and for their selfless support. Last, but certainly not least, I thank my grandmother Barbara, who has been a constant inspiration; you have made so many things in my life possible and I am forever grateful to be your grandson.

CURRICULUM VITAE

Education

Ph.D in Chemistry — March 2018
University of California Irvine, Irvine, CA 92697
Research Advisor: V. Ara Apkarian

B.Sc. in Chemistry – ACS Certified — December 2011
Wayne State University, Detroit, MI 48202
Senior Research: "Protonation Preferentially Stabilizes Minor Tautomers of the Halouracils: IRMPD Action Spectroscopy and Theoretical Studies"
Senior Research Advisor: Professor Mary T. Rodgers

Publications

4. **Crampton, K. T.**, Zeytunyan, A., Fast, A. S., Ladani, F. T., Alfonso-Garcia, A.,Banik, M., Fishman, D. A., Potma, E. O., Apkarian, V. A. Spontaneous and coherent Raman scattering at plasmonic nanojunctions. *J. Phys. Chem. C Richard P. Van Duyne Festschrift* **37**, 20943-20953 (2016).

3. Zeytunyan, A., **Crampton, K. T.**, Zadoyan, R., Apkarian, V. A. Supercontinuum based 3 color 3 pulse coherent anti-Stokes Raman scattering. *Opt. Express* **23**, 24019-24028 (2015).

2. Nei, Y., **Crampton, K. T.**, Berden, G., Oomens, J., Rodgers, M. T. Infrared multiple photon dissociation action spectroscopy of deprotonated RNA mononucleotides: gas-phase conformations and energetics. *J. Phys. Chem. A* **117,** 10634–49 (2013).

1. **Crampton**, **K. T.**, Rathur, A. I., Nei, Y.-w., Berden, G., Oomens, J., Rodgers, M. T. Protonation preferentially stabilizes minor tautomers of the halouracils: IRMPD action spectroscopy and theoretical studies. *J. Am. Soc. Mass Spectrom.* **9**, 1469-78 (2012).

Oral Presentations

2. **Crampton, K. T.**, Fast, A., Ladani, F. T., Potma, E. O., Apkarian, V. A. "Photons and Electrons at conductive and capacitive plasmonic nano-junctions", The 47th Winter Colloquium on the Physics of Quantum Electronics, Snowbird, UT, January 9th, 2016.

1. **Crampton, K.T.,** Zeytunyan, A., Fast, A., Garcia, A. A., Ladani, F. T., Fishman, D. A., Potma, E. O., Apkarian, V. A. "Towards time-resolved single molecule chemistry: probing plasmonic nanostructures with femtosecond light", The International Chemical Congress of the Pacific Basin Societies 2015, Honolulu, HI, December 18, 2015.

Poster Presentations

5. **Crampton, K. T.**, Zeytunyan, A., Fast, A. S., Ladani, F. T., Alfonso-Garcia, A., Banik, M., Fishman, D. A., Potma, E. O., Apkarian, V. A. "Ultrafast coherent Raman scattering at plasmonic nanojunctions", Ultrafast Dynamics at the Nanoscale, OIST, Okinawa, Japan, July 14, 2016.

4. **Crampton, K. T.**, Rathur, A. I., Nei, Y.-w., Berden, G., Oomens, J., Rodgers, M. T., "Infrared Multiple Photon Dissociation Spectroscopy of Protonated Halouracils: Gas Phase Conformation and Stability", Schaap Chemistry Symposium, Detroit, MI, September 17, 2011.

3. **Crampton, K. T.**, Nose, H., Rodgers, M. T., "Structures and Bond Dissociation Energies of Protonated and Sodium and Silver Cationized Complexes of 2,2′-Dipyridyl and 1,10-Phenanthroline'', 2011 Conference on Ion Chemistry and Mass Spectrometry, Lake Arrowhead, CA, January 14-16, 2011.

2. **Crampton, K. T.**, Nose, H., Rodgers, M. T., "Structures and Bond Dissociation Energies of Protonated and Sodium Cationized Complexes of 2,2′-Dipyridyl and 1,10-Phenanthroline'', 2010 Anachem/SAS Symposium, Livonia, MI, October 28, 2010.

1. **Crampton, K. T.**, Nose, H., Rodgers, M. T., "Structures and Bond Dissociation Energies of Protonated and Sodium Cationized Complexes of 2,2′-Dipyridyl and 1,10-Phenanthroline'', 12th Annual Wayne State University Chemistry Graduate Research Symposium, Detroit, MI, October 9, 2010.

Teaching Experience

Graduate Teaching Assistant — University of California Irvine, Irvine, CA 92697

CHEM 1LD: *General Chemistry Laboratory*	September 2013
CHEM 1B: *General Chemistry*	January 2013
CHEM 152: *Advanced Analytical Chemistry*	January 2014

Awards

- WSU Student Travel Fellowship to attend the 2011 Conference on Ion Chemistry and Mass Spectrometry, Lake Arrowhead, CA, January 14-16, 2011

- Phi Lambda Upsilon Undergraduate Research Award, 2012 Chemistry Honors Convocation, Wayne State University, Detroit, MI 48202

- MS-PIRE NSF Mass Spectrometry Partnership for International Research and Education Summer Fellowship, Wayne State University, Detroit, MI 48202, May 2 – August 16, 2012

ABSTRACT OF THE DISSERTATION

Single molecules at plasmonic nanojunctions interrogated through space, time and frequency domain Raman scattering

By

Kevin T. Crampton

Doctor of Philosophy in Chemistry

University of California, Irvine, 2018

Professor V. Ara Apkarian, Chair

Surface-enhanced vibrational spectroscopy has emerged as a powerful tool to probe the (photo)chemistry and (photo)physics of individual molecules, which may be regarded as the primary focus of the field of nanophotonics. Single molecule (SM) sensitivity relies on the excitation of localized surface plasmons which confine far-field radiation to molecular length scales, ultimately enabling submolecular imaging with chemical selectivity. Over the length scales that enable submolecular resolution, localized optical fields cannot be separated from the charge density oscillations that sustain them. As such, the interplay between plasmons, photons and electrons in plasmonic nano-junctions is of critical importance for the development of imaging modalities capable of circumventing the diffraction limit and, more generally, for gaining broader insight into the fundamental mechanisms of surface-enhanced Raman and tip-enhanced Raman scattering (SERS and TERS).

In what follows, the SM surface-enhanced parameter space is explored through linear and ultrafast optical measurements utilizing nanometer to ångstrom scale plasmonic junctions and non-resonant molecular reporters. SERS measurements carried out on the prototypical gold dimer nano-antenna highlight the interplay between the molecular Raman

scattering channel(s) and coherent luminescence of the plasmon itself. Ultrafast studies utilizing 100 femtosecond laser pulses establish the operating principles of the ultrafast analog of surface-enhanced spectroscopy, which are then utilized to demonstrated time and frequency resolved coherent Raman scattering (CRS) in the single molecule limit.

The fundamental mechanism of SERS is explored by replacing the continuous-wave excitation source with a picosecond pulse train, which probes the non-equilibrium population dynamics of SM phonon states. The latter are inferred through the observed inverted Stokes/anti-Stokes ratios and verified through stimulated and coherent Raman scattering (SRS and CARS) measurements carried out on the same system. Direct plasmon-molecule energy transfer is dominant over the optically induced and thermal contributions to the vibrational population.

Finally, SM TERS measurements utilizing a metalloporphyrin functionalized silver tip are carried out in ultrahigh vacuum and ultralow temperatures (5 K). These measurements directly image the atomic lattice of a copper nitride monolayer with 1.5 Å precision. A series of measurements recorded on this system highlight the essential role of photoelectrons in the TERS process.

INTRODUCTION

The first observations[1-2] of vibrational spectra emanating from single molecules may be considered the birth of the field of nanophotonics[3]. This development effectively accelerated the ongoing quest to exercise optical spectroscopy and microscopy beyond the limitations understood through diffraction theory. In what have become the interrelated fields of surface-enhanced Raman scattering (SERS) and tip-enhanced Raman scattering (TERS), single molecule vibrational spectroscopy relies on the mediation of surface plasmons. Surface plasmons mediate the interaction of far-field radiation and near-field matter through the collective motion of surface charge, which is provided by the nearly-free electrons of coinage metals. This coupling scheme effectively bridges the spatial mismatch between focused radiation ($\sim \lambda/2$ nm) and individual molecules (< 1 nm). In effect, this permits spectroscopic explorations on nanometeric, and in what will be presented here, atomic length scales.

Pioneering work over the past four decades has transformed the initial observations of single molecules (SM) through SERS into a robust spectroscopy capable of routine recognition of individual molecules[1-2, 4-13]. It is easy to show that the observation of a single, non-resonant molecule via Raman requires dramatic enhancement of the involved fields by factors on the order of $\beta = 10^2$ to 10^3, where β is the local field enhancement. Raman, as a second order optical process involves the interaction of four fields (incident and scattered waves and their complex conjugates)[14]. As such, the effect of the enhancement in SERS is twofold; by coupling to surface plasmon modes, incident radiation is localized to molecular dimensions, effectively increasing the photon density by a factor of β^2 beyond the vacuum density. The reciprocal process is also operative as excited molecules may couple to radiative

plasmon modes which broadcast molecular information into the far-field. The latter may be regarded as an effective increase in the molecule's spontaneous scattering cross section. This description captures the commonly quoted quartic dependence of the enhancement factor on the incident field. That is, $\beta = |E/E_0|^4$, where E is the local field and E_0 is the incident field[15-16].

Nanoscale plasmonic junctions, such as the gap between two metal spheres, provide the enhancement required to reach SM sensitivity in Raman[17-21]. The so-called dimer plasmonic nano-antenna (nantenna) represents a seminal prototype for the mechanistic description of the SERS effect given the lack of SERS activity on isolated spheres. The simplest model to account the large enhancements observed experimentally is rooted in electromagnetic theory[22-24]. The plasmon resonance(s) of single spheres couple when the gap between them is narrowed to $g_0 << D$, where g_0 is the vacuum gap and D is the diameter of the spheres. The bound sphere surface charge may be driven coherently, affording tight junction localization for D = 10 to 200 nm. The field inside the vacuum gap is then purely due to a displacement current which induces optical transitions in junction-localized molecules[25]. Indeed, this classical mechanism has been utilized extensively to rationalize SM sensitivity in SERS[16, 26-31]. With regard to the rational design of nantennas, the optical constants of the metal, parameters g_0 and D and the system symmetry are critical considerations that determine the location of the plasmon resonance(s) and the attainable field enhancement.

Significant detail regarding the characteristics of the local field may be gleaned from SERS spectra. The (frequency dependent) Raman cross section for a given scatterer depends on the orientation of the molecule relative to the local field through the transition

polarizability, α, which is a tensor quantity[32]. Generally, ensemble Raman spectra reflect an average over the orientations of all molecules present in the focal volume. From a computational standpoint, this is equivalent to fixing the vector local field and integrating α over all orientations. For SM's, this description is no longer appropriate and the tensorial nature of the Raman polarizability must be expressly considered[25, 33-37]. The local fields deduced from SM SERS signatures imply multipolar electric and magnetic fields and field gradients[25, 38-40]. These observations emphasize that junction fields vary on molecular length scales. In this limit, the concept of Raman based on the foregoing discussion of purely classical fields is inadequate. Moreover, the interpretation of fluctuating spectra in SERS, which is characteristic SM behavior, has identified operative chemical effects that contribute to the overall enhancement such as plasmon mediated metal-molecule or molecule-metal charge-transfer (CT)[41-45]. The appearance of CT resonances in metal-adsorbed or chemisorbed molecules alters the local enhancement by modifying the Raman polarizability relative to isolated molecule[42]. Note, in addition to the electromagnetic enhancement, the motion of 1 electron by 1 ångstrom via CT implies internal fields much stronger than may be obtained through any applied field. As such, the interplay between plasmon and electron mediated (photo)physics is a relevant consideration for developing a mechanistic understanding of SE processes at nanojunctions. Furthermore, there is increasing evidence that the observables in SE spectroscopies are dictated largely by atomic, rather than nanometeric, detail.

Arguably, SE scanning probe microscopies such as TERS are ideally suited to address concerted, plasmon driven chemical and electromagnetic processes while simultaneously providing an efficient route to developing the spatially resolved analog of SM SERS. In this

regard, several milestones have been met in near-field plasmon-enhanced optical microscopy and spectroscopy, including *1)* Raman chemical imaging with sub-nanometer precision in ultrahigh vacuum (UHV) and at ultralow temperatures[46], *2)* hyperspectral TERS with angstrom resolution at room temperature[40], and most recently, *3)* Raman imaging of single atoms and intramolecular charge distributions via apex-bound reporters[47]. These examples share common ground in representing successful combinations of optical spectroscopies with cavity plasmonics, permitting multimodal imaging with unprecedented resolution in both space and time. For scanning probe applications in the ambient, sharp gold or silver tips with cone radii < 50 nm have emerged as standard. Under UHV conditions, tip sharpness may be improved beyond 50 nm using ion sputtering techniques and high-voltage field emission[40, 47], enabling atomic termination and submolecular resolution[40, 46-47]. In addition, these accounts highlight that nanometric surface smoothness is essential for the execution of TERS. This ensures that the signal is entirely localized on the tip apex and eliminates hot spots that act as loss channels or parasitic SERS sources.

Extending the foregoing achievements of plasmon-enhanced near-field spectroscopy to include general coherence manipulation schemes with ultrafast pulses affords chemical imaging with joint ångstrom-femtosecond space-time resolution. Reaching this limit requires the development of the non-linear analog of SE molecular spectroscopy. When exercised with multiple ultrashort (< 100 fs) laser pulses, coherent spectroscopies are capable of monitoring electronic and vibrational wavepackets in real time, which has been amply demonstrated on molecular ensembles[48-49]. A number of techniques involving short pulses are commonly employed in the context of SERS, including femtosecond stimulated Raman scattering (FSRS)[50-53] and coherent Raman scattering (CARS)[54-64]. The majority of

these accounts, however, are implemented in the frequency domain and on ensembles of plasmonic junctions. Retrieving the temporal dynamics of SM's, which was recently demonstrated[64], poses a greater challenge, largely due to the peak laser intensities associated with short pulses. This work, which utilized time-resolved SECARS, captured the vibrational motion of a SM. It was shown that SM's are free from pure dephasing, which fundamentally limits the observation period for coherent dynamics in ensembles. This fundamental finding implies important distinctions between the ultrafast processes that govern molecular dynamics in SM and ensembles, which merits further investigation.

In what follows, the chronicled experimental and theoretical efforts to more thoroughly understand plasmon-mediated phenomena at the nanometeric and atomic scales are presented. A variety of methods and apparatus are employed to achieve this, ranging from SM SERS exercised in the ambient to UHV SM TERS performed under cryogenic conditions. In Chapter 1, experiments revealing the optical properties of isolated nantennas are presented in conjunction with multicolor SERS measurements on the same, aimed at probing the frequency dependent coupling between plasmons and molecules. The latter portion of this chapter is devoted to understanding the fundamental limitations involved in ultrafast SE experiments, which are probed through joint femtosecond-continuous wave SERS. In Chapter 2, vibrational population dynamics are explored through ultrafast SERS executed with 7 ps pulses. In Chapter 0, the principles of ultrafast coherent SE molecular spectroscopy are exercised through SECARS experiments executed on individual dimer nantennas in the ambient. In Chapter 4, ultimate control and sensitivity in TERS is demonstrated through atomically resolved chemical imaging of an insulating monolayer crystal surface. Finally, in Chapter 5, a novel photonic crystal fiber-based apparatus for

executing time-domain SECARS and more general SE non-linear spectroscopies is proposed and developed.

Reaching the ultimate limit of joint ångstrom-femtosecond space-time resolution in molecular spectroscopy represents the principle motivation behind these studies, *vide infra*.

1 Towards time resolved surface-enhanced spectroscopy in the single molecule limit

1.1 Introduction

Surface enhanced Raman scattering (SERS), which takes advantage of plasmonic nano-antennas (nantenna) to enhance and confine fields, is an established method for performing vibrational spectroscopy in the single molecule limit[1, 15, 65-68]. Conceptually, the technique is straightforward: properly designed nantennas allow convenient detection of the near-field molecular response with a far-field photo-detector[65, 69]. Typical implementations involve exploring the coupled molecule/nantenna parameter space through continuous wave laser excitation and are therefore fundamentally limited to the information content available in frequency space. In contrast, non-linear spectroscopies, when executed in the time domain with short pulses, have the ability to probe the dynamical part of plasmon-molecule interactions, opening up the field of quantum molecular photonics by the quantized nature of the interrogated matter. Nonlinear optical manipulations in this limit obey quantum logic, and should lead to the realization of applications that have already been considered in ensembles, which however suffer from the classicality that dominates coherent states of ensembles[70].

As a second order process, time-resolved Raman scattering is useful to consider as a step toward the more general nonlinear optical schemes of coherence manipulation in the single molecule limit. While it is well established that SERS has the sensitivity to reach the single molecule limit, its time domain implementation is subject to fundamental limits, principally because of the large local fields involved in generating the SERS signal.

It was recently shown that under optimized conditions, molecular vibrational information is preserved when the conventional continuous wave (cw) illumination in SERS is replaced with short picosecond (ps) pulses[71]. In nonlinear coherent Raman, however, the combined molecule-nantenna system interacts with the multiple fields required to drive a given nonlinear process, and the resulting signal is often dominated by the nonlinear electronic response of the plasmonic nantenna itself. Although the electronic response of plasmonic nanostructures has been studied in the context of nonlinear optical interactions, including second harmonic generation (SHG)[72], sum-frequency generation (SFG) and four-wave mixing[73-76], ultrafast studies that probe the molecular response mediated through the nantenna are few[77].

To directly clock vibrational motions of individual molecules in real time, it is necessary to rely on time-resolved nonlinear spectroscopy that uses at least two short laser pulses (pump and probe). The implementation requires the development of the surface-enhanced (SE) analog of ultrafast nonlinear spectroscopies. To this end, the response of plasmonic nantennas to ultrafast laser pulses and the coupling between the nantenna and its molecular load are critical considerations, which are most appropriately addressed on isolated plasmonic junctions.

The gold dimer nantenna represents a robust prototype in this regard and is utilized in the present in conjunction with a non-resonant Raman reporter molecule to establish the principles of SE spectroscopy in the joint single molecule - ultrafast limit. As presented below, the dynamic range between detection and destruction of single molecules via SE-NLO is rather narrow. The accumulated statistics of measurements carried out on several

hundred individual dumbbells provides an exploration of the mechanisms of degradation, which can be distilled into fundamental limitations in SE-NLO measurements.

1.2 Methods

1.2.1 Sample preparation

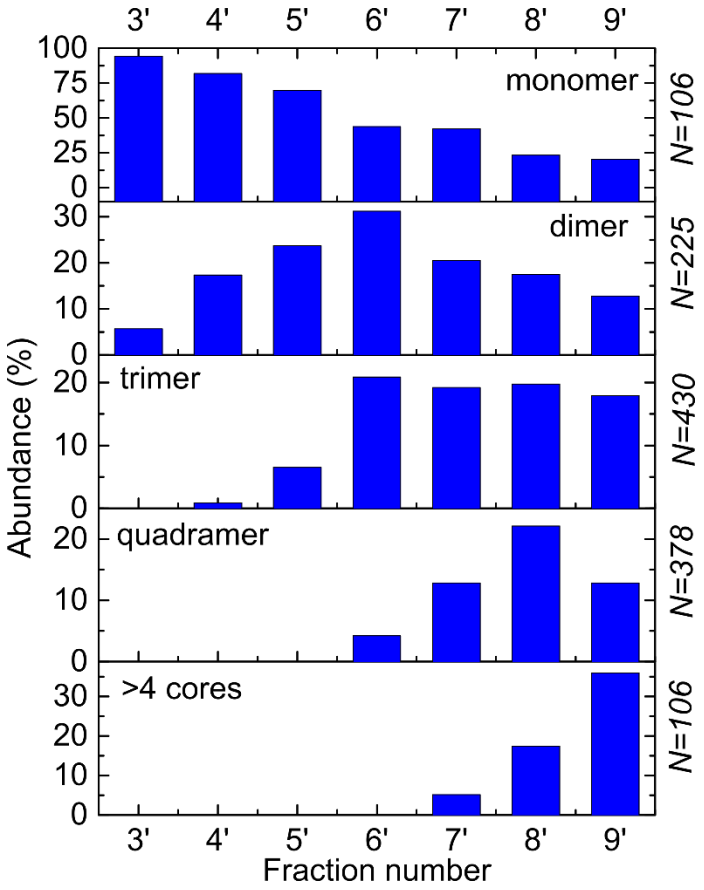

Figure 1.1 Nantenna ultra-centrifugation results. The abundance of N-core species ranging from monomer to > 4 cores are shown as a function of fraction number. These data were obtained through SEM characterization of the purified aliquots. The number of samples used in the calculation of the abundance is shown to the right of each distribution. Effective isolation of the dimer nantennas is evident for fraction 6' (30%) which represents a five-fold increase compared to the unpurified concentration.

The gold dimer nantenna plasmonic substrates utilized here were acquired commercially (Cabot Inc.) and consist of a pair of 95 nm gold spheres that are separated by sub-nanometer gap. The structures are encapsulated in a 40 – 70 nm thick silica shell post aggregation and drop cast onto a TEM grid, consisting of 8 nm thick silicon nitride windows. This permits facile post-optical high-resolution electron imaging and also limits optical backgrounds

generated by the substrate. Prior to encapsulation, 1,2-di(4-pyridyl)ethylene (BPE) molecules are promoted over the spheres in monolayer coverage and serve as a Raman reporters. The nantenna samples are polydisperse and consist of aggregates containing N cores (N ranges from 2 to ~10).

To isolate the dimer nantennas an ultracentrifugation procedure was employed[78]. Briefly, a linear gradient of iodixanol centrifugation medium was created in a 15 mL tube. The linear gradient ranged from 30% w/v at the top of the tube to 60% w/v at the end. This was accomplished using the SC-15 Linear gradient maker (Hoefer Inc.) and 2.5 mL starting volumes of each solution. The lower density solution was placed in the reservoir tube and the higher density solution was placed in the mixing chamber, along with a 10 mm magnetic stir bar. A 200 μL volume of 2 % w/v the nantenna stock solution of nantennas was layered over the density medium and the mixture was centrifuged at 500 g for 10 min. After centrifugation, 50 μL fractions were collected from the center of the tube, beginning at the top and ending at the bottom. In total, 26 fractions were collected.

To evaluate the efficacy of the purification process, fractions 3 through 12 were rinsed to remove any remaining iodixanol and characterized with SEM. The rinsing procedure is as follows: 10 μL aliquots of fractions 3 to 12 were isolated and diluted to 1 mL with water. Each fraction was vortexed and then centrifuged at 6 k RPM for 15 minutes. Following centrifugation, the aqueous supernatant was removed, and each sample was re-diluted with 1mL of water, vortexed and subsequently sonicated for 3 minutes. For the characterization, approximately 1 μL of each rinsed fraction was drop casted onto a silicon wafer and was allowed to dry prior to performing SEM. The relative abundance of each nantenna type

(monomer, dimer, trimer etc.) was identified and tabulated for each fraction. The results are summarized in Figure 1.1.

1.2.2 Single nantenna extinction

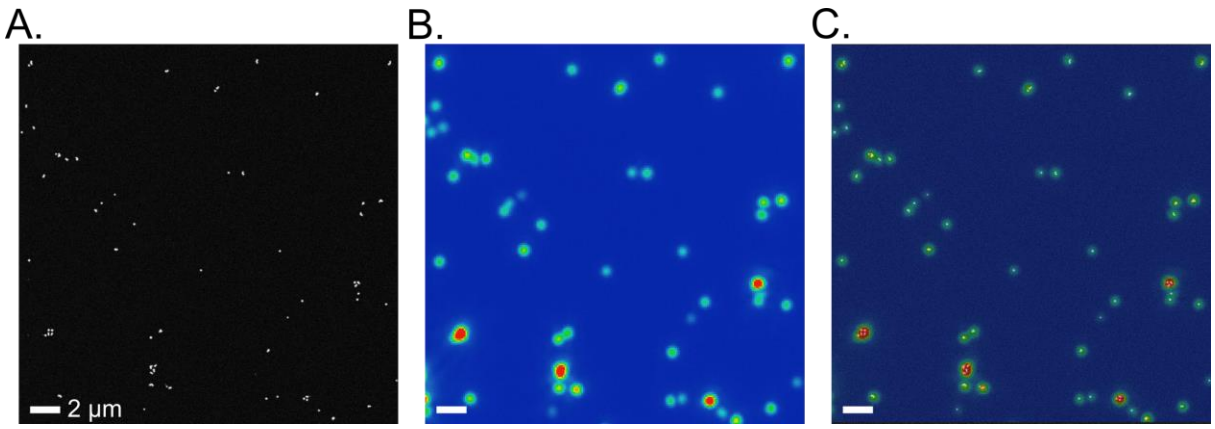

Figure 1.2 Correlated (A) SEM and (B) diffraction limited dark field images of the nantennas. (C) Overlay of (A) and (B).

Single particle, polarization resolved extinction measurements (see section 1.3) were carried out on using a conventional inverted optical microscope adapted for dark-field scattering in transmission mode. A tungsten-halogen source was used in conjunction with a dark-field condenser lens to illuminate the TEM grid supported nantenna samples. The condenser lens contains a Fourier mask which allows only the outmost portion of the full 0.9 numerical aperture excitation cone angle to reach the sample. A 0.65 NA collection objective was used to collect the scattered radiation, which was sent into a monochromator equipped with a cooled CCD camera (Andor iDus 401, Shamrock SR303i). This system with equipped with a 150 lines mm^{-1} grating blazed at 800 nm, permitting spectral acquisition over a large range (400 to 1000 nm). Individual particles were identified using the spectrograph operating in imaging mode (0^{th} order). This is shown in Figure 1.2 which compares an electron micrograph acquired through SEM to a diffraction limited dark field image over the same region. The spectrograph slit was used to isolate individual dimers for spectral

acquisition. Extinction spectra were recorded by subtracting the substrate response from the nantenna signal. The former was obtained from equal area regions directly adjacent to the particles of interest. In both cases, the integration times ranged from 1 to 10 seconds, depending on the apparent contrast. A linear polarizer placed in the detection path allowed the long and short axis responses of the dimer to be differentiated. All spectra were normalized to the spectrum of the source.

1.2.3 Continuous-wave SERS

Continuous-wave SERS spectra (see Section 1.4) were obtained using an inverted optical microscope equipped with a piezo scanning stage. The excitation sources (633 nm HeNe or 532 nm diode laser) were focused at the object plane via a high numerical aperture objective lens (40x oil, 1.32 NA). Images of the nantennas were acquired by scanning the sample stage in the *xy* plane over an area of 100 x 100 um while recording the transmitted light with a photomultiplier tube. Individual particles were identified by comparing the transmission images to SEM images acquired either before or after optical studies. Spectra were acquired in the back-scattered direction by separating source and Raman photons with dichroic beam-splitters that were matched to the excitation wavelength. Paired notch filters were also included in the collection path for further filtering of the source. A cooled camera spectrograph (Andor iDus 401, Shamrock SR303i) equipped with a 1200 lines mm^{-1} grating was utilized for acquiring spectra. Typical integration times were 1 s.

1.2.4 Damage threshold measurements

Damage threshold measurements were carried out on individual nantennas using the optical microscope described in Section 1.2.3 and two different three-color, 100 fs sources, designed to carry out background-free measurements in the time domain. The first consisted of two home-built non-collinear optical parametric amplifiers (NOPA), pumped with a 250 kHz regeneratively amplified Ti:sapphire laser (Mira Seed/REGA 9000, Coherent). The second consisted of an 79 MHz Ti:Sapphire pumped photonic crystal fiber (PCF), tailor-made for SE-NLO[79]. This will be discussed in detail in Ch. 5. Tolerable local intensities were determined by recording cw SERS spectra as time series during ultrafast irradiation. Relevant measurement parameters (incident intensities, exposure times etc.) will be noted where appropriate.

1.3 Characteristics of dimer nantennas

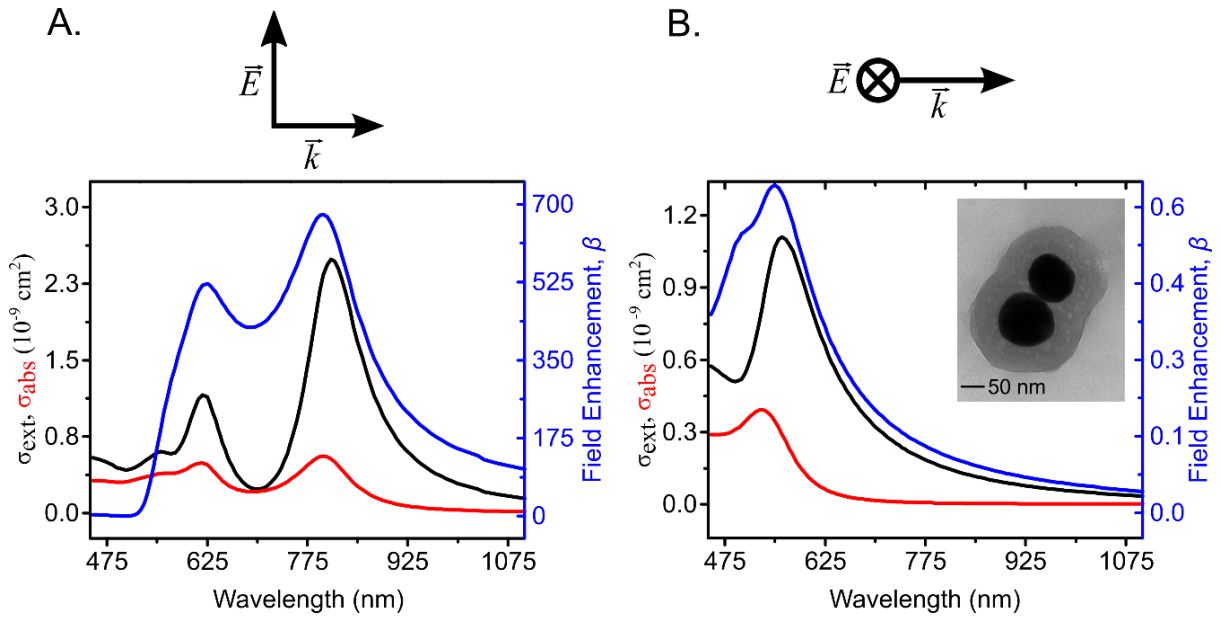

Figure 1.3 Simulated linear spectral response for a nantenna consisting of a pair of 45 nm radius Au spheres separated by 1 nm. Longitudinal (A) and transverse (B) excitation are shown for the extinction (black trace), absorption (red trace) and field enhancement factor (blue trace). Inset: transmission electron micrograph of a prototypical antenna.

A transmission electron micrograph of the typical dumbbell nantenna used in the present studies is shown in the inset of Figure 1.3. It consists of two gold nanospheres, of ~95 nm diameter (D), separated by a junction gap (*g0*) of 1 nm, and encapsulated in a silica shell of 40 - 70 nm thickness. Note, the parameter *g0* is taken as the edge-to-edge distance between the spheres. The simulated linear spectral response of the idealized version of the same structure is presented in Figure 1.3 for two different incident electric field polarizations. The extinction spectrum, the absorption spectrum, and the spectral dependence of the field enhancement in the middle of the intersphere junction, given by the ratio $\beta = E_L/E_0$ of local and applied field are presented. The nantenna sustains three major resonances that may be loosely assigned according to the commonly used hybridization model[17] to: the bonding dipolar plasmon at 816 nm, and the bonding and anti-bonding

quadrupolar plasmons at 618 nm and 555 nm, respectively. Several observations are noteworthy at the outset. There is a dramatic difference in enhancement factors between longitudinal and transverse excitation. Only quadrupolar resonances are accessed in transverse excitation, in which case $\beta < 1$ at the intersphere junction. Also, scattering spectra are loosely correlated with the spectral dependence of β. This is clearest at 700 nm, which corresponds to the valley between scattering resonances (Figure 1.3 A), yet $\beta \sim 400$, not very different from the peak value $\beta \sim 700$ reached at 816 nm. Both values correspond to very large SERS enhancement factors of $\beta^4 \sim 10^{10}$-10^{11}. The apparent discrepancy is due to the fact that the extinction spectrum reflects the induced polarization integrated over the entire surface of the dumbbell, while the enhancement reflects the charge density concentrated at the junction (at the hot spot). A figure of merit of the efficiency of the nantenna can be obtained from its radiation rate, given in which for a given plasmon mode can be extracted from the integrated absorption cross section over its resonance:

$$1/\tau_r = \frac{8\pi}{\lambda^2}\int \sigma_a(\nu)d\nu. \qquad (1.3.1)$$

Over the extracted timescale, $\tau_r = 10$ fs, radiation competes with Landau damping, which dominates at this size scale. Note that although the binding quadrupole is nominally dark, it radiates (absorbs) through its coupling to the binding dipolar plasmon. The finite element simulations reported in Figure 1.3 were carried out using the COMSOL multiphysics suite of programs, with the recently revised dielectric function of gold[80], and the literature value of silica[81] as inputs.

The simulations provide a benchmark for the obtainable field enhancement factors and optical scattering cross sections for the idealized structure. Deviations from sphericity and variations in the junction length alter the nantenna optical properties and the

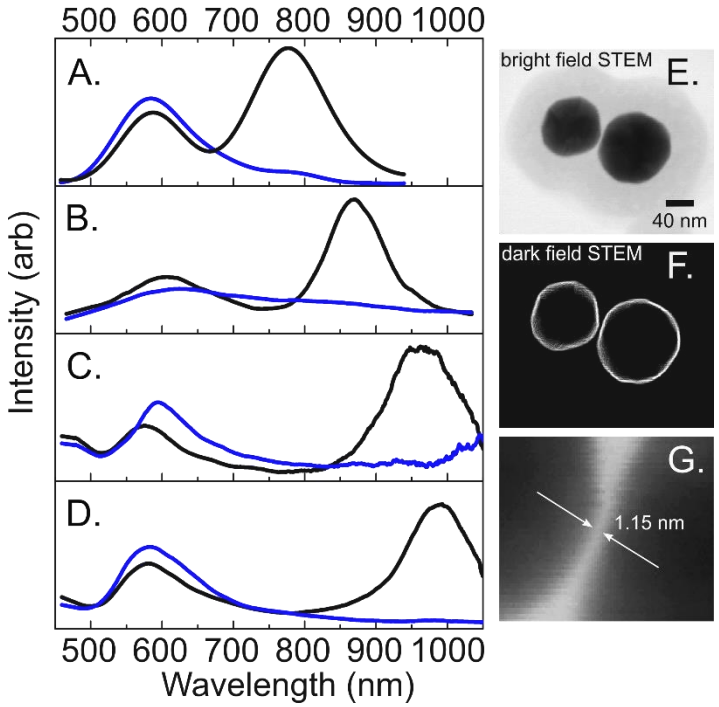

Figure 1.4 Linear extinction spectra recorded on individual dimer nantennas (A-D) through dark field spectro-microscopy (see Methods). Spectra under longitudinal and transverse excitation are shown in black and blue, respectively. High resolution electron micrographs of the dimer corresponding to the spectrum shown in A are shown in E-F. Bright and dark field STEM collection geometries provide the nantenna gross morphology and junction fine structure, which is shown in G. The latter reveals a physical gap of 1.15 nm.

spectroscopic observables relevant to SERS. This is highlighted in Figure 1.4 which compares experimentally obtained extinction spectra for four different dimer nantennas collected via dark field scattering spectro-microscopy. The spectral features observed are generally consistent with the simulated extinction shown in Figure 1.3 and may be recognized accordingly as the binding dipolar plasmon resonance in the range from 700 to 1000 nm and the quadrupolar resonance(s) in the range from 550 to 650 nm. Significant variation in the center wavelength of the dipolar resonance is observed from particle to particle. The predicted higher order quadrupolar resonances appear as a single broad feature near the red tail of the d-band to Fermi surface transition frequency for bulk gold (520 nm) and are

relatively stationary[80]. Overall, the observed polarization contrast emphasizes the character of the dipolar plasmon as an inherently junction-localized mode.

The agreement between the simulated and measured extinction is exemplified by the spectrum shown in Figure 1.4 A. Here, the dipolar and quadrupolar resonances are centered at 775 and 575 nm, respectively, which are within one standard deviation of the predicted extinction values of 580 and 810 nm. Variations between the structural parameters used in the FEM simulations, which are based on the idealized pair of equal radii nanospheres, and the experimental nantenna geometry lead to the apparent discrepancies in the peak positions. Establishing the latter requires high resolution electron microscopies that are capable of capturing the nantenna morphology while preserving the fine structure of the junction. As a result of the electron energies and current densities required for high contrast, conventional transmission electron microscopy (CTEM) imaging eventually leads to fusion of the junction and evolution of the spheres themselves. For these reasons, cryogenic scanning transmission electron microscopy (cryo-STEM) is preferred over CTEM. STEM micrographs acquired at 80 K of the nantenna corresponding to the spectrum shown in Figure 1.4 A are shown in Figure 1.4 E-G. The individual spheres appear faceted and are size distributed (left: 81 nm, right 100 nm). High resolution imaging of the junction itself reveals an isolated physical gap of 1.15 nm (Figure 1.4 G). This example highlights both the efficacy of classical computation methods for describing the optical response of the dimer structure and the inherent morphological heterogeneity that characterizes surface enhanced spectroscopy at the single nantenna level.

In addition to the intraparticle size and shape variations revealed by electron microscopy, the spectra in Figure 1.4 B-D suggest significant interparticle structural

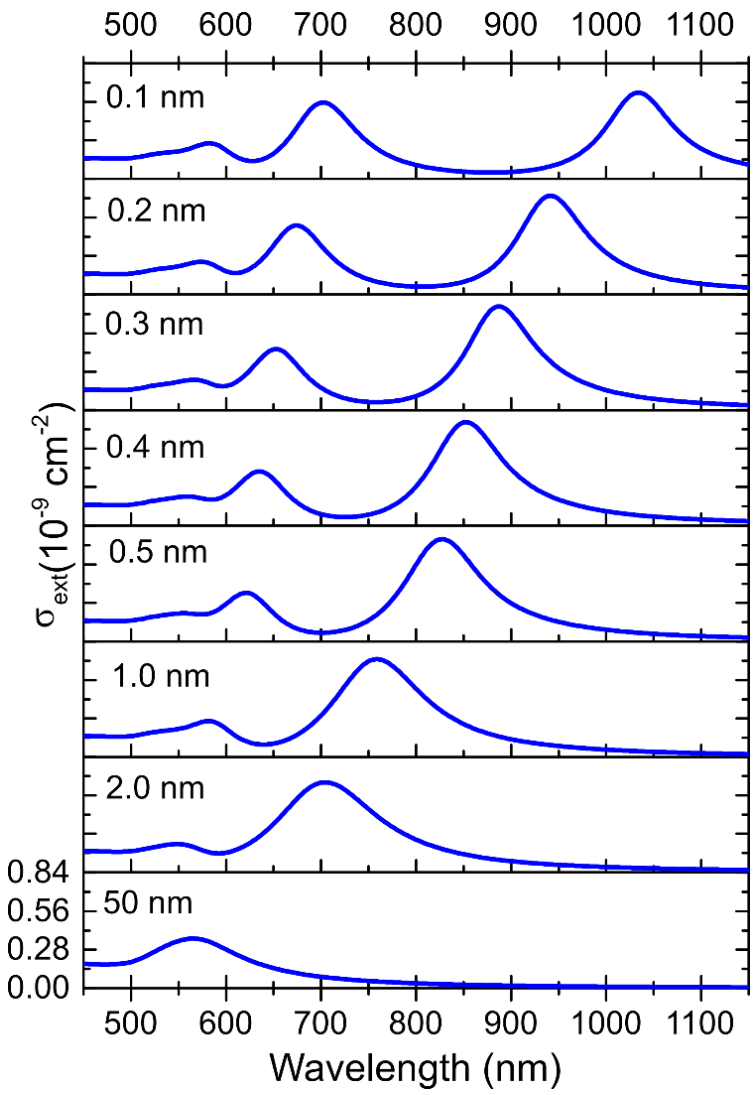

Figure 1.5 Calculated gap dependent extinction spectra for an Au dimer of 95 nm diameter embedded in a homogeneous medium with a dielectric constant of 1.25.

heterogeneity. The preservation of the general spectral features and the consistency among the linewidths across this series suggest similar single sphere polydispersity, which was shown above to only weakly modify the position of the resonances. Instead, the large tuning of the position of the dipolar resonance for this set, which ranges from 775 to 1000 nm, is indicative of variation in the vacuum gap length, *g0*. Quite generally, the local field generated at the intersphere junction is a strongly varying function of *g0*. In the present, the gap dependent extinction spectra for the dimer nantenna are theoretically considered using

generalized multiparticle Mie theory (GMM). GMM has been utilized extensively for calculating the optical properties similarly sized plasmonic nanostructures and permits the use of *g0* as a tunable parameter in the calculation of the multipolar expansion coefficients[82-88]. The gap dependent absorption and scattering spectra calculated for 95 nm diameter Au spheres are shown in Figure 1.5. Here, *g0* was varied from 50 to 0.1 nm and Mie coefficients up to 40th order were included to satisfactorily describe the response. There are several notable features. First, for large separations, *g0* ~ D, the extinction approaches the single sphere result, which exhibits a broad dipolar mode centered near 560 nm. With decreasing separation, the dipolar mode strongly red shifts. Moreover, the appearance of higher order modes is evident for *g0* = 2 nm, consequently in the regime where *g0*<<D. In the absence of independent measurements of *g0* for the dimers presented in Figure 1.4 B-D, which were obtained for the particle presented in Figure 1.4 A, these results allow the gap separation to be assigned with confidence based on the wavelength of the dipolar mode. As such, the spectra in B, C and E are consistent with *g0* = 0.4, 0.2 and 0.16 nm respectively, in effect, subatomic.

From a conceptual standpoint, the red shifting observed for the dipole and higher order modes may be understood in terms of the behavior of coupled dipoles. In the so-called quasistatic limit, the sum total of electron oscillators that comprise the free electron density of the single sphere are replaced by an individual dipole centered at the sphere origin[32]. In the limit of a coupled sphere pair, attractive interactions between charges at the intersphere junction have the tendency to weaken the induced polarization, resulting in a decrease in the energy of the bound sphere state[89-90]. As such, red shifting of the dipolar mode is expected with decreasing separation for an induced polarization along the dimer axis (in-phase

oscillation). For narrow separations, such as those explored in the GMM simulation, the presence of higher order multipoles precludes the use of the quasistatic approximation for effectively treating the magnitude of the peak shifts, although the general trend is correct. In the narrow gap limit, where $g0$ <<D, electric fields are distributed inhomogeneously across the dimer, reaching their maxima at the center of the junction. This extreme junction localization, which is the essential driving force in surface enhances spectroscopies, requires several multipole orders to adequately describe with theoretical models[91]. As a direct manifestation, the peak wavelengths calculated via GMM red shift more quickly with decreasing gap than predicted through pure dipole-dipole interactions, which go as $(g0/\mathrm{D})^{-3}$. This indicates that quasistatics underestimates the magnitude of intersphere coupling[92].

Overall, the Au dimer nantenna represents a robust substrate for performing optical spectroscopy in the single molecule limit. The properties and characteristics revealed by the linear scattering measurements and classical simulations described above will be used herein to quantify and rationalize observations relevant to the integrity of the nantenna itself and driven junction molecules. In what follows, single nantenna SERS experiments of nonresonant molecular reporters will be described.

1.4 SERS of plasmonic nantennas and their molecular load

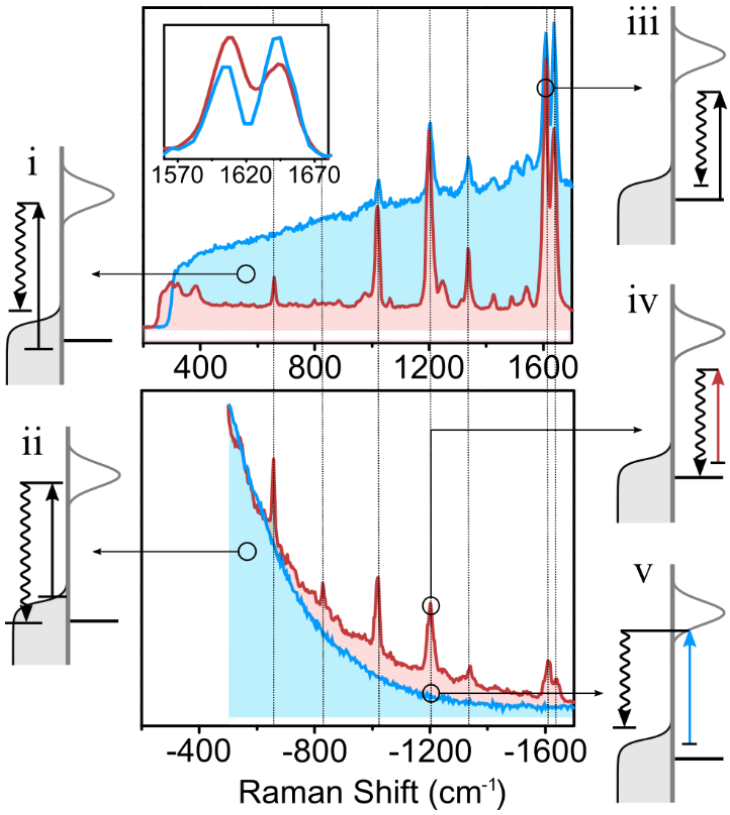

Figure 1.6 Stokes (top) and anti-Stokes (bottom) cw-SERS spectra recorded on a single nantenna at 532 nm (light blue trace) and 633 nm (red trace) excitation. Note the absence of vibrational lines in the anti-Stokes spectrum at 532 nm. Inset: Magnified C=C stretching modes at 1604 cm^{-1} and 1640 cm^{-1} revealing Gaussian profiles of FWHM ~20 cm^{-1}. The various scattering contributions are indicated schematically: (i) Stokes of metal ERS, (ii) anti-Stokes ERS, (iii) Stokes of molecular SERS, (iv) anti-Stokes of molecular SERS, perfectly aligned with vibrational Stokes lines, (v) absence of the molecular anti-Stokes lines at 532 nm, which is ascribed to the competition with molecule-metal scattering through the interfacial state resonance.

Ideally, the nantenna serves as a silent mediator between the far-field and near-field radiation. However, in optical measurements, electronic Raman scattering (ERS) of the metal and the coupled response of the molecule-metal system are integral parts of the observables. A synopsis of the information contained in cw-SERS spectra with regard to the interplay between molecular SERS and ERS of the nantenna is illustrated in Figure 1.6. The vibrational

SERS of the reporter molecule, bipyridyl ethylene (BPE), can be seen to ride over a background continuum that can be rigorously assigned to ERS. The vibrational assignments have been reported previously[93], and an analysis of the continuum was given recently[94]. Here, note that the relative intensity of SERS and ERS depends on excitation wavelength and polarization angle. In longitudinal excitation, the ratio changes by a factor of ~20 between 532 nm and 633 nm, and the background becomes negligible at 785 nm (not shown). Transverse excitation at 532 nm, shows ERS only, consistent with the fact that the accessed purely quadrupolar plasmon does not generate any significant fields at the intersphere junction (Figure 1.3 B). This highlights that ERS arises from the net polarization induced on the nantenna, while SERS arises from the hot spot where the field is confined on a scale comparable to the molecular dimensions. In transverse excitation, the relative contributions of ERS and SERS scale by the spectral dependence of scattering and β discussed above. The clearest signature of ERS is the anti-Stokes branch of the continuum, which decays exponentially as a function of Raman shift[94-96]. It perfectly fits the Fermi-Dirac distribution of hole states, which serve as the thermally occupied terminal states in ERS (see Figure 1.6 ii). The fit of the anti-Stokes ERS to the Fermi Dirac distribution yields the temperature of the nantenna and its dependence on excitation intensity yields the heating rate, which limits the tolerable average irradiation intensity. Remarkably, the vibrational anti-Stokes lines of the molecule, which can be seen at 633 nm, are completely absent when excited at 532 nm. This is ascribed to the competition between molecular SERS and molecule-to-metal scattering[94] with a real interfacial state resonance reached at 532 nm (Figure 1.6 v). The continuum of final states in this scattering process explains the absence of sharp vibrational anti-Stokes lines.

Although the location and number of molecules participating in scattering is not known, the absence of detectable SERS on single spheres establishes that the observed molecule(s) are near the hot spot of the junction in the dimer structures. Given that Raman is a feeble effect, the local field enhancement, $\beta = E_L/E_0$, provided by plasmonic nantennas is essential to boost its strength. Making the standard approximation of quartic field enhancement, the count rate, R, of spontaneously scattered photons in cw-SERS can be estimated as:

$$R_{cw-SERS} = \frac{\eta}{\hbar\omega_i}(\beta_i^2 I_i)(\beta_s^2 \sigma_s) = \frac{\eta}{\hbar\omega_i} I_L \sigma_s^* \qquad (1.4.1)$$

in which η is the collection efficiency (~0.1 under optimized geometries); I_i (W/cm^2) is the incident field intensity, σ_s(cm^2) is the spontaneous scattering cross section, and the subscripted β recognizes its wavelength dependence. The enhancement factors have been grouped to emphasize that the effect in $I_L = \beta^2 I_i$ is to reduce the demand on incident intensity. Based on the known non-resonant Raman cross section of $\sigma_s = 5 \times 10^{-28}$ cm^2 for the strongest C=C stretching lines near 1600 cm^{-1} for BPE [13], the observed count rates of 10^2-10^3 s^{-1} at an excitation intensity of 30 μW/μm^2 suggests an enhancement factor $\beta^4 = 10^8$ at 532 nm. Within the errors of this determination, the extracted local field enhancement of β =100 agrees with the calculated value of 50 at 532 nm (Figure 1.3).

1.5 Pulsed vs. cw count rates

The dynamic range between structural evolution and detectability in pulsed SERS measurements in limited. This arises from the same enhancement factors that determine sensitivity; For pulsed-SERS, the count rate is determined by the peak intensity I_L^{peak} and fill factor $ff = f\delta t$, given by the product of laser repetition frequency, f, and pulse width, δt:

$$R_{pulsed-SERS} = \frac{\eta}{\hbar\omega} I_L^{peak} \sigma_S^* ff \qquad (1.5.1)$$

At a repetition rate of 76 MHz and pulse width of 7 ps, ff = 5×10^{-4}. This corresponds to I_0^{peak} 10^7 to 10^8 W/cm^2 for average intensities in the micro to milliwatt range under tight focusing conditions (~1 μm^2). To compensate for the fill factor the peak intensity in the pulsed measurements must be increased by four orders of magnitude. Given typical intensities used in cw-SERS of 10^4 W/cm^2 (at 633 nm), the required incident peak intensity is $I_L^{peak} \sim 10^8$ W/cm^2. The computed value of $\beta \sim 3 \times 10^2$ at 785 nm implies local intensities approaching $I_L^{peak} \sim 10^{13}$ W/cm^2, which is on the order of the ionization threshold for molecular matter[97]. In what follows, this intensity regime is explored further through multicolor SERS experiments involving ultrafast pulses. Mechanisms of signal degradation and are understood in terms of (photo)chemical and (photo)physical transformations that may dominate spectroscopic observables in the strong field limit.

1.6 Mechanisms of signal degradation

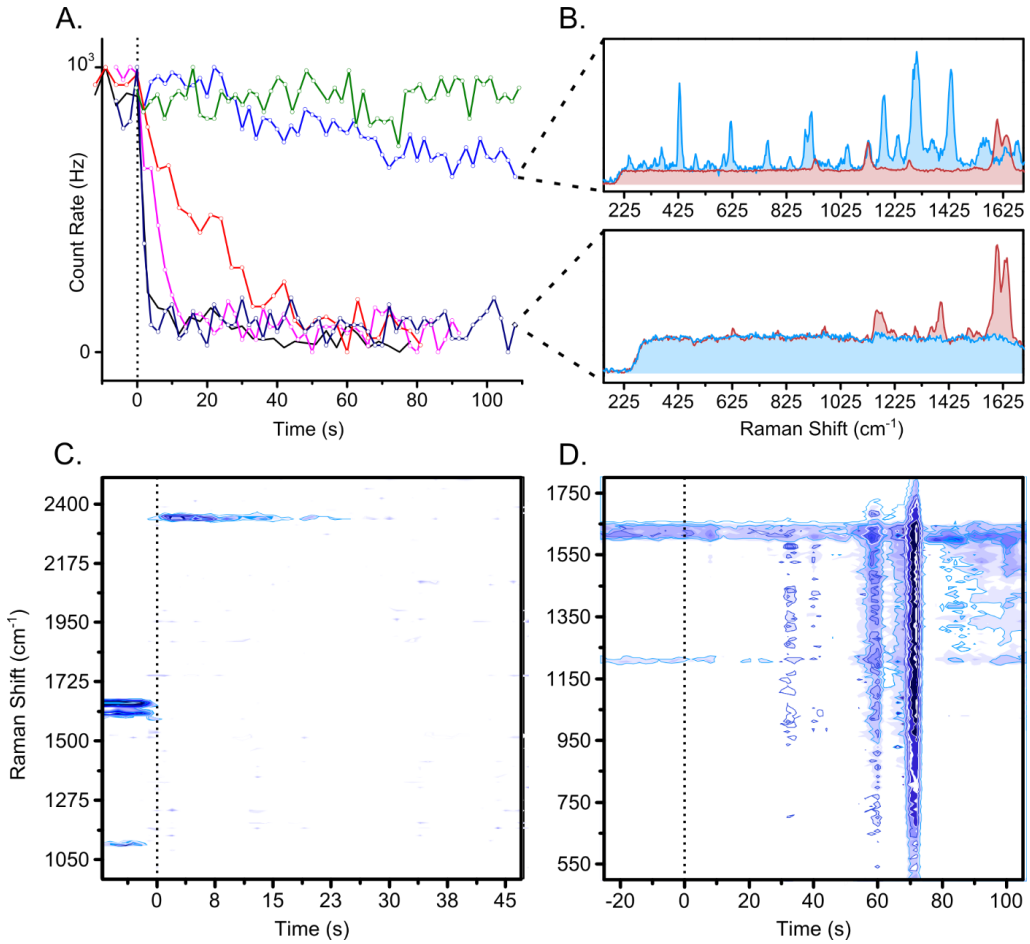

Figure 1.7 (A) Set of decay profiles taken on different nantennas depicting the evolution of the 1640 cm^{-1} line, during fs irradiation: 610 nm, 100 fs pulses, 1–5 $\mu W/\mu m^2$ at 79 MHz (purple, black and blue traces); and 50–100 $nW/\mu m^2$ at 250 kHz (red, olive and cyan traces). (B) Pre- (post-) fs irradiation SERS spectra shown in red and blue, respectively. Top in B illustrates the generation of an unfamiliar spectrum; bottom panel in B illustrates loss of the molecular signal and preservation of the ERS background. (C/D), SERS trajectories, consisting of sequentially recorded spectra at a rate of 1 frame/s, acquired during fs laser irradiation, highlighting distinctive behaviors: (C) the disappearance of the molecular signature concomitant with the appearance of a new line assigned to CN. (D) Arcing through a junction as discerned by jumps in the ERS continuum.

As mentioned above, the same enhancement that affords single molecule sensitivity is responsible for the narrow intensity window between signal quantification and signal degradation. In the present, the integrity of the nantenna is interrogated through the anti-Stokes ERS and that of its molecular load through SERS recorded during fs laser irradiation.

Large variations in behavior are observed on different structures under similar excitation conditions. Examples that illustrate prototypical mechanisms of signal decay are presented in Figure 1.7 A-D. In these measurements, multicolor 100 fs pulsed were applied at t=0 while monitoring the molecular SERS in the Stokes region. The variation in the rate of decay of the molecular SERS is illustrated in Figure 1.7 A by the intensity of the 1640 cm^{-1} line. With time resolution limited by the SERS acquisition time to 1 s, the observed decay profiles range from sudden to gradual, from seconds to many minutes. The latter represent the survivors that live long enough to be measured. Before and after SERS spectra are shown in Figure 1.7 B, to highlight that in addition to decay of the parent spectrum. Instances of plasmon-driven chemistry are evidenced by the appearance of an unfamiliar new molecular spectrum (Figure 1.7 B top panel). In the SERS trajectory of Figure 1.7 C, within one frame at t = 0, the BPE spectrum disappears, giving rise to the spectrum of the CN dissociation product, in what appears to be plasmon driven rupture of the parent pyridine rings. The excitation is at 800 nm, at a local intensity nearing $I_{L,max} \sim 10^{13}$ W/cm^2, in the strong field limit of 8 V/nm. In the SERS trajectory of Figure 1.7 D, recorded under similar conditions, arcing across the junction by the charge transfer plasmon can be identified by the jumps in the ERS continuum. Such arcing events are also seen under cw excitation, at local fields of ~0.1 V/nm[98]. Arcing is typically followed by fluctuations in the molecular SERS spectra, as is evident in the trajectory at t = 80 - 100 s (Figure 1.7 D). Among the variety of processes that occur in the strong field limit, several may be identified as operative in these experiments: internal field emission (arcing), plasmon driven ionization, photo-dissociation, and separation of the molecule(s) from the hot spot while maintaining its identity.

1.7 Local intensity limit

The extensive exploration of intensities at which the signal decays is summarized in Figure 1.8, as a function of the fill factor. Within the order of magnitude uncertainty associated with defining damage thresholds, a well-defined limit in incident field intensities of 10^8 W/cm^2 may be discerned. Under the assumption of a common field enhancement factor $\beta = 100$, tolerable local fields of $10^{12} – 10^{13}$ W/cm^2 is established. In effect, detectability in pulsed measurements, as given in (1.5.1), is subject to the fundamental strong field limit[97]:

$$I_{L,max}^{peak} < 10^{12} - 10^{13}\ W/cm^2 \qquad (1.7.1)$$

In effect, field enhancement reduces the demand on the incident intensity. The limit of $ff \rightarrow 1$ is subject to yet another limitation, namely heating and melting of the nantenna, which is the origin of the dramatic contrast between cw ($ff = 1$) and pulsed excitation intensity limits seen in Figure 1.8. Independence of the damage threshold on ff implies that the system cools between pulses.

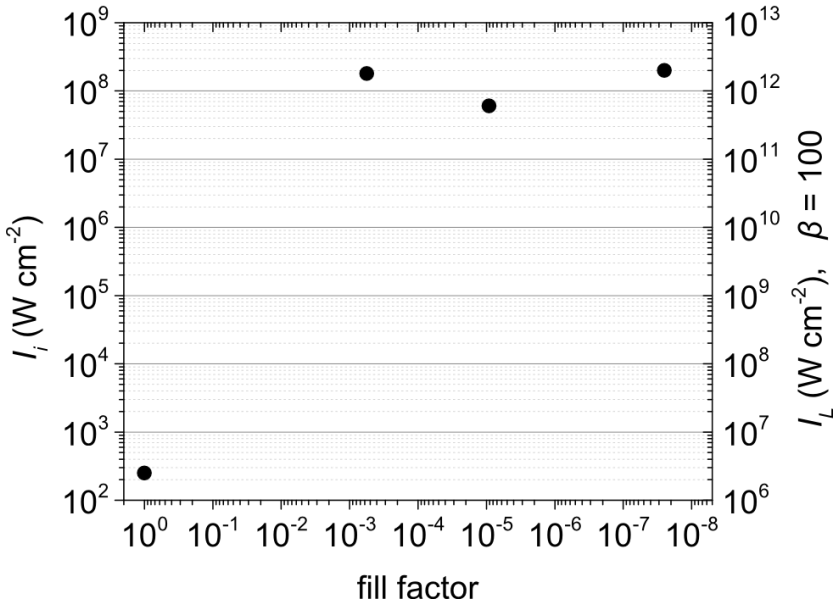

Figure 1.8 Measured tolerable incident and local intensity versus fill factor for an assumed value of $\beta=100$.

1.8 Heating in pulsed and cw irradiation

Heating of the nantenna can be conveniently monitored through the anti-Stokes ERS (Figure 1.6). The fit of the anti-Stokes spectrum to the Fermi-Dirac distribution yields the steady-state temperature of the nantenna. The cooling rate, dQ/dt, is then obtained from the measured steady-state temperature and the calculated absorption cross section (σ_a):

$$\frac{mC_p\Delta T}{\tau} = I_{0,cw}\sigma_a \qquad (1.8.1)$$

The slope of the experimental ΔT vs. I plot[99] implies $\tau\sigma_a/mC_p = 10^6$ K μm^2/W, which yields a cooling time constant of τ = 25 ns ($m = 2 \times 10^{-14}$ g, $\sigma = 10^{-9}$ cm^2 = 0.1 μm^2, C_p = 0.129 Jg^{-1}K^{-1}). The long cooling time reflects the poor thermal conductivity of the silica shell. This can be recognized by estimating the rates of heat transfer from gold to silica and heat transport within the shell. Assuming contact between the metal and its surrounding shell, the heat

exchange time τ_{xc} may be obtained by setting $VC_p=AlC_s$, where A is the surface area and $l = (D\tau)^{1/2}$ is the thermal diffusion length. For a nanosphere, this leads to:

$$\tau_{xc} = \left(\frac{1}{D_s}\right)\left(\frac{r}{3}\frac{\rho_{Au}C_{Au}}{\rho_s C_s}\right)^2 \tag{1.8.2}$$

τ_{xc}= 0.3 ns for a shell consisting of crystalline quartz, τ_{xc}= 1.2 ns for glass, and longer for porous silica. Using conductivity of glass[81], the time for heat to diffuse across the L = 70 nm shell is $\tau = L^2/D$ = 14 ns ($D = 3.4 \times 10^{-7}$ m^2/s), in agreement with the measured cooling time of 25 ns. Heat diffusion through the shell limits the rate of cooling in these dry-mounted, encapsulated nanostructures.

The heat load under cw irradiation, given by (9), is modified in pulsed excitation to:

$$\Delta T(t) = \frac{I_{0,cw}\sigma_a}{mC_p}\frac{1}{f}\sum\nolimits_n \Theta(t - n/f)\, exp\left[-\frac{t - n/f}{\tau}\right] \tag{1.8.3}$$

in which Θ is the Heaviside function, and τ is the cooling time constant. The steady-state temperature can be obtained as:

$$\langle \Delta T \rangle = \frac{1}{t'}\int_{t_i}^{t_i+t'} \Delta T(t)dt \sim \frac{I_{0,cw}\sigma_a}{mC_p}\frac{1}{f}ff = \frac{I_{0,cw}\sigma_a \delta t}{mC_p} \tag{1.8.4}$$

to recognize that the temperature is dictated by the pulse duration δt in this limit.

Note that despite the large temperature rise, the gross shape of the nantenna is verifiably preserved by the silica shell until reaching irradiation intensities of 1 mW/μm^2, where phase explosion is observed[64]. Spectral instabilities set in earlier (at 100 μW/μm^2 at 532 nm). As a general principle, the onset of bulk diffusion (of vacancies) in atomic solids can be taken as $T_{MP}/3$ = 450 K for gold, and significantly lower for surface diffusion. Note that a single gold atom injected in a 1 nm junction gap constitutes a tunneling bridge that may

shunt the displacement current. This would explain the observed arcing and catastrophic collapse of the junction after a period of irradiation (Figure 1.3). Also, large variations in β occur at junction gaps that range between 1 and 0.5 nm, which explain large fluctuations in signal that arise during fusion of the gap. Under ambient conditions, given the bulk diffusion rate, the requirement of ΔT_{max}= 150 K, may be used to define the tolerable average power of irradiation:

$$\langle I_0 \rangle = I_0 ff < mC_p \Delta T_{max} / \sigma_a(\omega) \delta t \qquad (1.8.5)$$

This translates to 100 $\mu W/\mu m^2$ at 532 nm (ff = 1); and knowledge of the wavelength dependent absorption cross section (Figure 1.3) allows generalization of (1.8.5)to different excitation colors.

1.9 Conclusion

The complementary optical and structural characterizations presented here on isolated nantennas underscore the heterogeneity that defines spectroscopic realizations in the limit of one molecule. The vacuum gap length and resulting attainable field enhancement was shown to exhibit variation from particle to particle, manifesting as dramatic shifting of the plasmon resonance(s) toward the near-infrared. The measured extinction spectra in conjunction with FEM and GMM calculations uniquely identify these modes as the binding dipolar plasmon and the bonding and anti-bond quadrupolar plasmons, which come into play when the particle size approaches the wavelength of light. Molecular SERS, mediated through either the quadrupolar or dipolar modes have unique signatures; anti-Stokes molecular information is lost when the excitation frequency is tuned to the quadrupolar

states of the plasmon. In this regime, a scattering channel involving the bulk transitions of the metal, s←d, becomes relevant.

Ultimately, the combination of field enhancement and tight focusing requirements to isolate single scattering centers, lead to limiting strong local fields 10^{12} - 10^{13} W/cm^2 with what may be regarded as weak laser source: 100 fJ per 100 fs pulse (100 μW at 10^8 Hz). For typical nonresonant molecular scatterers, due to the reduced duty cycle of pulsed lasers, the dynamic range between observation and damage threshold is rather limited. In effect, enhancement factors that dictate the sensitivity of SERS can be detrimental in ultrafast measurements. The variety of (photo)chemical and (photo)physical processes that compete at these high field intensities were highlighted through examples. In this regard, the encapsulated nano-sphere dimer is well suited to interrogate plasmonic chemistry in isolation.

2 Plasmon driven vibrational population inversion: a ps SERS study

2.1 Introduction

Plasmonic nanojunctions effectively confine optical fields on length scales that exceed the Abbe diffraction limit by more than three orders of magnitude. This is most directly demonstrated in tip-enhanced Raman scattering (TERS) measurements carried out at the precisely controllable junction of scanning tunneling microscopes (STM), where optical spectro-microscopy of single molecules with submolecular spatial resolution has been achieved[40, 46-47]. Confinement of light is key to single molecule vibrational spectroscopy, as has been amply demonstrated in a variety of structures that sustain junction plasmons. The TERS measurements show that the effective length scale of the interactions is on atomic rather than nanometric scales. On such scales, optical fields cannot be separated from the surface charge density oscillations that drive them. The interplay between electron vs. photo-mediated coupling of molecule and plasmon is important to disentangle to clarify principles of surface enhanced spectroscopies, and more generally, of plasmon driven molecular chemistry and physics. This consideration is of particular interest in time-domain measurements of vibrational dynamics, which in the single molecule limit, often rely on surface-enhanced coherent Raman scattering (SE-CRS) processes[64]. While frequency domain single molecule SERS[1, 4-13] and TERS[40, 46-47, 100-102] measurements abound, including measurements with ultrafast pulses[54, 64, 103], their time domain implementation proves to be challenging. This challenge, and apparent discrepancies among observations made with short pulses, can be attributed to the efficient up-pumping of molecular vibrations in the process of plasmon damping. This can be readily concluded from the anti-Stokes versus Stokes scattering intensities of SERS spectra recorded with ps pulses and their contrast with

their cw analogues. The consistency between observations and interpretation is further verified through simultaneous ps-SRS and ps-CARS measurements. The fundamental mechanism of SERS is also addressed through the analysis of AS/S scattering intensities. Anomalous AS/S ratios in SERS have been reported previously[4, 11, 104-110], and are typically understood in terms of optical pumping[4, 111], although other mechanisms have been proposed[106, 112]. In the present, it is found that the enhancement of scattering rates is consistent with the Purcell effect, which for the leaky cavities is fairly color independent.

2.2 Methods

The measurements are carried out on the nanoscale analog of the Hertzian dipolar antenna, consisting of gold nanosphere dimers. The commercially obtained nanodumbbells (Cabot, Inc.) are promoted with 1,2-Di(4-pyridyl)ethylene (BPE) molecules, then encapsulated in silica (shell thickness of 40 – 70 nm).

These experiments were performed using a conventional inverted optical microscope equipped with galvo scanning mirrors. For single particle SRS and CARS measurements, the microscope was coupled to a coincident pair of 76 MHz pulse trains of 7 ps duration, emanating from the tunable output of an Nd:Vanadate pumped optical parametric amplifier (PicoTrain, High-Q; Emerald OPO, A.P.E.), which served as a probe pulse. The remaining fundamental output at 1064 nm was modulated at 10 MHz and served as the pump pulse. The collinear pump and probe pulse train was focused at the object plane via a high numerical aperture objective lens (40x oil, 1.32 NA). Images were obtained by raster scanning the excitation pulse train in the *xy* plane at a rate of 10 us per pixel over an area of 100 x 100 um while recording the transmitted or reflected probe in the forward or backscattered directions, respectively. The forward scattered probe was collected with a

1.45 NA oil condenser and focused onto a reverse biased silicon photodiode (Thorlabs Inc., FDS100). The signal was amplified by 60 dB using a voltage preamplifier (Femto Inc., HVA-10M-60-B) and demodulated at 10 MHz with a lock-in amplifier (Zurich Instruments Inc., HF2LI). CARS spectra were acquired in the back-scattered direction by sweeping the pump laser frequency from 905.0 to 913.5 nm with 0.5 nm steps.

Pulsed and cw spectra SERS were acquired in the back-scattered direction by separating source and Raman photons with dichroic beam-splitters that were matched to the excitation wavelengths of 785 nm (pulsed) and 633 nm (cw). Paired notch filters were also included in the collection path for further filtering of the source. A cooled camera spectrograph (Andor iDus 401, Shamrock SR303i) equipped with a 300 lines mm^{-1} grating blazed at 500 nm was utilized for acquiring spectra. Typical integration times were 1 s for cw and 30 s for ultrafast excitation. The galvo mirrors were used to reposition the excitation laser for targeting individual dimers. By recording the SERS in the backscattered geometry, signal photons were relayed to the spectrograph via the excitation galvos. This ensured that the system remained telecentric and permitted Raman acquisition from individual, diffraction limited objects in the focal volume.

2.3 cw-SERS vs. ps-SERS

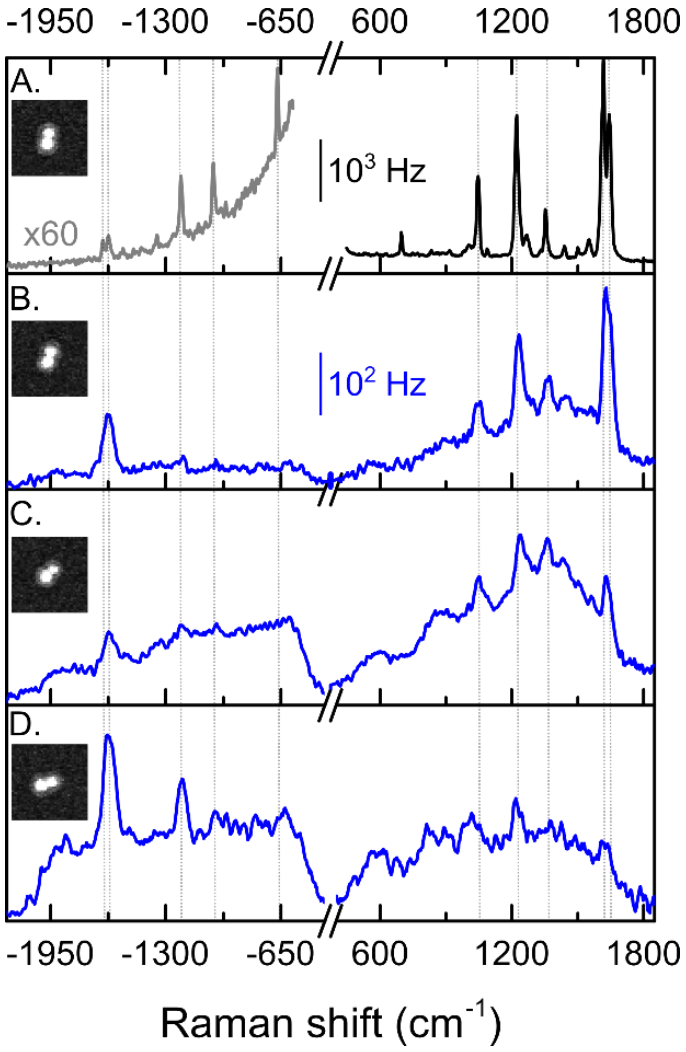

Figure 2.1 Stokes and anti-Stokes SERS spectra recorded on single nantennas: (A) continuous wave excitation (634 nm, 30 μW μm-2), (B,C,D) pulsed excitation (785 nm, 7 ps, 80 MHz, 100 μW μm-2). In all cases the polarization of the incident field is aligned with the long axis of the dimer. Micrographs of each dimer, acquired after the SERS measurements, are shown in the insets.

SERS spectra recorded on different nanodumbbells, under cw and pulsed excitation with a 7 ps pulse train, is presented in Figure 2.1. Stokes and anti-Stokes branches are simultaneously recorded using a notch filter to block the Rayleigh line. An additional bandpass filter is used in the ps-SERS spectra, hence the roll-off at shifts of ±1900 cm^{-1}.

Under cw illumination, the nantenna and its molecular load can be expected to be in thermal equilibrium; and this is verified by the cw-SERS spectrum. In addition to the vibrational lines of the molecule, the electronic Raman scattering (ERS) spectrum of the metal can be seen in the magnified AS branch (gray trace in Figure 2.1 A). The profile of the ERS is determined by the joint density of electron-hole states, which for large spectral shifts ($\Delta E = E_e - E_h$) reduces to the Boltzmann distribution. The profile can be fitted with different levels of sophistication to extract the electron temperature. The extracted temperature $T_e = 385\ K$, is in fairly good agreement with the temperature obtained from the AS/S intensity ratios of the vibrational lines:

$$\frac{I_{AS,v}}{I_{S,v}}\left(\frac{\omega_S}{\omega_{AS}}\right)^3 = e^{\frac{-\hbar\omega_v}{k_B T}} = \frac{N_{v=1}}{N_{v=0}} \qquad (2.3.1)$$

The temperatures extracted from the five prominent vibrations, v, seen in the spectrum of Figure 2.1 A agree within a few percent (T_{avg} = 394 ± 20 K, see Appendix 2.5.2). The relation, (2.3.1), seems to hold over the 3000 cm^{-1} range spanned by the vibration pairs. Similarly, the AS-ERS continuum does not show any spectral coloration, as would be expected if nantenna resonances determined SERS rates. This holds for over 100 nanodumbbells investigated through their cw-SERS spectra, both at 532 nm and at 634 nm excitation, which flank the transverse and longitudinal resonances seen discussed in detail in Section 1.3. Note, the Stokes branch of the ERS shows strong contributions from scattering on plasmonic resonances (coherent luminescence), which have been investigated through polarization resolved Raman studies[113]. Given the spectral inhomogeneity illustrated by the dark field spectra (Section 1.3), it would seem that the SERS rates are practically independent of the plasmonic resonances seen in the extinction spectra. The same is implied by the utility of

(2.3.1), which otherwise is only rigorously valid for normal, spontaneous, non-resonant Raman scattering (see Appendix 2.5.1).

The contrast between cw-SERS and ps-SERS spectra is rather remarkable. The intensity in the AS channel has increased by three orders of magnitude, scaling with the peak intensity of the ps-excitation. The electronic temperatures are significantly elevated, evident by the slopes of the AR-ERS continua (see Appendix 2.5.2). Moreover, the molecular vibrational populations are athermal; and in the case of the spectrum in Figure 2.1 D, the vibrational populations are inverted. This is most clearly seen by the inversion of the AS/S intensity ratio of the 1600 cm^{-1} mode, which after correction for all instrumental response and using eq. 1, yields $N_{v=1}/N_{v=0} = 1.2 \pm 0.03$. While the 1250 mode is not inverted, its population ratio $N_{v=1}/N_{v=0} = 0.52 \pm 0.06$ would correspond to a $T_v = 3400\ K$. In contrast with the thermally equilibrated AS lines where the intensities/populations are progressively lowered as a function of vibrational energy, the highest energy states carry intensity, while the lower lines are lost in the ERS of the hot electron background.

It is fairly easy to be convinced that the molecular vibrations are not optically pumped. To be able to see AS lines in the ps-SERS spectra, ν = 1 must be prepared within the 7 ps width of the pulse, therefore a SERS pumping rate of $I_L\sigma_S^*$ = 10^{11} s^{-1} is required. As indicated by the scale bars in Figure 2.1, the observed average scattering rates are ~ 10^3 s^{-1}, which after accounting for the fill-factor of the ps pulse train, corresponds to $I_L\sigma_S^*$ = 2x10^6 s^{-1}, nearly 5 orders of magnitude short of the required pumping rate. Indeed, Raman pumping can compete with thermal occupation of vibrations upon resonant excitation of bright dyes, which is most convincingly demonstrated at cryogenic temperatures[104]. The effect is negligible in the present non-resonant SERS governed by electromagnetic enhancement

factors. The Raman cross section of the brightest vibrational mode in BPE is $\sigma_s = 5 \times 10^{-28}$ cm^2 and the operative overall enhancement factor is 10^8, sufficient to observe single molecules, but not enough to drive the system away from thermal equilibrium. An alternative optical pumping mechanism with short pulses was recently offered in terms of nanocavity optomechanics[11, 112]. Given the relatively low quality-factors, the mechanism is difficult to reconcile with the population inversion in a single mode, or the preferential up-pumping of the high frequency modes, or the observed very high electron temperatures.

Rather than optical pumping, the data suggests vibrational excitation by electron to vibration (e-v) energy transfer. Both the hot vibrations and hot electrons are simultaneously seen in the ps-SERS spectra. Indeed, in cavities that involve atomic scale separation between molecule and metal, it would be difficult to detach the enhanced local field of the plasmon from the surface charge density oscillations that drives it. Scattering on molecular adsorbates, or dirty surfaces, is a common mechanism for activating intraband electronic transitions and accelerating the damping of surface plasmons. For an e-v pumped vibration to develop a line spectrum, after the impulsive excitation, it must be decoupled from the electron bath during the observation period, within 7 ps in the present. This provides the selection principle for seeing the high frequency vibrations. The impulsive excitation of the 1600 cm^{-1} mode would require the dynamic perturbation to have Fourier components on $1/\nu = 20$ fs time scale. This is well within the dephasing time of plasmons, ~ 5 fs, but an order of magnitude shorter than the thermalization time of electrons through e-e scattering. Rather than hot electrons, the inverted vibrations must be prepared by the coherent charge density oscillation of the plasmon, during its dephasing. To survive, the vibration must remain above the phonon temperature, which develops within the pulse. This explains the

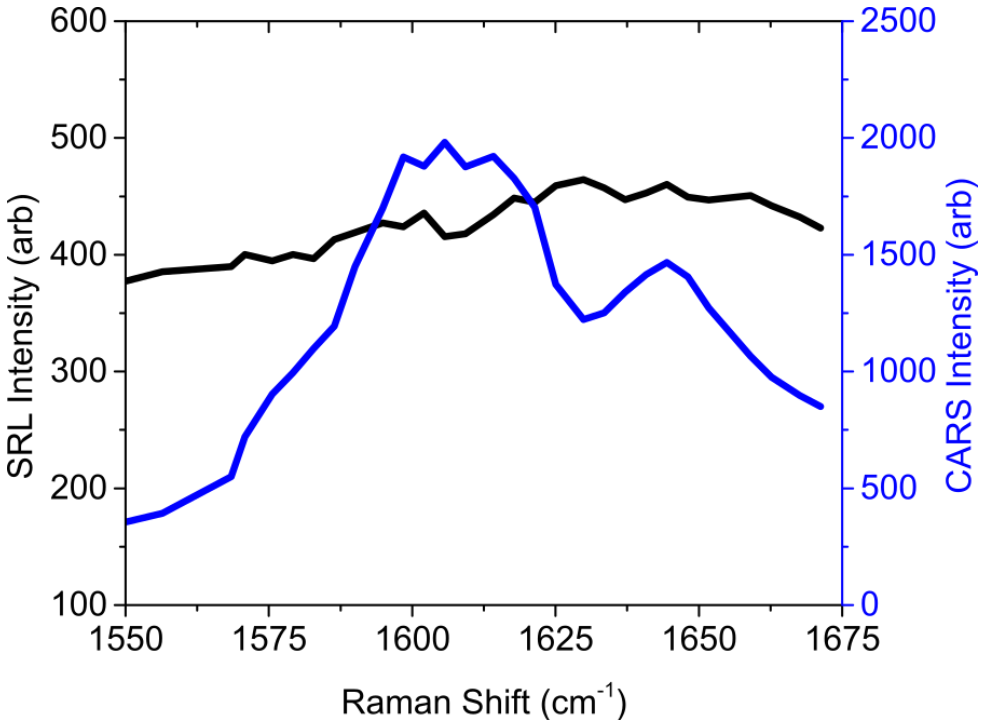

Figure 2.2 Simultaneously recorded SR loss and CARS on an ensemble of nantennas. The CARS channel tracks the 1604 and 1640 cm^{-1} mode of BPE. The featureless SRL channel reflects the lack of phase coherence between the interrogating pulse and the e-mediated preparation.

selective preparation and detection of the high frequency modes, while the low frequency modes that are prominent in the cw-SERS spectrum blended in the electronic background in ps-SERS.

The above model is directly verified through simultaneous SRS and CARS measurements carried out with the ps pulse train. The experimental arrangement is included in Section 2.2. The particular measurements are carried on an ensemble of dry mounted and well dispersed nanoantennas, which contain a distribution of dimers and larger aggregates. The simultaneously recorded SRS and CARS data are shown in Figure 2.2. The SRS channel carries a large signal, which however is entirely featureless. The CARS channel clearly shows the 1600 cm^{-1} doublet. SRS requires phase coherent preparation of the vibrational packet, which evidently is not the case. CARS interrogates the SRS prepared packet through the same

AS scattering process seen in the ps-SERS spectra. The requirement of coherence between preparation and interrogation periods to develop the CARS signal in ensembles, is entirely relaxed in the single molecule limit. Single molecules are impervious to pure dephasing, in the strong coupling regime they develop a stochastic phase, which does not prevent their detection through AS-Raman scattering. A detailed description of CARS in the single molecule limit has been presented in prior time resolved measurements[64].

2.4 Conclusion

Ultrafast and non-linear implementations of the SERS effect directly access dynamical coupling between plasmons and molecules. This was demonstrated through cw and ps-SERS carried out on the prototypical dimer nantenna in the wavelength range that simultaneously accesses the Stokes and anti-Stokes branches. The extracted vibrational populations for the cw case are in excellent agreement with the room temperature thermal distribution of phonons in conjunction with modest heating via the pump laser. The latter was verified independently via Fermi-Dirac statistics for electron-hole pair states extracted from the AS branch of the metal coherent luminescence. The far-field AS/S ratio for cw excitation is dominated by the cubic dependence of scattering on frequency as opposed to the underlying plasmon resonances that enable SM detection. Under pulsed excitation, the AS/S ratios indicate vibrational population inversion which cannot be explained by optical pumping. Direct plasmon-molecule energy transfer is proposed as a mechanism to account for the large $\nu = 1$ population observed. The coherent charge density associated with plasmon excitation contains the frequency components necessary to drive a vibrational population out of equilibrium, which is not the case for either hot electrons or a large phonon population.

This model is directly verified by simultaneously acquired SRS and CARS measurements on the same system. SRS requires the preservation of phase coherence between the preparation and interrogation steps, which is disrupted by driving the interrogation step during the vibrational lifetime. In contrast, in the SM limit, CARS only requires an incoherent hot vibration to scatter from. As a manifestation, the SRS signals on single nantenna are dominated by the electronic response of the metal, which simultaneously report AS molecular information via CARS. Overall, these experiments clarify the mechanism of vibrational state population in surface-enhanced Raman, which has important implications for nanoscale thermometry and for the fundamental mechanism of SERS, which involves coherent electrons.

2.5 Appendix

2.5.1 Vibrational populations and enhancement

In normal spontaneous Raman (SR), the scattering rate:

$$R_{SR} = I\sigma \tag{2.5.1}$$

is given by the differential cross section:

$$\frac{d\sigma}{d\Omega} = \frac{16\pi^4}{\lambda_s^3 \lambda_i} \langle \hat{e}_s \cdot \alpha_{si} \cdot \hat{e}_i \rangle, \tag{2.5.2}$$

integrated over the experimental solid angle Ω of detection. The λ_s^3 recognizes the spontaneous nature of the process, with photons scattered into the vacuum density of states. The total rate in a given channel is given by the number of scattering centers in the excitation volume, in their initial states. For a two-level system, the population ratio N_1/N_0 can be obtained from the AS and S scattering rates (intensities) by taking into account the acceleration of AS/S scattering rates due to the increase in the vacuum density:

$$\frac{N_1}{N_0} = \frac{I_{AS}}{I_S} \left(\frac{\lambda_{AS}}{\lambda_S} \right)^3. \tag{2.5.3}$$

In SERS, it is useful to separate enhancement factors $\beta_{i,s}$ of the incident field and the scattering rate:

$$R_{SERS} = (\beta_i^2 I_i)(\beta_s^2 \sigma_s) = I_L \sigma_s^*. \tag{2.5.4}$$

The incident field is enhanced by the ratio of local and applied fields, $\beta_i = E_L/E_0$. The scattering is enhanced by the local cavity provided by the nantenna, namely by the Purcell factor (Note, s stands for scatter, while S stands for Stokes):

$$\beta_s^2 = F = \frac{3}{4\pi^2}\frac{\lambda_s^3 Q}{V} \tag{2.5.5}$$

determined by the quality factor, Q, and mode volume, V, of the cavity. Plasmonic nantennas are leaky due to both ohmic and radiative damping. Based on extinction resonances (see Figure 1.1), Q ~ 7. The cavity volume is principally geometric, although its estimates greatly vary from pico- to nano-volume. This in part is due to the fact that the orientation and location of the molecule relative to the cavity determines the coupling. An estimate that seems operative here, based on observed enhancements, would be the product of the junction gap and surface area occupied by the plasmon, $V = 4\pi r^2 g$. Two extreme limits arise. If Q/V is treated as constant, substitute (2.5.5) in (2.5.4) in (2.5.3) to see that the spectral corrections disappear:

$$\frac{N_1}{N_0} = \frac{I_{AS}}{I_S} \tag{2.5.6}$$

This is somewhat odd. Since the cavity will have to ultimately re-emit into the far field, (2.5.3) is restored. Thus, in the limit of leaky cavities, (2.5.3) remains valid in SERS. In the limit of bright cavities, the ratios are entirely determined by the plasmonic resonances, but in a nontrivial way. Not all modes couple to the junction, not all junction modes couple to the molecule, and dark modes do not couple to the far-field.

2.5.2 cw-SERS AS/S ratios

The AS/S ratios presented here were extracted by taking the ratio of integrated Gaussian fits of the molecular lines. These data are shown in Table 2.1 for the cw experiment presented in Figure 2.1. Within the estimated error, the molecular temperatures calculated for each mode using (2.5.1) are in agreement. The average temperature of 394 ± 20 K may

Mode (cm^{-1})	molecular SERS		[b]AS ERS background	
	I_{AS}/I_S (10^{-4})	[a]temp (K)	I_{AS}/I_S (10^{-4}) (430 K)	I_{AS}/I_S (10^{-4}) (385 K)
660	753 ± 49	406 ± 26	906	704
1025	126 ± 2.0	360 ± 24	240	162
1200	69± 5.4	381 ± 30	126	80
1604	19± 2.0	407 ± 44	30	16
1637	18 ± 2.3	415 ± 52	26	14

[a]Calculated based on (2.3.1) using the experimental ratios.

[b]Calculated based on (2.3.1) using the temperature extracted through either a Boltzmann fit (second to last column), or a cubic corrected Boltzmann fit (last column) to the AS-ERS.

Table 2.1 Comparison of the experimentally extracted AS/S ratios and temperatures for the molecular SERS and AS-ERS.

be compared to the same for the metal extracted by fitting the AS-ERS to an exponential decay. This reveals a metal temperature of 430 K. Better agreement is observed, however, by including the cubic correction in the exponential fit, which softens the decay constant. The extracted value of 385 K is close to the vibrational temperature estimated through the AS/S ratio. This is shown graphically in Figure 2.3 A along with the fitted ERS signal.

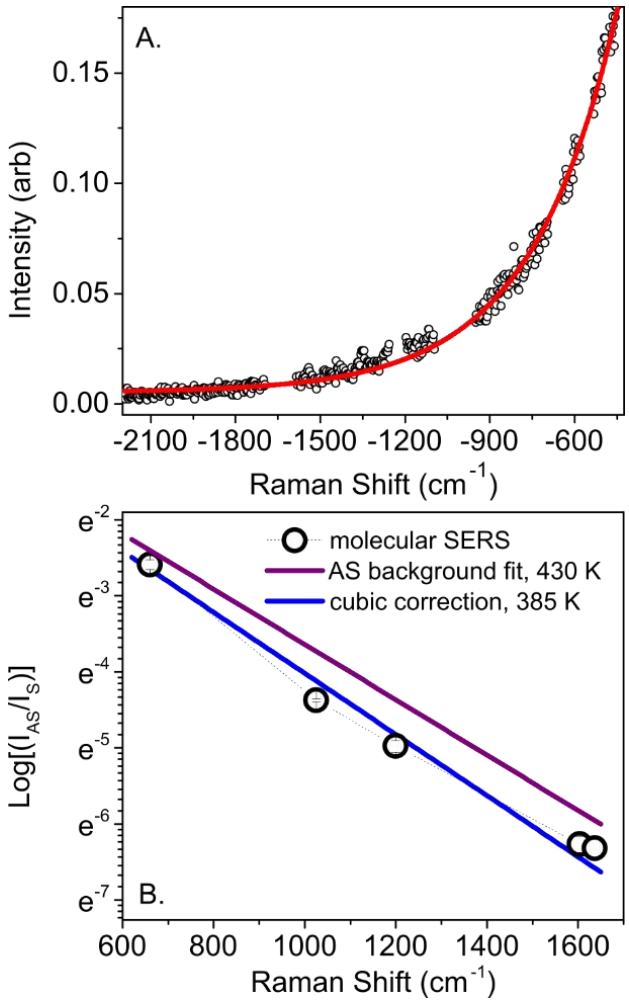

Figure 2.3 (A) Exponential fit to the Anti-Stokes ERS signal corrected for the cubic dependence on scattering for far-field radiation. (B) AS/S ratios for each of the prominent vibrational modes presented in Figure 2.1 A (open circles) plotted alongside the same for the ERS signal. The latter was computed using (2.3.1) and the temperatures extracted though pure exponential (purple trace) and cubic corrected exponential (blue) fits.

2.5.3 ps-SERS AS/S ratios

dimer (Fig. 3)	SERS (1600 cm^{-1})		AS ERS background
	[a]I_{AS}/I_S	[b]$N_{v=1}/N_{v=0}$	[c]temp (K)
B	0.23 ± 0.05	0.12 ± 0.03	3300 ± 2600
C	0.48 ± 0.08	0.27 ± 0.04	2400 ± 450
D	2.2 ± 0.06	1.20 ± 0.03	3100 ± 1700

[a]Corrected for the instrument response.

[b]See (2.3.1).

[c]From fits using (2.5.7).

Table 2.2 Experimentally extracted AS/S ratios, vibrational populations and electronic temperatures for pulsed excitation (data shown in Figure 2.1).

The procedure described above was also utilized to extract the AS/S ratios for pulsed SERS experiment (see Figure 2.1). These data are shown in Table 2.2. The AS branches of the ERS continua were fit to (2.5.7) and are shown in Figure 2.4.

$$s(\upsilon) = \left(\frac{\upsilon_0 + \upsilon}{\upsilon_0}\right)^3 e^{\frac{-\hbar c(\upsilon_0+\upsilon)}{k_B T}}. \qquad (2.5.7)$$

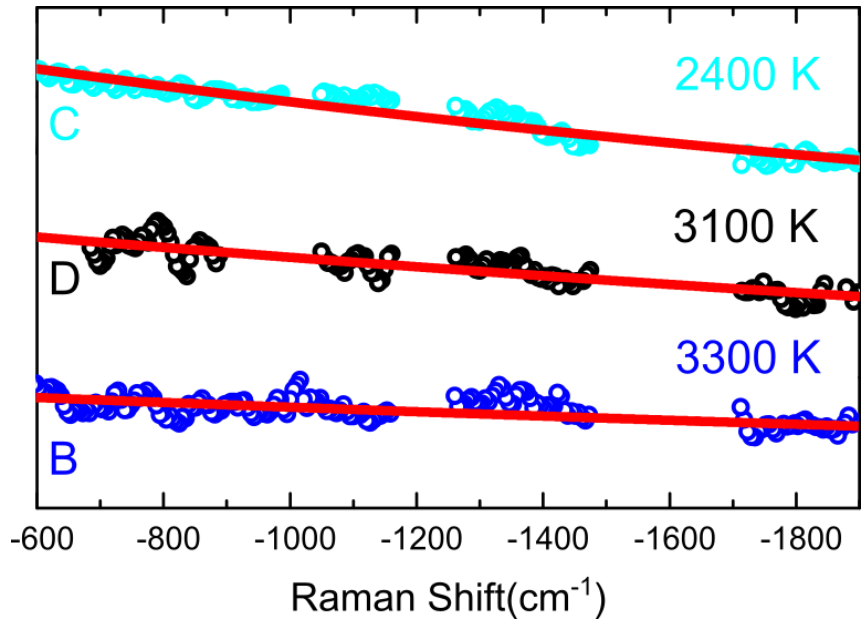

Figure 2.4 AS ERS continua for the particles shown in Figure 2.1, fitted using (2.5.7). The extracted temperatures are shown for each particle.

3 Single molecule coherent Raman in time and frequency

3.1 Introduction

Ultrafast implementations of the SERS effect are capable of probing the early-time (femtosecond to picosecond) dynamics of molecules in isolation. Such approaches take advantage of the enhanced scattering cross sections of molecules in the vicinity of plasmonic junctions and the increased sensitivity of third-order nonlinear optical processes over conventional Raman[54-55]. Surface-enhanced coherent anti-Stokes Raman scattering (SECARS) represents the non-linear analog of SERS and has emerged as a powerful tool to effectively translate the principles of SERS into the ultrafast limit.

The recent literature includes several accounts of surface-enhanced coherent anti-Stokes Raman scattering (SECARS)[55-58, 60-61, 66, 114] and stimulated Raman scattering (SESRS)[50, 69] experiments. In all of these cases, although short pulses are used, the measurements were carried out in the frequency domain. Frequency domain measurements contain information about the shortest time interactions that control ultrafast dynamics, and the existing examples suggest important differences between a given nonlinear scattering process and its SE analog. For example, the SESRS measurements on colloidal nanosphere dimers show dispersive vibrational lines[50]. In contrast, while heterogeneous ensemble SECARS studies report dispersive lineshapes[115], SECARS on individual plasmonic nanostructures show nondispersive lines[114], similar to those seen in cw-SERS. These observations contradict expectations based on standard implementations of SRS and CARS on ensembles. Since CARS is given as the square of the third order polarization, it shows interference between the electronic continuum and discrete molecular transitions[116]. Along the same consideration, since SRS is proportional to the imaginary part of $P^{(3)}$, it does not

heterodyne with the background. However, since the phase-shifted signal in SRS co-propagates with the stimulating beam, interference is unavoidable. These considerations are less clear when the interaction with the molecular load is mediated via the nantenna, since now a new source of phase delay between molecule and plasmon is introduced. It is then valuable to compare SECARS versus SESRS carried out on the same plasmonic nanostructure, and more generally to establish design considerations and fundamental limitations of time-resolved SE nonlinear optics (SE-NLO). As important is the distinction in information content of time domain versus frequency domain measurements using short pulses. These are the motivations behind the studies reported here.

In what follows, frequency domain SECARS measurements on the prototypical dumbbell nantenna are reported. The nantenna substrates consist of a gold nanosphere dimers, the same system used in the reported SESRS measurements[50], and on previously reported time-domain SECARS measurements using femtosecond (fs) pulses[64].

3.2 Methods

3.2.1 ν-domain SECARS

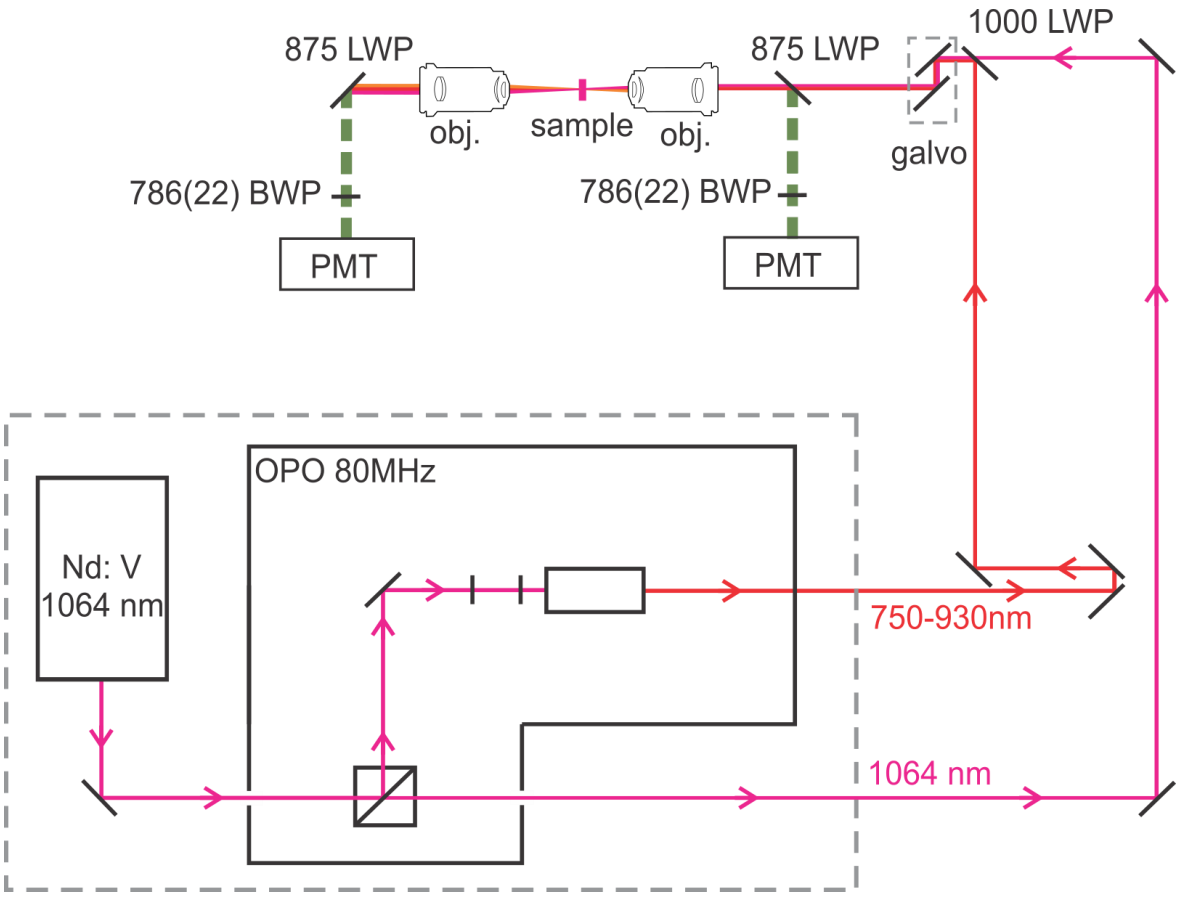

Figure 3.1 Schematic of the CARS microscope. Either galvo mirrors or a scanning stage are used to collect backscattered CARS images at each time delay, or at each frequency. The images are stacked to extract the photon count rate as a function of the dynamic variable (ν or t). The forward scatter channel is dedicated to cw-SERS, detected through a series of filters and a fiber-coupled spectrograph.

The system and methods employed in the *ν*-domain ps-SECARS studies that reported here are similar to those utilized for ultrafast SERS (Section 1.2.3)[64]. These measurements employ 7 ps pulses with bandwidths (6 cm^{-1}) much smaller than the ~35 cm^{-1} spacing between the targeted 1604 and 1640 cm^{-1} lines. The measurements are carried out in imaging mode, using an optical microscope adapted to simultaneously measure cw-SERS and

tr-SECARS (see Figure 3.3). The nantennas are dry-mounted on the SiN membrane (50 nm thick) of a transmission electron microscopy grid. They are first characterized and mapped-out via scanning electron microscopy, then collocated on the optical microscope using backscattered light. A coincident pair of 76 MHz pulse trains is used for the ps-SECARS measurements: The 1064 nm output of a Nd:Vanadate laser (PicoTrain, High-Q) serves as the Stokes pulse, and a tunable optical parametric oscillator (Emerald OPO, A.P.E.), which is scanned from 905.0 to 913.5 nm with 0.5 nm steps, serves as pump and probe. The combination generates difference frequencies ranging from 1550 cm^{-1} to 1660 cm^{-1}, which covers the spectrum of the bright C=C modes. The collinear beams are focused on the grid plane with a high NA objective (40x oil, 1.32 NA) in a laser-scanning inverted microscope (Fluoview 300, Olympus). At each frequency increment, a 92 μm x 92 μm area of the grid is scanned with a dwell time of 10 μs/pixel (Figure 3.1). The approach allows the simultaneous interrogation of ~50 dumbbells that fall within the scanned area. The anti-Stokes radiation is filtered (875 nm edge, 787 (22) bandpass; Semrock) and detected using a photomultiplier tube (R3896, Hamamatsu).

3.2.2 t-domain SECARS

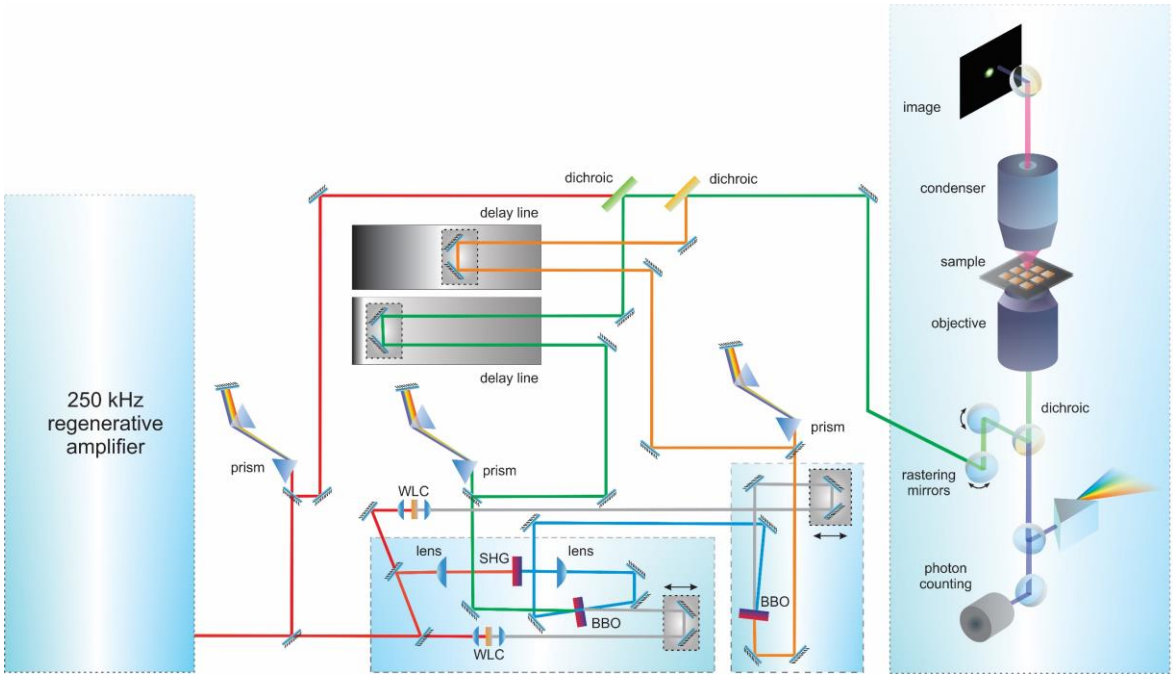

Figure 3.2 Schematic of the 250 kHz, 3 color fs laser apparatus for time-resolved SECARS. Two home-built NOPA's are sequentially pumped by a regenerative amplifier seeded by a Ti:sapph oscillator running at 80 MHz (40 fs, 800 nm). Each NOPA consists of two stages: 1) supercontinuum generation in 3 mm thick sapphire windows and 2) second harmonic generation in a 0.3 mm thick type I beta barium borate (BBO) crystal. The resulting WLC seed and 400 nm pump are focused into a 3 mm thick type II BBO crystal for NOPA generation. The remaining 400 nm pump is collimated and used as the pump source for a second NOPA which utilizes the same configuration. The NOPA's and remaining fundamental are temporally compressed to ~ 100 fs using a folded prism configuration.

Time-resolved SECARS measurements on individual nantennas are carried out using two different three-color, 100 fs sources, designed to carry out background-free measurements. The first consisted of two home-built, sequentially pumped non-collinear optical parametric amplifiers (NOPA). The pump source consists of 250 kHz regeneratively amplified Ti:sapphire laser (Mira Seed/REGA 9000, Coherent). A schematic of this system is shown in Figure 3.2. The second consisted of an 79 MHz Ti:Sapphire pumped photonic crystal fiber (PCF), tailor-made for SE-NLO[79]. This system will be discussed in detail in

Chapter 5. As was established in Chapter 1. the requirement for such measurements is an agile source of multicolor fs pulses at high repetition rate and low intensity, with typical pulse energies of 100 fJ in 100 fs (100 μW at 100 MHz repetition rate). These specifications are based on fundamental limits in peak and average intensity that a nanojunction can tolerate. Both sources were configured to prepare and probe the same vibrational superposition interrogated in the ps-SECARS experiments. An APD (SPCM-AQRH-25, Excelitas) or a PMT (R6358, Hamamatsu) operating in photon counting mode is used for detection of the photons emanating from the sample at the anti-Stokes frequency.

3.3 SECARS spectra

SECARS spectra recorded on six dumbbells are shown in Figure 3.3, along with the cw-SERS spectra recorded after the measurement on the same nantennas. Scanning electron micrographs recorded before and after the ps measurements did not show a noticeable change in the gross structure of these nanostructures. The recorded envelopes of the SECARS spectra can be seen to

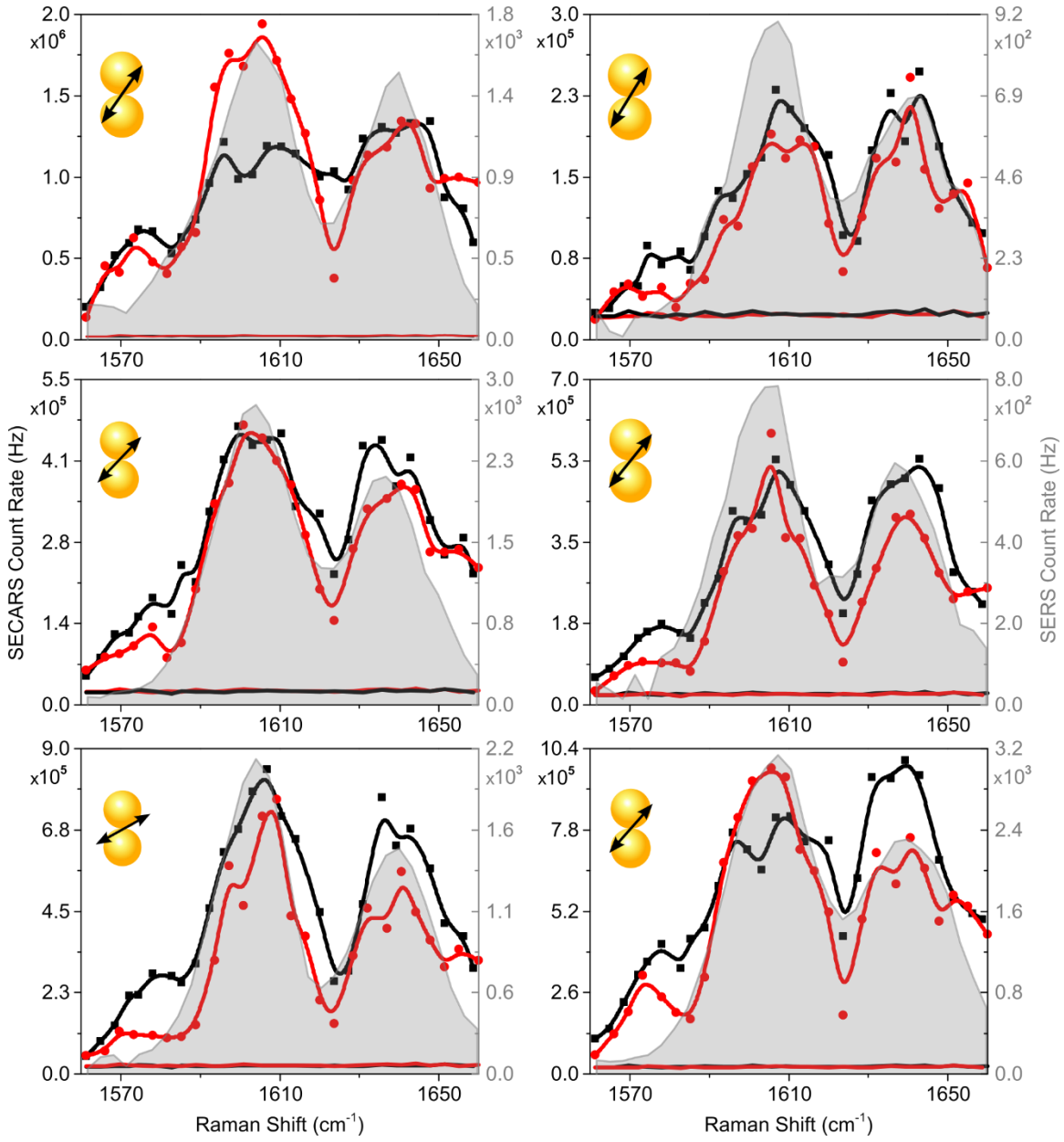

Figure 3.3 SECARS spectra recorded on different dumbbells (red and black traces) and the cw-SERS spectra (gray, shaded) recorded on the same structures after the SECARS measurements. Consecutive SECARS measurements on each particle are reported: 1st acquisition in red, and 2nd acquisition in black. Also shown are the off-particle, background signals associated with each measurement. For the SECARS spectra, illumination conditions were as follows: $I_{Pu,I}$ = 525 μW μm^{-2} and $I_{St,I}$ = 260 μW μm^{-2} corresponding to peak incident intensities of 9 x 10^{7} W cm^{-2} and 5 x 10^{7} W cm^{-2}, respectively. The relative orientation between laser polarization and nantenna is shown in the insets. The SERS spectra are recorded with a depolarized 633 nm cw laser (I_i = 10 μW μm^{-2} = 1 x 10^{3} W cm^{-2}).

be in good agreement with those of the SERS, which exhibit Gaussian lineshapes of ~20 cm^{-1} FWHM. The noticeable difference is the jagged appearance of the SECARS spectra, due to under-sampling of the heterogeneous distribution betrayed by the Gaussian profiles. The cw-SERS spectra are recorded with 10 s exposure, during which the distribution is continuously sampled. The accumulated sampling time in the SECARS spectra is ~1.5 ns per point (dwell time × rep rate × pulse width). Evidently, the sampling time in the ps-SECARS measurement is shorter than the time required to achieve ergodicity of the accessible phase space. Another important distinction is the contrast between the spectrum observed in the present ν-domain SECARS and the inferred spectrum from the prior t-domain measurement[64]. There, decoherence times as long as ~10 ps were extracted for the two-state superposition, equivalent to a linewidth of ~3 cm^{-1}. The discrepancy is understood by recognizing the unique difference in t- versus ν-domain measurements in the single molecule limit. Recall that CARS measures the square of the third order polarization[14]:

$$S(t) = \left| \int dt \mathcal{E}(t) \sum_{v} a_v \exp(-i(\omega_{v,0} + \Omega)t - \gamma_v t \right|^2 \qquad (3.3.1)$$

in which $\mathcal{E}(t)$ and Ω are the slow envelope and frequency of the probe pulse, and the summation is over the vibrational superposition prepared by the pump and Stokes pulses. With a pulse duration of 100 fs, much longer than vibrational periods $2\pi/\omega_{v,0}$ = 20 fs but shorter than the vibrational beat period $2\pi/(\omega_v - \omega_{v'})$ = 1 ps, the probe envelope acts as a time window that filters out only the difference terms $\omega_{v,v'} = |\omega_v - \omega_{v'}|$ in the product (3.3.1)[117]. This reduces the t-domain signal to the cross correlation between vibrations:

$$S(t) = \sum_{v,v'} a_v a_{v'} \exp(-i(\omega_{v,v'})t - \gamma_{v,v'}t). \qquad (3.3.2)$$

In contrast, line profiles in SERS, as in spontaneous Raman, reflect the autocorrelation of individual vibrations:

$$S(\omega) = \left|\int_0^\infty dt\, e^{-i\omega t} \sum_v a_v \exp(-i\omega_v t - \gamma_v t)\right|. \qquad (3.3.3)$$

The ν-domain SECARS spectrum recorded with a 7 ps probe pulse, yields the Ω-shifted copy of the SERS spectrum, as seen in Figure 3.3 and predicted by (3.3.1). While not clear at the outset, the ν-domain ps-SECARS recorded on a single nantenna does not contain information that is not already present in cw-SERS. In contrast with ensemble measurements, in the single-molecule limit, ν-and t-domain measurements are not simply Fourier related. In the present, the spectral covariance measured in t-domain is much smaller than the variance observed in ν-domain spectral linewidths. This is consistent with the two vibrations sampling the broad inhomogeneous distribution in a highly correlated fashion, which implies that the two vibrations are driven by common environmental fluctuations. Moreover, the observation that ps-SECARS does not show any incremental broadening over SERS, implies that the light driven forces under the ps pulses are not perceivably different than in the case of cw illumination.

3.4 Measurement yield

The data shown in Figure 3.3 are those of survivors, which represent ~30% of the dumbbells imaged on the grid. The particles are randomly oriented on the grid, while the laser polarization is linear and fixed. Consistent with the strong dependence of enhancement factors on the polarization of the incident field (see Section 1.3), it is found that the modes of signal degradation on individual dumbbells are correlated with their orientation on the grid. In Figure 3.4, measurements on 46 dumbbells are summarized by binning them into four categories: (i) The set of survivors, exemplified by the data in Figure 3.3, are dumbbells with long axis oriented at 45°±15° relative to the incident polarization. (ii) The set in which SECARS spectra decay during the course of measurement clump up near 30°±15°. The post

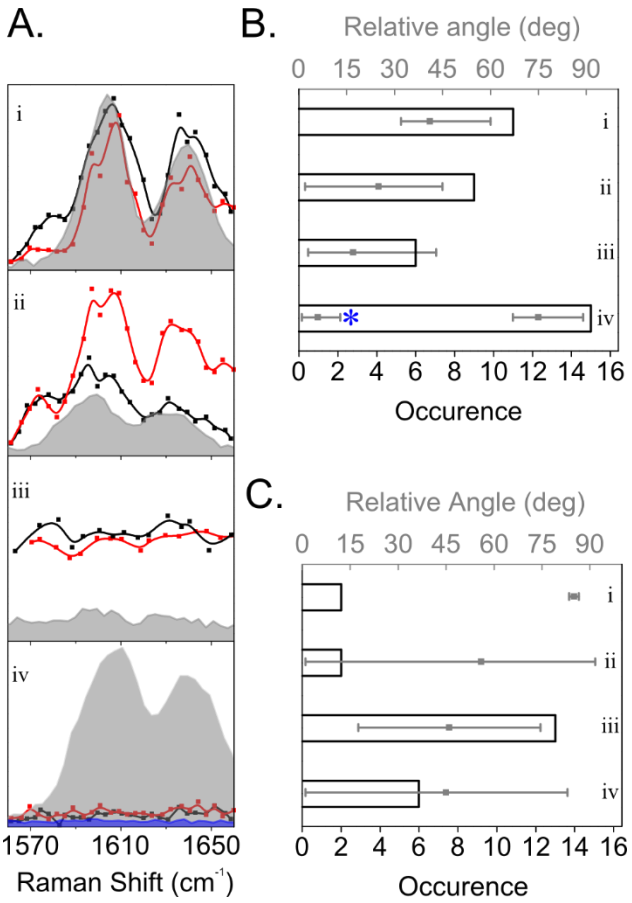

Figure 3.4 Statistics of survival organized in four categories, according to behavior illustrated in (A) by consecutively recorded ps-SECARS spectra (red and black traces for 1st and 2nd acquistions) and subsequent cw-SERS (gray, shaded). The bar graphs show the correlation of the categories with orientation of the dumbbells relative to the polarization of incidence: (B) At peak pump and Stokes pulse intensities 9 x 10^7 W cm^{-2} and 5 x 10^7 W cm^{-2} (C) The same correlation upon he intensity in each arming the peak intensities to 5 x 10^8 W cm^{-2} and 1 x 10^8 W cm^{-2} for pump and Stokes, respectively.

mortem SERS spectra on these dumbbells are either very weak, or strongly perturbed. In several cases, the BPE molecular lines are replaced by a new line at ~2350 cm^{-1}, which is assigned to CN, and take as evidence for photo-dissociation of the pyridines. (iii) The set aligned near 17° shows strong electronic CARS void of any molecular signal. Their post-mortem SERS is similar to the second category: the spectra are either highly perturbed or exhibit very weak BPE molecular features. iv) Dumbbells that do not yield SECARS are either perfectly aligned with the *E*-field or perpendicular to it. The post-mortem cw-SERS on the

aligned nantennas is limited to ERS – the molecular SERS has entirely bleached. Nantennas that are perpendicular to the polarization, retain an intact molecular SERS, reinforcing that the nano-junction is inaccessible in transverse pumping (see Section 1.3).

Finally, the fraction of dumbbells that survive measurements is reduced from 30% to 8% upon doubling the intensity (see Figure 3.4 C). Since the enhanced local field changes dramatically with polarization angle of incidence, the observed orientation dependence confirms that rather than the incident field, it is the enhanced local field that induces degradation of the molecular SECARS signal. Yet, the local field, which plays the most critical factor in experimental considerations, is most difficult to quantify; hence the reliance on the computed values.

3.5 Saturation of stimulated steps in tr-SECARS

The tr-SERS signal considered in (1.5.1) is for spontaneous Raman (SR), a two-photon process in which a pump photon is absorbed and a Stokes photon is emitted. CARS is a four-photon process, which can be decomposed into stimulated Raman scattering (SRS) followed by SR. The expected SECARS count rate may be expected to scale as:

$$R_{SE-CARS} \propto (\beta_{Pu}^2 I_{Pu})(\beta_{St}^2 I_{St})(\beta_{Pr}^2 I_{Pr})(\beta_{As}^2 \sigma_{As}). \qquad (3.5.1)$$

The first two terms on the right hand side in (3.5.1) correspond to SRS, whereas the last two terms represent spontaneous anti-Stokes Raman. Coherence among scatterers that distinguishes CARS in ensembles is irrelevant in measurements on single scattering centers. As such, the second step in CARS scales with the rate of SR, but now acting on the vibrationally excited molecule(s) prepared through SRS. Therefore, the photon yield in tr-SECARS must be reduced relative to tr-SERS by the efficiency of the initial SRS process. Yet,

the photon count rates of 10^5 - 10^6 Hz seen in the ps-SECARS in Figure 3.3 are 2-3 orders of magnitude larger than the cw-SERS count rates. Even after making due allowance for differences in β-values and *ff*, the ps-SECARS counts remain 1-2 orders of magnitude larger. This necessarily implies that the stimulated steps in SECARS are near saturation. The same conclusion can be reached by noting that the rate of stimulated versus spontaneous radiation scales by the occupation number of photons, n, in the stimulating mode[118]:

$$\frac{R_{SRS}}{R_{RS}} = \frac{(n+1)}{1} = n \qquad (3.5.2)$$

Even if mode confinement by the nantenna is ignored, the typical number of incident photons per pulse of $n = 10^7$ can be expected to amplify the observed SERS count rate $R_{RS} \sim 10^3$ s^{-1} to an SRS rate of $R_{SRS} = 10^{10}$ s^{-1}. This is two orders of magnitude larger than the repetition rate of the laser. As such, it may be concluded that the interrogated vibrational coherence is prepared with every pulse, *i.e.*, the SRS step is saturated. Recent reports, which demonstrate SRS saturation of electronically non-resonant molecules at peak intensities of $\sim 10^{11}$ W/cm^2, echo this conclusion[119]. The applicability of (1.5.1) to tr-SECARS is contingent on saturation of the stimulated steps, which is verified by the count rates seen in SERS and SECARS as a function of *ff*.

Since there usually is a reserve of incident laser intensity in typical pulsed setups, the fundamental advantage in tr-SERS reduces to the quadratic enhancement of the cross section $\sigma_s^* = \beta_s^2 \sigma_s$. That is, since stimulated steps are easily saturated (3.5.2), rather than the β^8 enhancement suggested by (3.5.1), detectability in time-resolved SECARS reduces to the

consideration of (1.5.1); namely, the quadratic enhancement of the spontaneous cross section and maximizing the fill factor.

3.6 Plasmon mode matching

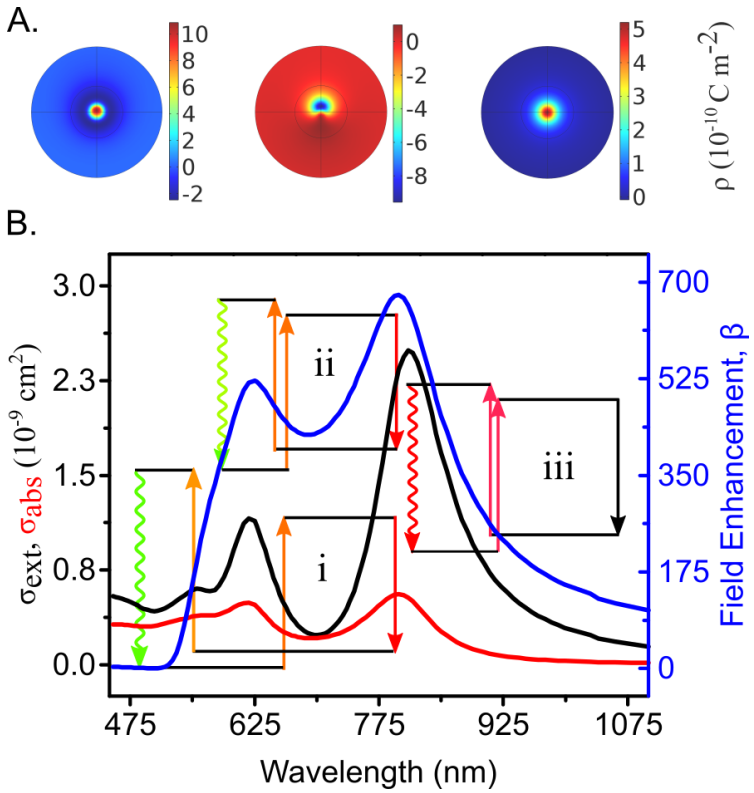

Figure 3.5 (A) Computed charge density distributions at the junction between the spheres for an applied field of 1 V/m at 555 nm (left), 618 nm (center), and 816 nm (right). (B) Linear spectral response of the nantenna for longitudinal excitation: extinction (black trace), absorption (red trace), and field enhancement factor (blue trace). Time circuit diagrams for the three SECARS measurements discussed are superposed over the spectra to highlight the resonances underlying the different excitations. They consist of (i) tr-SECARS executed with 100 fs pulses, using all three plasmon modes; (ii) tr-SECARS utilizing the dipolar plasmon (pump and dump) and bonding quadrupolar resonances (probe and emission); and (iii) ν-domain SECARS using picosecond pulses, with all four waves coincident on the dipolar resonance.

In two-color tr-CARS measurements, where the pump and probe pulses are derived from the same laser, there is an unavoidable background that arises from the coincidence of all three pulses at t = 0. This can be overcome in 3-color measurements, with distinct *Pu*, *St*,

and *Pr* colors, hence a unique (background-free) 4-wave mix that generates the targeted AS signal. This was accomplished by two different 3-color, 100 fs laser systems, operating at 79 MHz and 250 kHz, respectively. In the case of the 250 kHz system, the dramatic reduction in fill factor $ff = 2.5 \times 10^{-8}$ makes tr-SECARS measurements on single scattering centers rather challenging. Nevertheless, because of the reduction in background, tr-SECARS measurements could be done with results identical to those observed at 79 MHz. The observed tr-SECARS signal is shown in Figure 3.6. It consists strictly of the instantaneous response of the anti-Stokes ERS of the nantenna, with no trace of the time-delayed molecular signal. This is in stark contrast with the ps-SECARS data in Figure 3.3, where the molecular signal appears with negligible ERS background. The colors used in these measurements are contrasted with those of the ps-SECARS measurements against the backdrop of the nantenna resonances in Figure 3.5.

Consistent with all stimulated steps being saturated, the observed count rate in the fs-tr-SECARS signal Figure 3.6 can be directly related to the ps-SECARS count rates (Figure 3.3) through equation (1.5.1). Using the computed enhancement factors, the relative ratio of spontaneous scattering rates alone, $(\beta_{AS}^2 ff / \beta_{AS'}^2 ff') \sim 2 \times 10^3$, rationalizes the observed ratio of count rates between the ps and fs measurements. The contrast of seeing strictly molecular response in the 2-color experiment and strictly ERS of the nantenna in the 3-color experiment, underscores that enhancement factors alone do not determine the signal in CRS mediated via the nantenna. Plasmon mode matching is an important consideration. As in the prior fs tr-SECARS measurements[64], the present ps-SECARS data were obtained with all four waves coupled through the bonding dipolar plasmon. The three-color fs SECARS relies on the bonding dipolar plasmon to prepare the coherence, the bonding quadrupolar plasmon to

probe, and the anti-bonding quadrupolar plasmon to enhance the anti-Stokes signal (see Figure 3.5). As in the cw-SERS spectrum of Figure 1.6, where the molecular anti-Stokes scattering is completely absent at 532 nm; here too, only the ERS of the metal is observed. The opening of the molecule-to-metal scattering channel, which shows strong nonlinearity[94], is operative in the 3-color experiment. This dramatic difference in observables can be generally ascribed to the requirements of plasmon mode matching in nantenna mediated preparation and interrogation of molecular coherences.

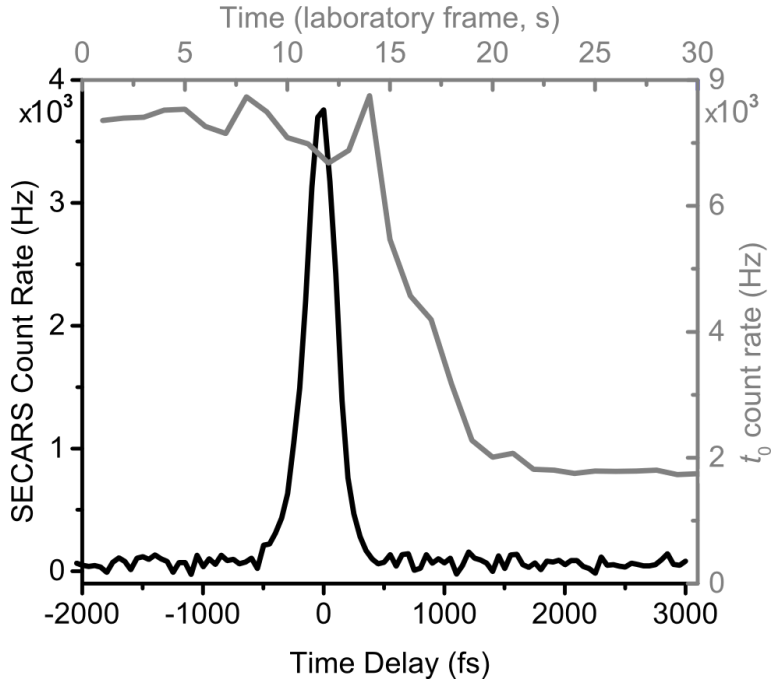

Figure 3.6 Time-resolved signal (black trace) from a dumbbell obtained through 3-pulse 3-color CARS (scheme i Figure 3.5 B), illustrating the metal response at t = 0 and the absence of a molecular signal at positive time. Gray curve: The time course of the t = 0 response of a dumbbell decays after an induction period of ~15 s, suggesting collapse of the nanojunction.

The electronic anti-Stokes Raman scattering of the nantenna is enhanced by the junction plasmon. The signal strength decays when the junction fuses. An example of what appears as a catastrophic decay of the t = 0 signal is shown in Figure 3.6 (gray trace). The junction collapses after an induction period of ~15 seconds, which underscores that peak

intensity arguments alone do not explain the damage. Evidently, irradiation induced slow evolution of the junction, *e.g.,* through thermal and electro-migration induced mobility of surface atoms, precedes the catastrophic decay.

3.7 Conclusion

The ν-domain ps-SECARS measurements carried out on single plasmonic nantennas illustrate coherent Raman spectroscopy in the few molecule limit. The recorded spectra are under-sampled copies of the cw-SERS spectra. This is in contrast with the fs-SRS measurements on the same system, which show dispersive lines[50]. The contrast is remarkable because it does not follow expectations based on ensemble measurements. Beside the distinction that the CARS signal cannot interfere with the incident fields, due to its color and scattering geometry, an important distinction is the time ordering of interactions. In SRS, the incident field drives the nantenna, which in turn excites the molecule, and the re-radiation of the molecule is amplified by the nantenna[120]. Ultrafast SECARS on single scattering centers can be understood as a saturated SRS step, followed by surface-enhanced, spontaneous anti-Stokes Raman scattering. Since the final step in which the signal is formed is the same as in SERS, it is perhaps not surprising that the observed line profiles are the same. However, in both SERS and SECARS there is an interplay between the molecular response, ERS of the nantenna, and coupled molecule-metal scattering, which depends strongly on the selected excitation resonances.

The contrast between the line profiles observed in the present *υ*-domain ps-SECARS measurements and those implied by the prior *t*-domain fs-SECARS measurements underscores that in the single molecule limit, the two measurements are not Fourier-related. The *t*-domain CARS yields the cross-correlation among the members of the prepared

vibrational superposition, while the ν-domain measurements yield the autocorrelation of individual vibrational lines. The two are identical in the limit of large ensembles, where the tr-CARS signal can be retrieved through a Fourier transform of the Raman spectrum[79].

More generally, explore the parameter space for designing tr-SE-NLO was explored. The stimulated steps are easily saturated, as such tr-SECARS and tr-SERS scattering rates are determined by the final spontaneous radiation cross section, which in turn is quadratically enhanced: $\sigma_s^* = \beta_s^2 \sigma_s$. This is to be contrasted with the effective quartic, β^4, enhancement in SERS, and the naïve extrapolation that in the four-photon CARS process one may expect β^8 enhancement. The quadratic enhancement of incident fields $I_L = \beta_i^2 I_i$ has the primary advantage of lowering the demand on incident intensity. In this regard, the encapsulated nano-sphere dimer is well suited to interrogate plasmonic chemistry in isolation. Beside the fundamental limits in both peak and average intensities that were extracted from a large number of measurements on single nantennas, an effective mode-matching criterion exists in multicolor experiments. The latter consideration, namely the role of the spatial and temporal coherence of plasmons in coherent Raman scattering deserves further exploration.

4 Atomically resolved tip-enhanced Raman scattering

4.1 Introduction

Tip-enhanced Raman scattering (TERS) may be regarded as the spatially resolved analog of the surface enhanced Raman (SER) effect. TERS effectively combines the chemical specificity of vibrational spectroscopy with the principles of scanning probe microscopy, enabling ultrahigh resolution imaging with chemical contrast. Recent demonstrations have highlighted the utility of scanning tunneling microscopy based TERS (STM TERS), which, when executed under ultrahigh vacuum (UHV) and ultralow temperatures, affords ultimate control and stability over the tip-sample junction[34, 40, 46-47]. STM TERS is therefore ideally suited to address single molecules (SM) and, more generally, to explore the mechanisms that govern optical contrast and resolution in near-field plasmonics.

While conventionally exercised with bare metal tips, TERS via functionalized tips represents a plasmonic construct capable of directly probing interaction potentials and is therefore equipped to map surface and molecular charge density distributions and local forces in the regime(s) relevant to chemistry[47]. From a mechanistic standpoint, the existing examples distinguish themselves from the nominally field-driven concept of SERS, principally due to achieved levels of lateral resolution (> 1 nm). This has sparked progressing theoretical interest into the coupling of electrons, photons and plasmons at nanojunctions, which are difficult to disentangle over the length scales in question[11, 112, 121-122].

In what follows, TERS measurements carried out with a tip terminated with a single metalloporphyrin molecule are presented. TERS maps of an insulating monolayer surface composed of copper nitride (Cu_2N) were recorded under UHV and cryogenic temperatures

(5 K), which ultimately demonstrate atomic imaging via photons. The TERS signals are decomposed in terms of their spectroscopic observables (intensities, frequency shifts and linewidths), which yield fundamentally different information about the Cu_2N surface and the mechanism of SM TERS.

4.2 Methods

These measurements were carried out in a home-built UHV (base pressure $4x10^{-11}$ Torr), cryogenic STM equipped with a parabolic mirror for Raman collection (solid angle 2.7 sr). The focus of the parabola is precisely aligned to the apex of the tip by recording the tip electroluminescence (EL) in imaging mode. The output of a linearly polarized, single mode 634 nm diode laser served as the excitation source for TERS measurements and is focused at the tip-sample junction (45° illumination angle) using an aspheric lens. Scattered photons are collimated by the parabola and set into a 0.3 m spectrograph (Princeton, SpectraPro 2300i) equipped with a LN_2 cooled CCD. The silver TERS tip was prepared as previously described[47]. The tip was further processed in situ by field directed sputter sharpening. The Cu_2N surface was prepared by ion sputtering nitrogen over a Cu(100) single crystal at room temperature. Cobalt(II) Tetraphenyl porphyrin molecules (CoTPP) were later deposited via sublimation, enabling sub-monolayer coverage. A single CoTPP molecule was adsorbed to the apex of an atomically terminated Ag tip by scanning the freshly dosed surface at 0.1 nA tunneling current and a 45 mV sample bias.

4.3 Atomic imaging with a CoTPP reporter

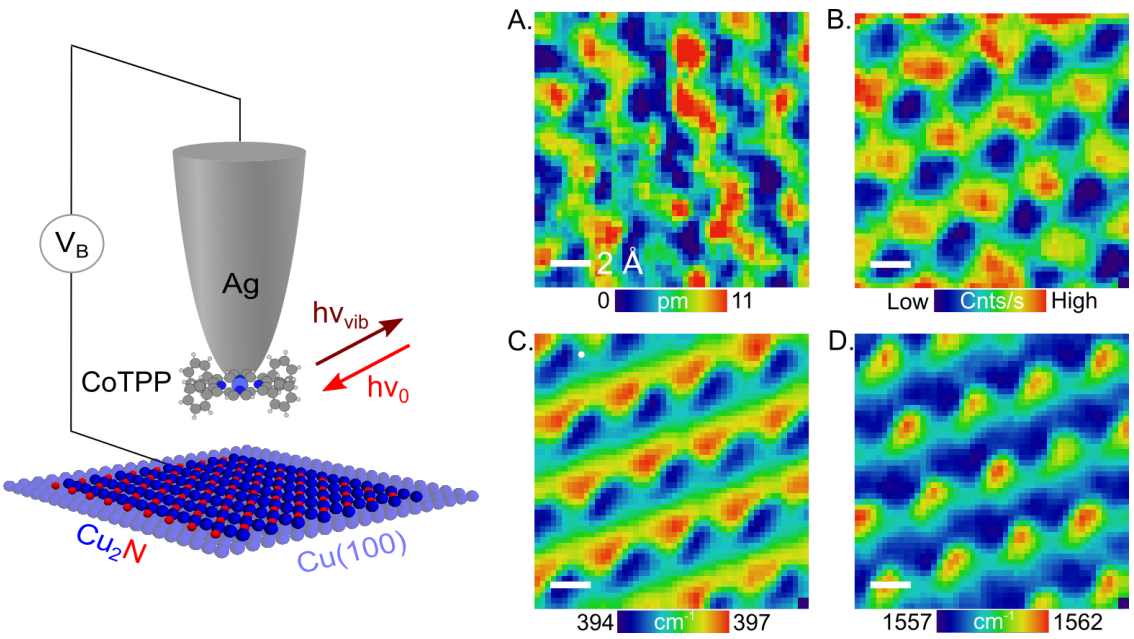

Figure 4.1 Simultaneously recorded (A) STM topography on Cu_2N at a 1 nA and 15 mV set point via CoTPP terminated tip, (B) TERS intensity integrated over the full range from 400 to 1600 cm^{-1}), (C-D) frequency shift maps for the 398 and 1560 cm^{-1} modes, respectively

The tip-side CoTPP vibrations exhibit quantifiable frequency shifts and intensity variations when the vacuum gap is decreased to 2 Å, which, overall, map out discrete components of the atomic lattice on mode-specific basis. This is shown in Figure 4.1 which compares simultaneously acquired STM topography to TERS intensity and frequency shift maps of Cu_2N. The intensity map (Figure 4.1 B) was generated by integrating over the full range (400 to 1600 cm^{-1}) of the CoTPP TERS spectrum. The individual modes map out the same spatial features with varying degrees of contrast. Variations in the center frequencies of selected modes clearly map out atomic corrugation. Line profiles following the depressions in the TERS intensity map are shown below in Figure 4.2. The depressions in the TERS intensity and 398 cm^{-1} frequency shift images are clearly correlated. The same features appear as protrusions at 1560 cm^{-1}. As such, intense regions in the TERS map

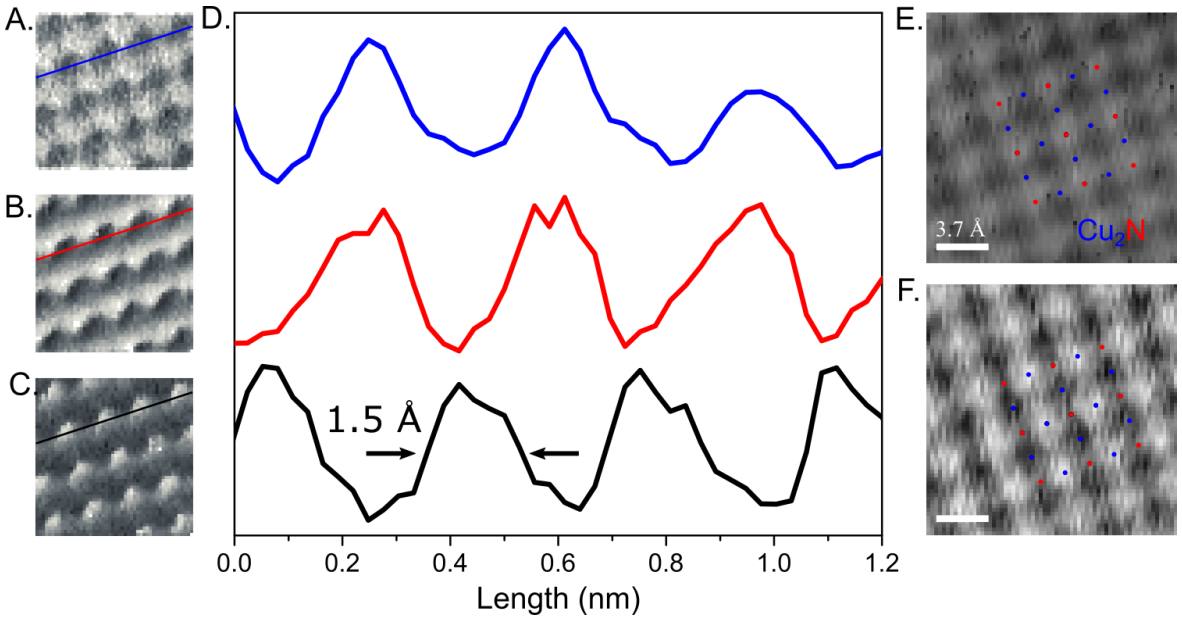

Figure 4.2 (A) TERS intensity, and (B-C) 398 and 1560 cm^{-1} frequency shift maps. Spatial line profiles of were taken where indicated (blue, red and black lines for A, B and C, respectively). (E-F) STM topography acquired at +1 V 0.1 nA (E) and -1 V 0.1 nA (F).

correspond to red shifting of the 398 cm^{-1} mode and blue shifting of the 1560 cm^{-1} mode. Note, the TERS signals are spatially localized to 1.5 Å, slightly beyond the atomic radius of silver (1.72 Å).

At the outset, the Cu_2N registry is not known and must be established. The reconstruction of Cu_2N on Cu(100) is well known and yields an incommensurate c(2x2) lattice[123-125]. For 1 ML coverage, Cu_2N is an insulator with a bandgap in excess of 4 eV. The work function of 6 eV is higher than that of bare Cu(100) (5.1 eV) which has been attributed substrate-adsorbate charge transfer[126-127]. Cu and N species may be distinguished by recognizing *1)* N atoms appear as protrusions at high, negative bias, and 2) the topography inverts at high, positive bias[124]. In addition, N adsorbs at the hollow site of Cu(100)[123, 128-129]. These criteria permit exact identification of Cu and N species in the topography. Positive and negative high bias STM images are compared in Figure 4.2. Based on the criteria

described above, N is assigned to the protrusion at -1 V and the depression to the 4-fold hollow. As anticipated, the contrast inverts at +1V. These assignments are rigorously justified below, where the origin of the frequency shifts is explicitly treated.

4.4 TERS signal retraction dependence

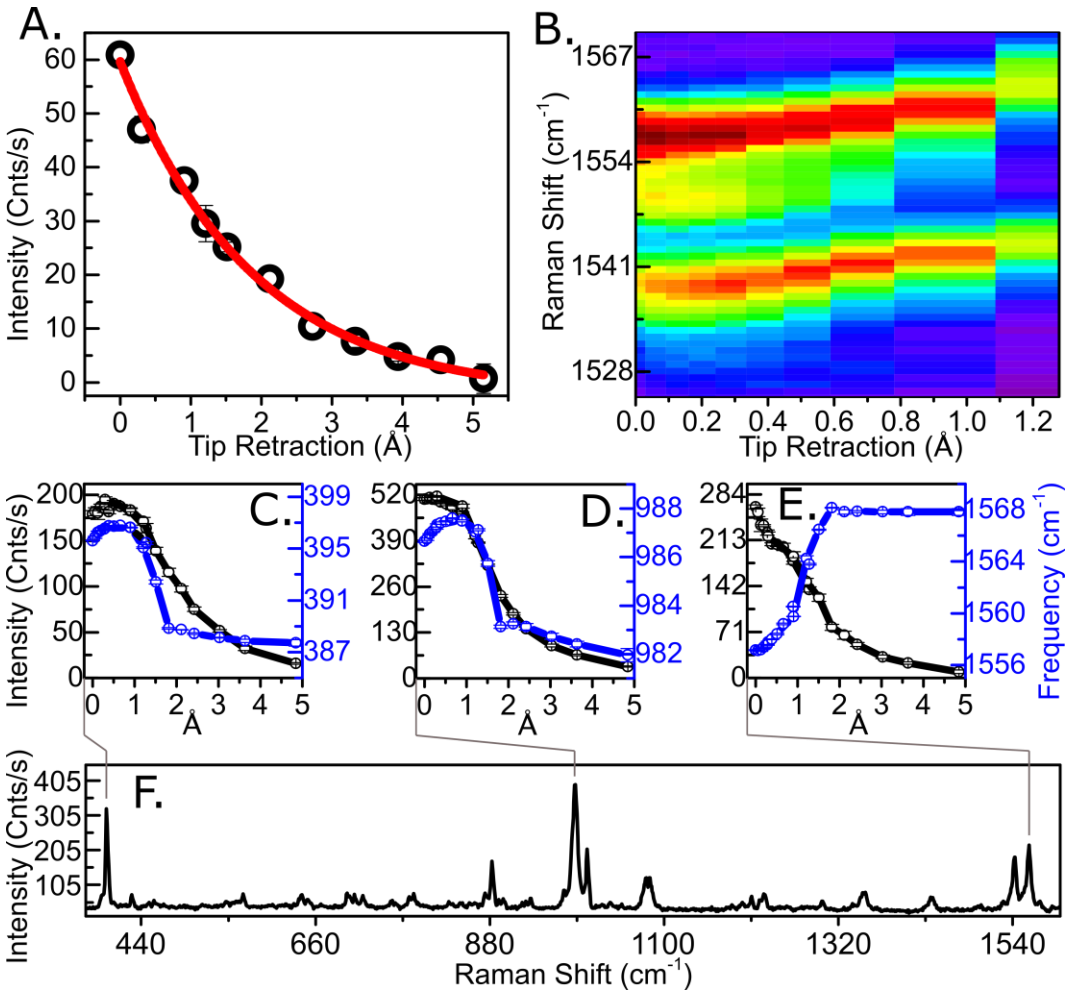

Figure 4.3. Mode-specific retraction dependent TERS intensities and frequency shifts. (A) Retraction curve for the 1560 cm^{-1} mode at a 0.1 nA 10 mV set point exhibiting exponential dependence with a 2 Å decay length (fit: red curve). (B) Evolution of the 1540 and 1560 cm^{-1} modes with tip retraction starting from a smaller initial tip-sample separation (set point: 1 nA -10 mV). (C-E) Intensity (black) and frequency shift (blue) retraction curves for 390, 985 and 1560 cm^{-1} modes, respectively, taken at the latter set point (1 nA -10 mV). The TERS intensity and frequency shifts saturate for the first ~1 Å for the 390 and 985 cm^{-1} modes. (F) TERS spectrum of the tip adsorbed CoTPP molecule. Note, (A) was recorded at the N site while (B-E) were collected at the Cu site.

The TERS signal is laterally confined to dimensions reaching 1.5 Å, enabling atomically resolved imaging. The transverse confinement of the TERS signal is explored through tip

retraction dependence. In Figure 4.3, The TERS intensity variation with vacuum gap distance is presented for selected modes.

In these measurements, TERS spectra were recorded as a function of tip retraction for two different initial tip-sample separations, g_0. For the larger g_0, established by a 0.1 nA 10 mV set point, the TERS intensity decays exponentially with retraction and exhibits a decay length of 2 Å. This is exemplified by the 1550 cm^{-1} retraction curve, which is shown in Figure 4.3 A. When g_0 is decreased by changing the set point to 1 nA and -10 mV, the individual modes exhibit distinct retraction profiles. This is highlighted in Figure 4.3 B for the 1540 and 1560 cm^{-1} modes which blue shift with increasing gap length. While the 1550 cm^{-1} increases in intensity as the tip is engaged, the 1540 cm^{-1} mode saturates near ~ 0.6 Å and subsequently decreases. Intensity and frequency shift retraction profiles taken over an extended range are shown in Figure 4.3 C-E for the 380, 985 and 1560 cm^{-1} modes at the same set point. The intensity of the modes at 380 and 985 cm^{-1} increase exponentially till ~ 1.5 Å where saturation is evident. The frequencies of these modes roughly track the profiles of the intensity dependence, and biexponentially red shift until ~1.5 Å, where the shifts plateau and subsequently change sign. In contrast, the intensity of the 1560 cm^{-1} mode monotonically increases and blue shifts as the gap length decreases.

4.5 TERS signal bias dependence

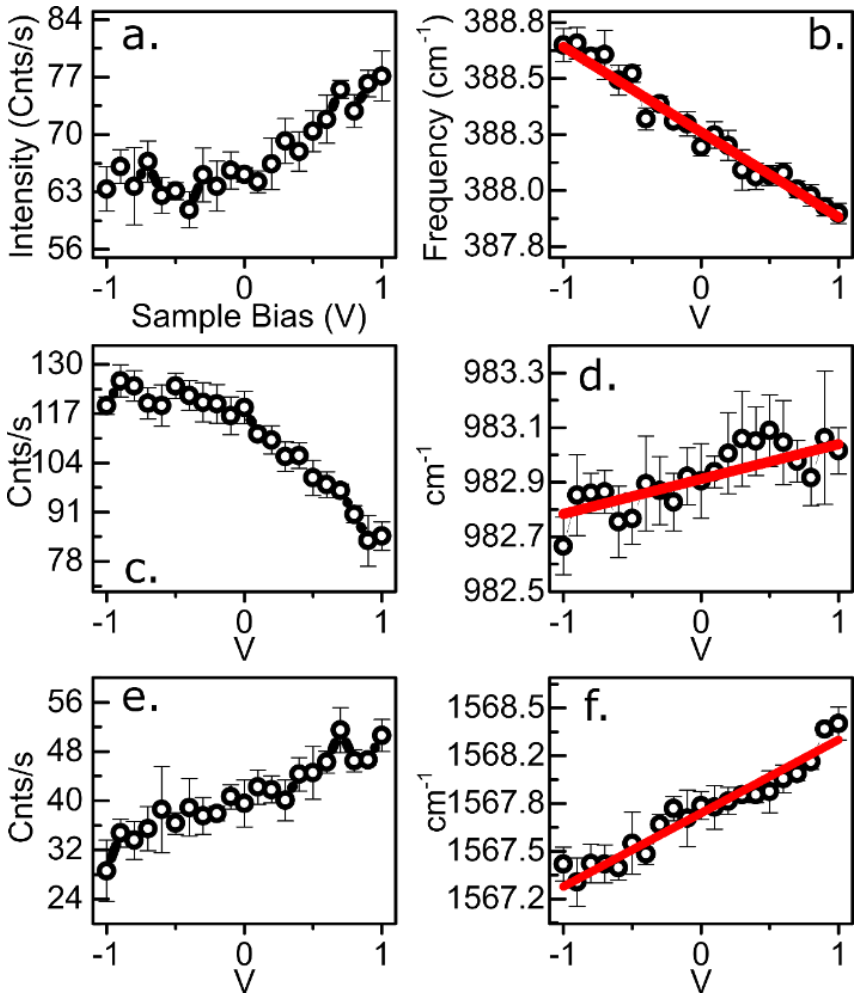

Figure 4.4. Sample bias dependent TERS intensities (left column) and center frequencies (right column) for 388 cm^{-1} (A, B), 983 cm^{-1} (C, D) and 1560 cm^{-1} (E, F). Linear fits to the frequency shift data are shown in red. These data were recorded at the Cu site.

In addition to the variations in the TERS spectra observed when the gap length is tuned, the intensities and center frequencies of the CoTPP modes are sensitive to the applied sample bias. The results of a bias ramp recorded Cu site are shown in Figure 4.4. In these measurements, the applied bias was varied from -1 V to +1 V while the gap length was held constant (current set point 1 nA). Notably, the intensity traces for the 388 and 983 cm^{-1} modes are asymmetric about the zero-voltage crossing; they plateau in the range from 0 to -

1 V. At positive bias, the dependences are roughly linear and exhibit opposite slope. That is, the intensity of the 388 cm^{-1} increases in the range from 0 to +1 V while the opposite is observed at 983 cm^{-1}. The intensity of the high frequency 1560 cm^{-1} mode linearly increases over the full range. For all three modes, the observed peak shifts are linear with bias (see Figure 4.4 B, D, and F). Tabulated Stark coefficients recorded on the N and Cu sites are shown in Table 4.1.

4.6 Origin of atomic resolution

The atomically resolved TERS images imply lateral confinement of the excitation volume to 1.5 Å, which relays the Cu_2N atomic positions into the far-field via the tip-side CoTPP molecule. It is interesting to consider the origin of atomic contrast, which was achieved with what may be regarded as a blunt probe; the CoTPP macrocycle ring itself is 4 Å in diameter, while the phenyl to phenyl distance is larger (8 Å). The tip retraction dependence curves (Figure 4.5) clearly confirm that the CoTPP is located at the apex as opposed to the shaft, which would exhibit gap-independent Raman. The latter may be thought of as SERS arising from tip roughness, and is periodically observed in the ambient[130].

Evidently, the CoTPP normal modes, which are *1)* incommensurate with the Cu_2N lattice, and *2)* largely delocalized throughout the molecule, register atomic features that are 8-fold more localized. This apparent contrast may be explored considering the Raman signature of the CoTPP reporter under an excitation field localized somewhere on the molecule. For Å-scale Gaussian excitation, the Raman signal may be approximated by the polarizability derivative with respect to a normal mode, q, weighted by the constituent atomic displacements of the normal modes that lie within the local field, which is assumed to be a 3D Gaussian:

$$\left| \langle \frac{\partial \alpha}{\partial q_n} \rangle_{g,\rho\sigma} \sum_{i=1,N} \frac{\delta_i}{\sqrt{2}} e^{-\left(\frac{r_i - r_T}{\Delta}\right)^2} \right|^2 . \qquad (4.6.1)$$

In (4.6.1), the leading term describes the ρ, σ tensor component of the the polarizability derivative with respect to the n^{th} normal mode and δ_i is the displacement amplitude of the N^{th} atom. The Gaussian term represents the overlap between the scalar field centered on the tip, r_T, and the equilibrium position of a given atom, r_i, and the summation is over all atoms in the molecule. The denominator, Δ, is the FWHM of the field. Using (4.6.1), and the α-derivatives, atomic displacements and atomic positions retrieved through a DFT ROA analysis (Gaussian09), Raman spectra for various values of Δ, r_T, and α are calculated. Note, the ρ, σ tensor elements are selected by the vector components of the incident field and scattered fields, respectively. In the implementation, these terms are adjustable parameters utilized to obtain the best match with the experiment. The results shown in Figure 4.5 are for *ρ = (1,1,1), σ = (0,0,1)*, denoted α_{zz}, and *ρ = (1,1,1), σ = (0.1,0,1)*, denoted α_{xz}. For a complete derivation of (4.6.1), see Appendix 4.10.2.

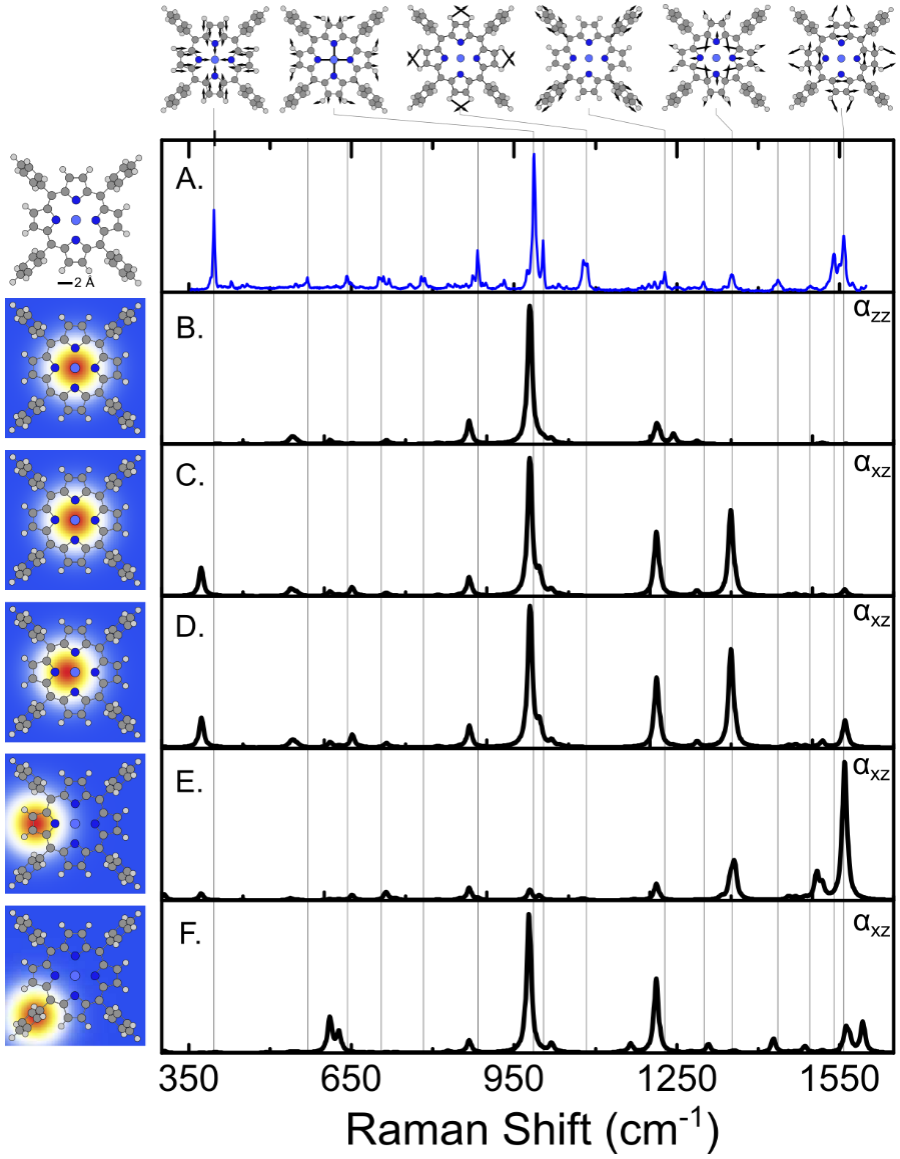

Figure 4.5 Experimental (A) and simulated (B-F, see (4.6.1)) TERS spectra for the apex bound CoTPP under localized Gaussian excitation (Δ=5 Å) and various conditions: (B) α_{zz} component and Co excitation, (C) α_{xz} component and Co excitation, (D) α_{xz} with the excitation centered on the Co-N bond, (E) α_{xz} and pyrrole excitation and (F) α_{xz} and phenyl excitation. The excitation geometries are depicted on the left panel for each spectrum. Top: atomic displacement vectors projected onto the xy-plane for the prominent modes. The theoretical frequencies were scaled by 0.96.

For pure *zz* excitation centered on the cobalt (Δ=5 Å, Figure 4.5 B), the Raman spectrum reflects the bright C=C stretching (979 cm^{-1}) and C-H wagging (868 and 1212 cm^{-1}) modes of the phenyls, which are twisted out of the plane of the macrocycle as evidenced by

the large dihedral (72°). The addition of an in plane contribution to the scattered field (E_z/E_x = 10), denoted $\alpha_{xz,}$ enhances the 1212 cm^{-1} mode, which now tracks the pyrrole C-H's, and generates several new modes: 373 cm^{-1} (macrocycle breathing), 1349 cm^{-1} (coupled Co-N, C-C stretching, pyrrole) and 1560 cm^{-1} (C-C stretching perpendicular to the Co-N axis, pyrrole), which are in fairly good agreement with the peak positions observed in TERS (Figure 4.5 A). Slight lateral displacement of the field by 0.6 Å toward a pyrrole (Figure 4.5 D) enhances the modes near 1560 cm^{-1} and captures the relative intensity trend for the most prominent modes in the TERS spectrum. Direct excitation of the pyrrole selectively enhances the in-plane 1560 cm^{-1} mode which is significantly less intense in the experiment. Similarly, direct excitation of the phenyl moiety fails to capture the distal macrocycle breathing mode at 373 cm^{-1} and generates intense lines at 3100 cm^{-1} (C-H stretch) which were not observed experimentally.

In conjunction with slight displacement of the field toward the pyrrole, the α_{xz} spectrum (Figure 4.5 D) reproduces essential features of the experimental spectrum, suggesting that the molecule is adsorbed to the atomically terminated tip via the Co atom. Taken together, the lack of observable lines at 3100 cm^{-1} in the TERS data, and the overestimated intensity of the 1212 cm^{-1} mode in the simulations suggest the phenyl groups do not feature in the excitation localized on the Co atom. The brightness of the 1349 cm^{-1} mode in the simulated spectra is similarly indicative; for adsorption at the Co site and a modest α_x contribution, the 1349 cm^{-1} mode is expected to dominate over the distal 373 and 1560 cm^{-1} modes, which is captured by the simulation (see e.g. Figure 4.5 D and C). In the experiment, the opposite trend is observed. This may be taken to suggest that the molecule distorts away from planarity upon adsorption on the tip. For a concave distortion, the planar

modes would have finite projections in z that follow the derivative of the curvature of the molecule. This simultaneously explains the brightness of the 373 and 1560 cm^{-1} modes in the experiment, the overestimated 1349 cm^{-1} in the simulation, the silence of the phenyls and the presence of a bright mode at 1078 cm^{-1} in the TERS spectrum, which is enhanced due to symmetry relaxation (see Figure 4.5). In effect, the E_x component required to reproduce the TERS spectrum mimics concavity of the molecule. Moreover, out-of-plane motion of the distal vibrations generates significant polarization at the Co atom, which contains an unpaired electron in its dz^2 valence. This clarifies the origin of atomic resolution registered through the normal modes, which effectively translate distal vibrational amplitude into *z* polarization modulation at the Co, which is efficiently tracked by the tip. Explicitly considering the bond polarizabilities would have the effect of significantly reducing the required width of the field, which, in the simulations was 5 Å.

4.7 Electrostatic model

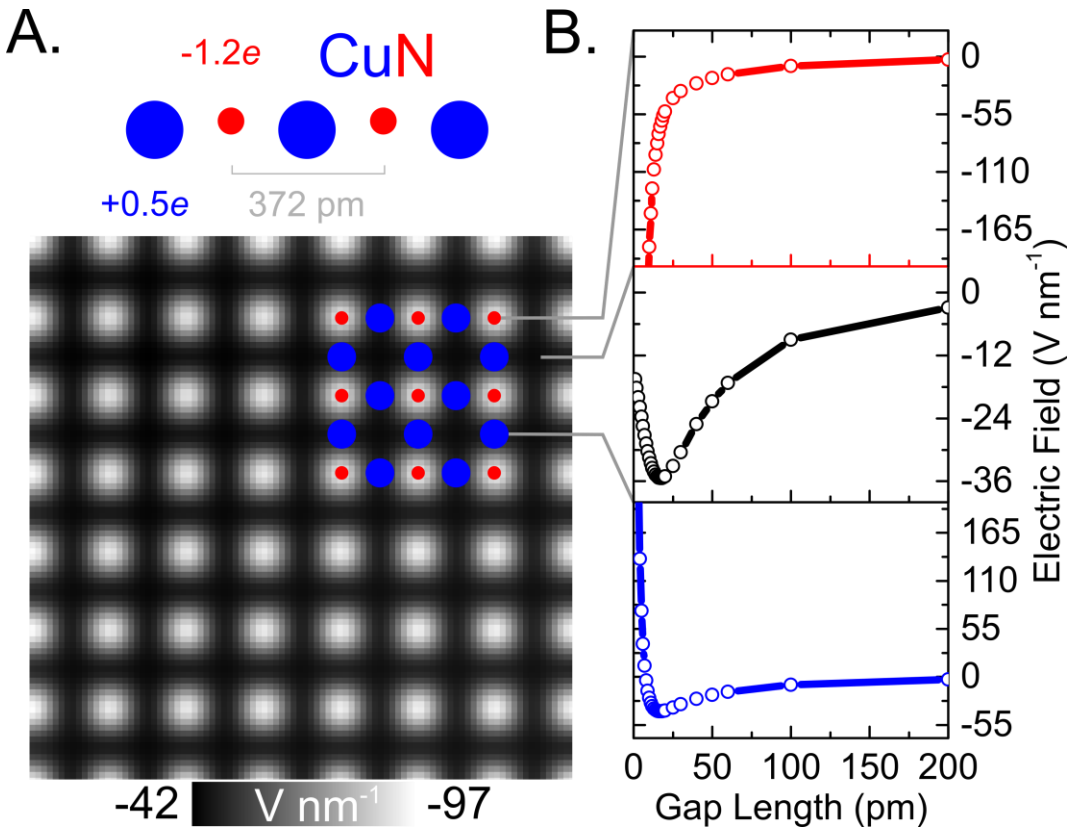

Figure 4.6 Electrostatic model for Cu_2N TERS ν-shift imaging. (A) Cross section of the constructed lattice indicating the atomic charges and lattice constant (upper). Lower: total electric field resulting from the point charge distribution on the surface recorded at a constant height of 1.5 Å (inset: Cu_2N lattice). (B) Total field as a function of z-position (height) for fixed positions on the surface (blue: Cu, black: 4-fold hollow site, red: N).

The atomically resolved TERS ν-shift maps suggest significant Stark shifting of the CoTPP vibrational modes, which is considered here using an electrostatic model. The total electric field at the tip apex is considered through a 3D point charge representation of the Cu_2N monolayer. Literature values are utilized for the structural parameters of the surface which exhibits a 3.72 Å lattice constant. The N atoms are known to be vertically displaced from Cu by 21 pm[126]. The Cu_2N lattice is ionic, reflecting a significant charge transfer from Cu to N upon adsorption. The net charge on each species has been determined to be -1.2*e* for

N and +0.5e for Cu[131]. In the current model, the charges are placed at the atomic core positions. Using this framework, a Cu_2N lattice consisting of 14x14 unit cells was constructed.

The total electric field simulated at a constant height of 1.5 Å from the surface is shown in Figure 4.6. Due to the lattice stoichiometry and the significant charge transfer that occurs upon Cu_2N formation, the net charge on the surface is negative and ranges from -42 to -9.7 V $Å^{-1}$. As a result, the positive electrostatic contribution due to individual Cu atoms is suppressed, making them indistinguishable from the 4-fold hollow site. For z-positions below $\sim$1 Å, the diverse surface charge distribution becomes apparent in the height dependent total field, which is shown in Figure 4.6 B for the Cu (blue), N (red) and the four-fold hollow site (black). While the N site exhibits purely inverse-square dependence on z-position, the sign of the field inverts for the Cu and hollow sites, reflecting the vector-charge additive contributions of each species.

This model provides realistic estimates for the local field in the TERS junction due to the charge distribution on the surface. The local field may be mapped onto the CoTPP molecular vibrations through the linear Stark interaction:

$$\bar{\nu}(E_L) = \bar{\nu}(0) - \Delta\mu E_L. \qquad (4.7.1)$$

In equation (4.7.1), $\bar{\nu}(0)$ is established by the vibrational frequency of a particular mode in the limit of an infinite gap (zero field). Moreover, the bias dependent ν-shifts (see Appendix 4.10) quantitively establish the magnitude and sign of the Stark coefficient $\Delta\mu$, by taking into account the tip-sample gap distance, g_0. For an estimated gap of 1.5 Å, the experimental slopes from the bias ramp translate into 0.57 and -0.75 cm^{-1}/V/Å for 388 and

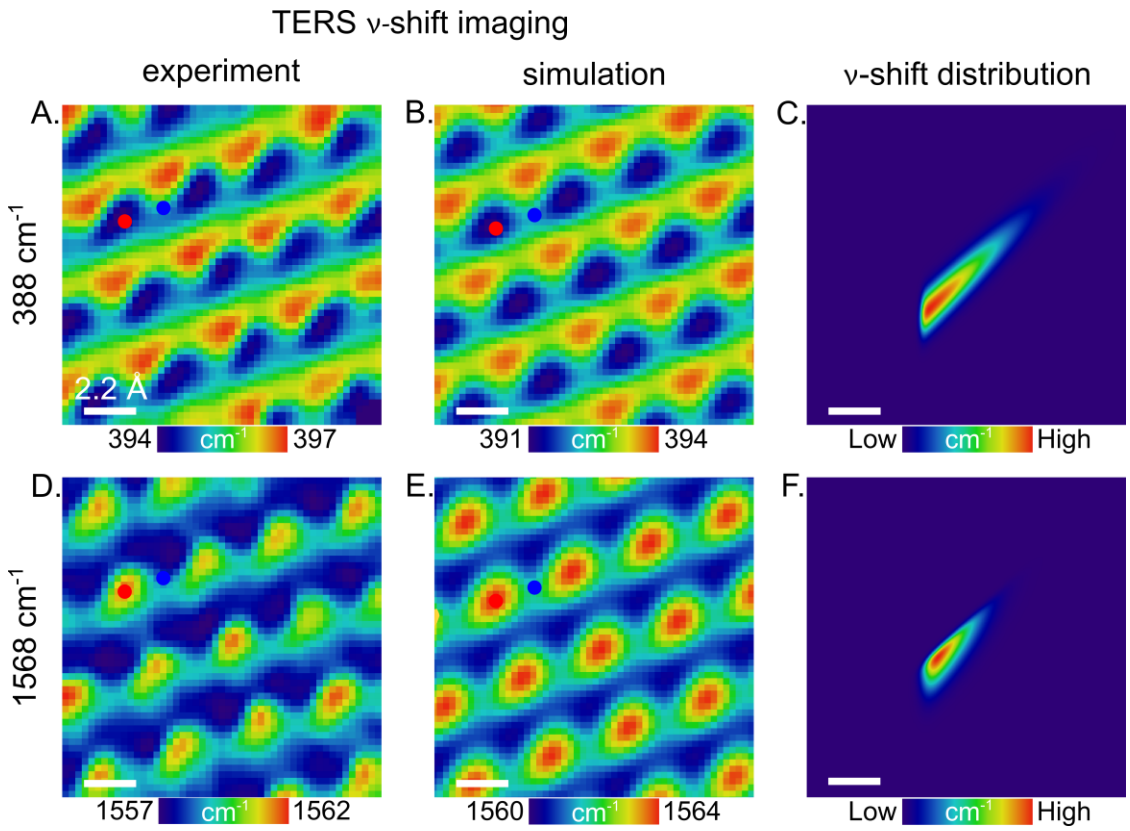

Figure 4.7. Experimental and simulated ν-shift maps for the 388 cm^{-1} (A, D) and 1568 cm^{-1} (D, E) modes of CoTPP. Red and blue dots indicated the positions of N and Cu respectively. The experimentally derived skew functions are shown in (C) and (F) for 388 and 1568 cm^{-1}, respectively.

1568 cm^{-1} respectively. Note, at a fixed position above the surface, vibrational modes will exhibit a distribution in ν-shifts owning to the presence of a distribution of orientations relative to the tip axis. The translation from the orientational distribution of the vibrational density to ν-shift results in a skewed population. As such, topographical features such as spatial charges will appear asymmetrically broadened. In the present, the parameters for the spatial distribution function are retrieved from cross sections of the TERS images, which are fit to skewed Gaussian distributions. As such, reproduction of the time-averaged vibrational frequency involves a 2D spatial convolution:

$$\bar{\nu}(x,y) = \bar{\nu}(0) - \Delta\mu \iint E_L(x-x', y-y') f(x', y') dx dy \qquad (4.7.2)$$

Here, f(x′, y′) is the skew function represented by the normal distribution multiplied by its integral. Using these values, the simulated local field and the extracted skew functions, the TERS ν-shift maps may be simulated. This is shown in Figure 4.7 which compares the experimental (Figure 4.7 A, D) and simulated (Figure 4.7 B, E) ν-shift images for the 388 and 1568 cm^{-1} modes. There are several notable features. First, the local field established through the electrostatic potential due to the ions effectively captures the magnitude and sign of the frequency shift for each mode. The 388 cm^{-1} mode exhibits an overall blue shift and an additional 3 cm^{-1} variation that maps out atomic corrugation. On the N site where the local field peaks (Figure 4.7 A, red dot), the 388 cm^{-1} mode red shifts, consistent with the sign on the measured Stark coefficient. In the positive contrast images presented, this manifests as a dip in the TERS map. Alternatively, the 1568 cm^{-1} exhibits an overall blue shift, and 5 cm^{-1} variation thereof, directly mapping out the N site. Consistent with the local field map presented in Figure 4.7, contributions to the TERS signal due to Cu atoms are not apparent. Simulations into the effects of constant current v. constant height were performed. The small magnitude of the tip oscillation under constant current scanning (~10 pm) was found to be insignificant when compared to the total charge. This straightforward model captures the general features and concept of TERS ν-shift mapping through the apex bound reporter.

4.8 TERS intensities

The ν-shift maps uniquely identify the position of the N sites in the Cu_2N lattice. The intensity images may be assigned in a similar fashion. Interestingly, the TERS intensity maps out the 4-fold hollow site with high fidelity. Similar to the ν-shift measurements, the TERS

intensity contrast is generated on and off the N and 4-fold hollow sites. The general intensity trend is as follows: 4-FH > Cu > N. The weak TERS activity on N sites suggests that these atoms act as spectators in the Raman optical process.

In Figure 4.8, the STM topography is compared to the TERS intensity maps for two different set points. Line profiles extracted at corresponding points in each image exemplify the TERS intensity – tip height correlation. At 1 nA and +15 mV, the TERS intensity mimics the topography (Figure 4.8 A 1-3). When the tip is engaged further by decreasing the bias (set point of 1 nA, -20 mV, Figure 4.8 B 1-2), the same is true along the Cu cut. Along the N-Cu-N cut, similar, yet phase shifted profiles are observed. Note, the set point evolution observed in the topography is not mirrored in the TERS intensity maps, which aside from a fractional decrease in count rate appear identical. The linear correspondence between the tip height and the intensity is consistent with the retraction dependence curves presented in Figure 4.3. That is, the small amplitude height dither observed in the CC topography traces over a narrow window in the retraction dependence over which the intensity is essentially linear.

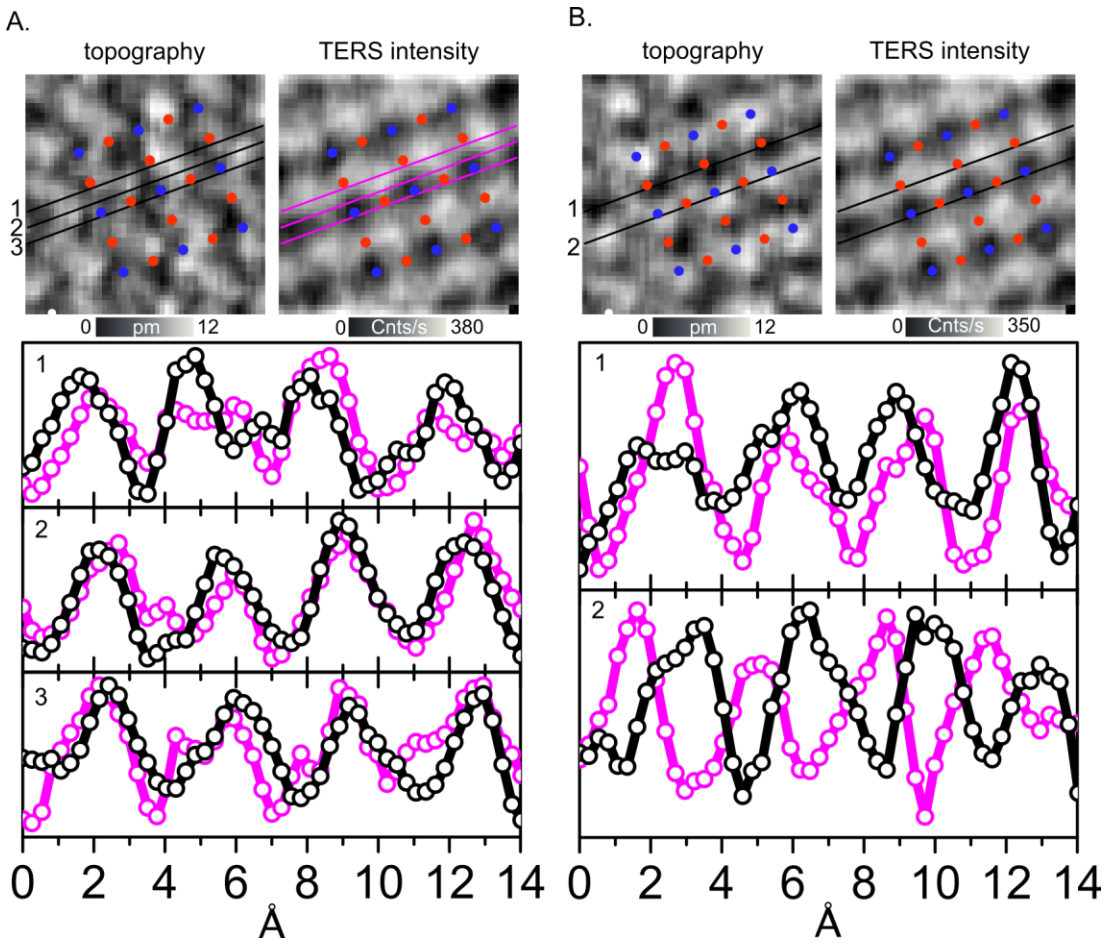

Figure 4.8 STM topography - TERS intensity correlation. Topography (left) and intensity maps (right) are shown in (A) and (B) for 1 nA +15 mV, and 1 nA -20 mV set points, respectively. Line profiles are shown and were taken where indicated.

The linear correspondence between the tip height and the TERS intensity preclude the use of electromagnetic arguments, that is, modulation of the field due to gap variation, to justify the response. If purely electromagnetic in origin, the TERS intensity would vary as g_0^{-4} (field-driven Raman) and would also be anti-correlated with the tip height. This suggest that in the narrow gaps utilized to sustain TERS, photo-current driven Raman is operative. Note, the phase-shifted response observed when the bias is tuned to +15 mV is due to evolution of the topography. STM tracks the DC tunneling current, which is, in general, a complex function of sample bias. Moreover, the seemingly bias independent intensity maps suggest that the

DC and AC (Raman) components of the tunneling current are involved in separate terminal densities. The 634 nm excitation provides 1.95 eV of energy, which is sufficient to excite photo-electrons well out of the Fermi energy range, where the local density of states is complex. In this regard, it is not surprising that the TERS intensity maps closely resemble the high bias topography presented in Figure 4.2. The lack of appreciable variation in the TERS maps among the various vibrational modes is also consistent with this model; the excess photon energy provided by most shifted modes, ~1600 cm^{-1}, is small compared to that of the incident light, and evidently narrower than the photo-tunneling resonance accessed here.

The retraction curves presented in Figure 4.3 are further evidence for photo-current driven Raman. The 2 Å decay length(s) observed for the TERS intensities coincides with the de Broglie wavelength of a Fermi electron, effectively limiting the efficacy of TERS imaging to the range where the junction is (photo)conductive. In this regard, the intensity is well suited to behave as a single molecule ammeter, now operating at optical frequencies.

4.9 Conclusions

The CoTPP terminated tip utilized here ultimately enables atomic resolution in TERS, which was demonstrated on a Cu_2N monolayer supported by Cu(100). This arguably inefficient plasmonic heterojunction, utilized in conjunction with non-electronically resonant Raman, provided sufficient enhancement to carry out a wide range of TERS experiments. While the size extent of the molecule itself implies spatial averaging, the surface features are laterally resolved with 1.5 Å precision, which was evident in both the Stark shift and TERS intensity mapping. The former was shown to map out the static charge distribution of the ionic surface with high fidelity, relayed into the far-field through multiple normal modes of the CoTPP.

The TERS spectra were shown to be consistent with reorganization of the molecule upon tip adsorption, which was explored by considering the Raman spectrum of a SM through localized excitation. These results highlight the origin of atomic resolution as motion of the distal vibrational modes along the tip axis translated into polarization of the central cobalt atom on the porphyrin. This finding serves as a fundamental design consideration for exercising ultrahigh resolution TERS with functionalized tips and provides the essential framework for extending these studies into the ambient, where chemistry abounds.

Interestingly, the intensity maps, which directly track the junction optical conductance, are similar to the STM topographs acquired with similar energy electrons. This was highlighted by the TERS intensity maps and retraction curves, which require ~ 1-5 Å separation between the tip and sample. Overall, the explored (photo)physics of the surface-molecule interaction clearly demonstrate the essential role of photoelectrons in the TERS process.

4.10 Appendix

4.10.1 Stark tuning rates

Mode (cm^{-1})	$d\nu/dV$ ($cm^{-1}V^{-1}$)	
	N site	Cu Site
390	*-0.37 ± 0.03*	*-0.38 ± 0.02*
986	*0.17 ± 0.12*	*0.13 ± 0.02*
1550	*0.40 ± 0.17*	*0.70 ± 0.10*
1569	*0.67 ± 0.12*	*0.50 ± 0.03*

Table 4.1 Experimental slopes extracted from plots of frequency vs. sample bias recorded at N and Cu positions.

4.10.2 Localized Raman scattering

The rate of non-resonant Raman scattering may be cast in terms of Fermi's golden rule:

$$\frac{1}{\tau} = \frac{2\pi}{\hbar}\left|\left\langle E_{s,\rho}\chi_{g,v'}\right|\left(\alpha_0 + \frac{\partial\alpha}{\partial q_n}q_n\right)\left|\chi_{g,v}E_{i,\sigma}\right\rangle\right|^2 \delta\left[E_{i,s} - E_{v',v} - i\gamma\right]. \qquad (4.10.1)$$

The first term leads Rayleigh scattering in the far field and to AC stark shift in the near field, given by enhanced local fields:

$$\left\langle E_{s,\rho}\chi_g\middle|\alpha_0\middle|\chi_g E_{i,\sigma}\right\rangle\delta_{i,s} = E_{L,i}\langle\alpha_0\rangle_{\rho\sigma}E_{L,i} + E_{L,s}\langle\alpha_0\rangle_{\rho\sigma}E_{L,s}. \qquad (4.10.2)$$

Raman scattering is due to the second term, but now in terms of the real space N atomic positions:

$$\frac{\partial \alpha}{\partial q_n} q_n = \sum_{i=1,N} \frac{\partial \alpha}{\partial r_{i;n}} r_{i;n} \tag{4.10.3}$$

For a particular mode *n*, the matrix element of interest is:

$$\sum_{i=1,N} \left\langle E_{s,\rho} \chi_{g,v'} \left| \frac{\partial \alpha}{\partial r_i} r_i \right| \chi_{g,v} E_{i,\sigma} \right\rangle \tag{4.10.4}$$

Assuming Born-Oppenheimer separation of the vibronic wavefunctions,

$$= \sum_{i=1,N} \langle \frac{\partial \alpha}{\partial r_i} \rangle_{g,\rho\sigma} \langle E_L(r) \psi_{v'}(r) | r_i | \psi_{v=0}(r) E_L(r) \rangle \tag{4.10.5}$$

the scalar local field is isolated in the spatial integral. Then using the ladder operator,

$$= \sum_{i=1,N} \langle \frac{\partial \alpha}{\partial r_i} \rangle_{g,\rho\sigma} \left\langle E_L(r) \psi_{v'}(r) \left| \frac{\delta_i}{\sqrt{2}} (a + a^+) \right| \psi_{v=0}(r) E_L(r) \right\rangle \tag{4.10.6}$$

$$= \sum_{i=1,N} \langle \frac{\partial \alpha}{\partial r_i} \rangle_{g,\rho\sigma} \langle \frac{\delta_i}{\sqrt{2}} P_{v=1}(r) I_L(r) \rangle \tag{4.10.7}$$

Where,

$$\delta_n^2 = \frac{\hbar}{m\omega_n}, \tag{4.10.8}$$

is the amplitude of motion and

$$P_{v=1}(r) = \psi_1^*(r) \psi_1(r), \tag{4.10.9}$$

is the ν=1 vibrational probability distribution. The signal can be seen in (4.10.7) to be determined by the overlap of vibrational distribution and the scalar local field. Assuming a Gaussian for the latter:

$$= \sum_{i=1,N} \langle \frac{\partial \alpha}{\partial r_i} \rangle_{g,\rho\sigma} \int \frac{\delta_i}{\sqrt{2}} \frac{1}{\sqrt{\pi}\delta_i} \left(\frac{r - r_i}{\delta_i^2} \right)^2 e^{-\left(\frac{r-r_i}{\delta_i}\right)^2} e^{-\left(\frac{r-r_T}{\Delta}\right)^2} dr \qquad (4.10.10)$$

Dropping the slowly varying quadratic term under the integral, in effect retaining the ν=0 vibrational probability density, (4.10.10) reduces to the Gaussian overlap integral:

$$= \sum_{i=1,N} \langle \frac{\partial \alpha}{\partial r_i} \rangle_{g,\rho\sigma} \frac{1}{\sqrt{2\pi}} \int e^{-\left(\frac{r-r_i}{\delta_i}\right)^2} e^{-\left(\frac{r-r_T}{\Delta}\right)^2} dr \qquad (4.10.11)$$

Under the assumption $\delta_i \ll \Delta$,

$$\sum_{i=1,N} \langle \frac{\partial \alpha}{\partial r_i} \rangle_{g,\rho\sigma} \frac{\delta_i}{\sqrt{2}} e^{-\left(\frac{r_i-r_T}{\Delta}\right)^2}. \qquad (4.10.12)$$

Noting that

$$\frac{\partial \alpha}{\partial q_n} = \sum_i \frac{\partial \alpha}{\partial r_i}, \qquad (4.10.13)$$

the final form used in the evaluations is reached:

$$\left| \langle \frac{\partial \alpha}{\partial q_n} \rangle_{g,\rho\sigma} \sum_{i=1,N} \frac{\delta_i}{\sqrt{2}} e^{-\left(\frac{r_i-r_T}{\Delta}\right)^2} \right|^2. \qquad (4.10.14)$$

5 Femtosecond apparatus for surface enhanced spectroscopy

5.1 Introduction

Parametric four-wave mixing (4WM) processes represent one of the more general families of ultrafast time-resolved nonlinear optical spectroscopies[14], which acquire their full capability when executed with three incident pulses in three colors that can be independently controlled[132]. Beyond flexibility, 4WM in three colors achieves ultimate sensitivity by allowing background free detection. In this limit, detectivity is determined by the noise equivalent count rate of signal photons, which, for spontaneous scattering on a single center, is given quite generally by the product

$$counts = (I/\hbar\omega)\sigma\eta f\delta t \qquad (5.1.1)$$

of incident local intensity, I, scattering cross section, σ, collection efficiency, η, and fill factor, $ff = f\delta t$, product of pulse width, δt, and laser repetition rate, f. There are fundamental limitations on the attainable count rate. To remain in the weak-field limit of perturbative parametric mixing processes, the Keldysh criterion[97] limits the maximum tolerable local field intensity to $I_{L,max} \sim 10^{13}$ W/cm^2 ($E_{L,max} \sim 1$ V/nm). This limit is easily attained in tightly focused fs laser pulses (10 nJ, 100 fs pulse, focused to a spot of 1 μm^2). σ is a material property, therefore under optimized collection conditions, for ultrafast measurements with time resolution set by δt, it is necessary to operate at as high a repetition rate as allowed by the recovery time of the system under interrogation. For molecular matter, photon anti-bunching sets the fundamental limit of maximum count rates to ~ 25 MHz[133-134]. This sets the lower limit for f, since in general the scattering probability cannot be saturated. Thus, optimal source requirements for a large number of applications is fairly narrowly defined:

three independent colors at $f \geq 100$ MHz, δt = 100 fs, and average power of mW. Here, an efficient and compact system based on photonic crystal fibers (PCF) that meet these requirements is presented and demonstrated through three-color time-resolved coherent anti-Stokes Raman scattering (tr-CARS) measurements.

Various approaches have been previously used for non-resonant, background-free CARS spectroscopy and microscopy[135-159]. These include second harmonic based[158] supercontinuum (SC) based techniques[138-150, 160], or reliance on a single broadband pulse[151-157], along with approaches requiring kHz amplifiers[158-159]. In Ref. 158, a multiplexed three-color three-pulse tr-CARS scheme was developed to acquire non-resonant background-free spectra with high spectral resolution and relatively broad spectral range (~ 900 cm^{-1}). However, this approach requires high intensity laser systems, including a kHz amplifier and optical parametric amplifier. The more efficient approach to achieve a large Raman frequency range (> 2000 cm^{-1}) from an unamplified and high repetition-rate source (> 100 MHz) is to use SC generated in nonlinear fibers[138-150, 160]. This has been implemented in frequency domain two-color CARS, with degenerate pump and probe excitations driven by the narrowband source and Stokes induced by the continuum[138]. Microscopy with two-pulse three-color CARS, in which two different frequency components of the continuum act as pump and Stokes and the narrowband pulse acts as probe[160], has also been effectively implemented to obtain images tagged by vibrational dephasing times[139]. This approach takes advantage of the time-delayed probe to separate the resonant signal from the nonresonant background by virtue of the contrast in coherence times of the nonresonant background (< 10 fs) and vibrational resonances (0.5 ps-10 ps). Approaches based on amplified laser systems to pump multiple optical parametric amplifiers to generate multiple fs pulses are

limited in repetition rate, typically to < 10 MHz. In contrast, oscillator pumped fiber-based setups have the advantage of higher repetition rate (> 100 MHz) at significantly reduced cost and complexity, signal-to-noise ratio improvement by higher data acquisition rates, and peak powers reduced by the fill factor to prevent sample damage. Despite these promising advantages, reports of *t*-domain 4WM via SC generation in fibers have been limited to impulsive application of the pump and dump (Stokes) pulses. Here, we demonstrate three-color, three-pulse, tr-CARS based on SC generation in a commercially available PCF and subsequent slicing of the spectrum with filters to generate the desired pump, Stokes, and probe pulses with independently controllable time-frequency profiles. The demonstration suggests that the approach is well suited to address the challenges of single-molecule ultrafast coherent spectroscopy[54, 64, 161].

5.2 Experiment

5.2.1 Methods

A detailed schematic of the three-color, three-pulse tr-CARS setup is shown Figure 5.1. A mode-locked Ti:sapph laser (Coherent, Inc., MIRA 900) operating at 798 nm (average power = 700 mW, f = 76 MHz, δt = 40 fs) is used to pump a 12 cm long, polarization maintaining PCF (NKT Photonics NL-PM-750). The fiber is mounted in a protective module (FemtoWHITE 800),and housed in a commercial intensity control/fiber-coupling unit (Newport Wavelength Extender (WE) SCG-02). The WE splits the pump beam using a polarizing cube (PCBS) into two, and provides variable attenuators consisting of half waveplates and Glan-laser polarizers to control the intensities in the two arms. The first arm passes through a Faraday isolator (FI) and is used to pump the PCF with 50% coupling efficiency. The second arm, which consists of the remaining Ti:sapph output, is utilized as

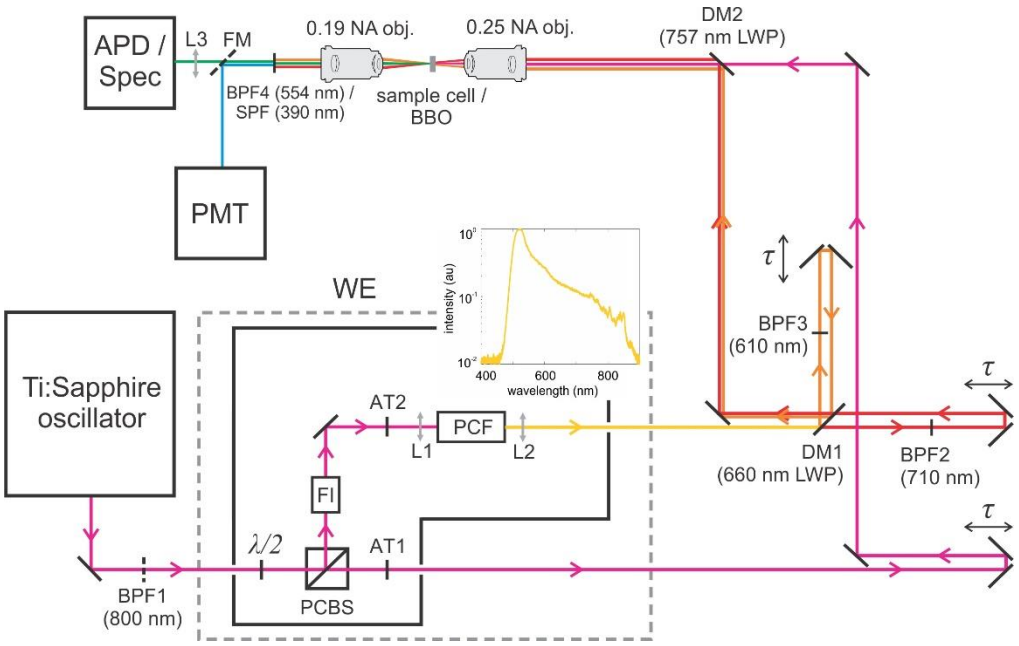

Figure 5.1 Experimental apparatus for three-color three-pulse CARS (λ/2 – half waveplate, PCBS – polarizing cube beamsplitter, FI – Faraday isolator, AT1, AT2 – attenuator assemblies consisting of half waveplates and Glan-laser polarizers, L1, L2 – aspheric lenses for focusing and collimation, PCF – photonic crystal fiber, WE – wavelength extender, DM1, DM2 – 660 nm and 757 nm long wave pass dichroic beamsplitters, BPF1, BPF2, BPF3, BPF4 – bandpass filters centered at 800 nm, 710 nm, 610 nm, and 554 nm respectively, SPF – 390 nm short wave pass filter, APD – avalanche photodiode, Spec – spectrograph, PMT – photomultiplier tube. Inset shows the SC spectrum on log scale.

either the reference pulse in cross-correlation measurements or as the Stokes pulse in the CARS measurements (see below). The spectrally broad output of the PCF (inset of Figure 5.1). is further split into red and blue arms using a 660 nm long wave pass dichroic mirror (Semrock FF660-Di02), followed by bandpass filters in each arm to select the desired colors. In the present, 10 nm FWHM bandpass filters centered at 610 nm (Thorlabs FB610-10) and 710 nm (Thorlabs FB610-10) are used in the blue and red arms, respectively. The sliced pulses are then recombined along with the leftover fundamental in a collinear geometry using a 757 nm long wave pass dichroic mirror (Semrock FF757-Di01). Separate delay lines

and attenuators are used to introduce relative delay between the pulses and for intensity control.

The collinear CARS measurements are carried out on liquid trans-1,2-bis-(4-pyridyl) ethylene (BPE) dissolved in methanol, or in pure styrene, contained in 1 mm quartz cuvettes. An achromatic 0.25 NA objective lens is used to focus the three beams to a spot size of ~ 10 μm. In our tr-CARS configuration, the sliced pulses at 708 nm and 612 nm serve as pump (Pu) and probe (Pr), while the leftover fundamental at 798 nm serves as the Stokes (St), to generate the anti-Stokes signal $\omega_{Pu} - \omega_{St} + \omega_{Pr} = \omega_{AS}$ centered at 557 nm. The transmitted excitation pulses, along with the CARS signal, are collimated and spectrally filtered (Semrock FF01-554/23-25) to isolate the anti-Stokes signal. The signal is collected using an avalanche photodiode (APD Excelitas SPCM-AQRH-16-FC), and recorded using a dual-channel photon counter (Stanford Research Systems SR400). The pulses are characterized through sum-frequency generation (SFG) cross-correlation using a 1 mm BBO crystal placed in the sample position. The three-pulse instrument response is characterized through third-order cross-correlation frequency-resolved optical gating (XFROG)[162]by replacing the sample with pure carbon disulfide (CS_2) and using a spectrograph (Andor iDus 401/Shamrock 303i) in place of the APD. The pulses are not precompensated for group-delay dispersion (GDD) of the objective lens, which is estimated to be 2200 fs^2 at 612 nm (4 cm, fused silica).

5.2.2 Characterization of the sliced PCF pulses

SC generation in the NL-PM-750 PCF, and applications therein, are available in prior reports[163-165]. The PCF displays anomalous dispersion with two zero crossings at 750 nm and 1260 nm. The output characteristics of the highly nonlinear fiber depend on the intensity,

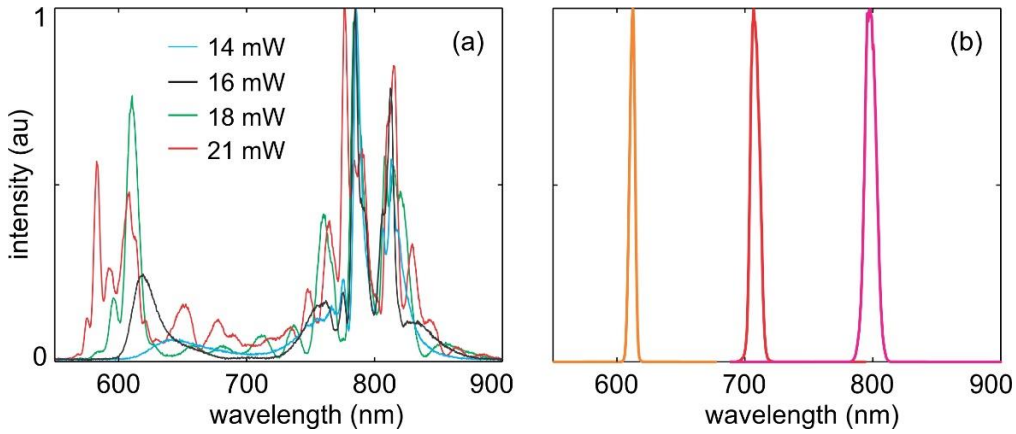

Figure 5.2 (a) SC spectra at different pump powers, (b) normalized spectra of the probe (612 nm), pump (708 nm), and Stokes (798 nm) pulses sliced from the SC spectrum given by the green trace in (a).

wavelength, and bandwidth of the pump beam. When directly pumped with the 40 fs (25 nm FWHM) Ti:Sapph laser at 0.5 W average power, a fairly flat SC is generated across the wavelength range 400-900 nm, as illustrated in the inset of Figure 5.1. Note that the red edge of the displayed spectrum is limited by the spectral response of our spectrometer, otherwise it stretches out to 1600 nm. Under this pumping condition, the sliced pulses at 708 nm and 612 nm stretch out to ~ 1 ps. It is in principle possible to compress these output pulses. Instead, we generate nearly transform-limited output pulses directly by limiting both bandwidth and intensity of the pump laser to counter-balance the interplay of self-phase modulation and dispersion. The generation of transform-limited SC components at these low intensities is thought to principally arise from soliton fission[142, 166]. With the bandwidth of the pump laser limited to 10 nm using a bandpass filter (Figure 5.1, BPF1), by adjusting the pump intensity, near transform-limited 100 fs pulses can be extracted from the PCF. Under these conditions, the SC is strongly colored, with spectral structure that tunes as a function of pump power[142, 166]. This is illustrated in Figure 5.2 (a). For the set of spectral slices pre-specified by the bandpass filters to $\lambda(\Delta\lambda)$= 612(5) nm, 708(8) nm, and 798(10) nm, the

shortest pulses are obtained when the PCF is pumped at 36 mW (total SC output of 18 mW). The strongly modulated SC spectrum obtained under this pumping condition is the green trace in Figure 5.2 (a), and the spectra of the filtered slices are shown in Figure 5.2 (b). The filter functions inscribe the bands in the SC spectrum, to slice out sections of stationary phase, albeit with different intensities. The extracted powers at 612 nm and at 708 nm are 110 μW and 25 μW, respectively. To characterize the sliced pulses, we carry out cross-correlation and XFROG measurements, which are summarized Figure 5.3 and Figure 5.4.

Using the filtered 798 nm (94 fs) pulse as reference, the cross-correlations of the pump (708 nm) and probe (612 nm) pulses yield widths of FWHM = 150 fs and 153 fs, respectively (Figure 5.3). Assuming Gaussian profiles, the cross correlation widths $\delta t_{i,j} = [\delta t_i^2 + \delta t_j^2]^{1/2}$ imply pulse widths of FWHM = 120 fs for both pump and probe slices. This is to be compared with their respective bandwidth equivalent transform limit of 92 fs and 110 fs.

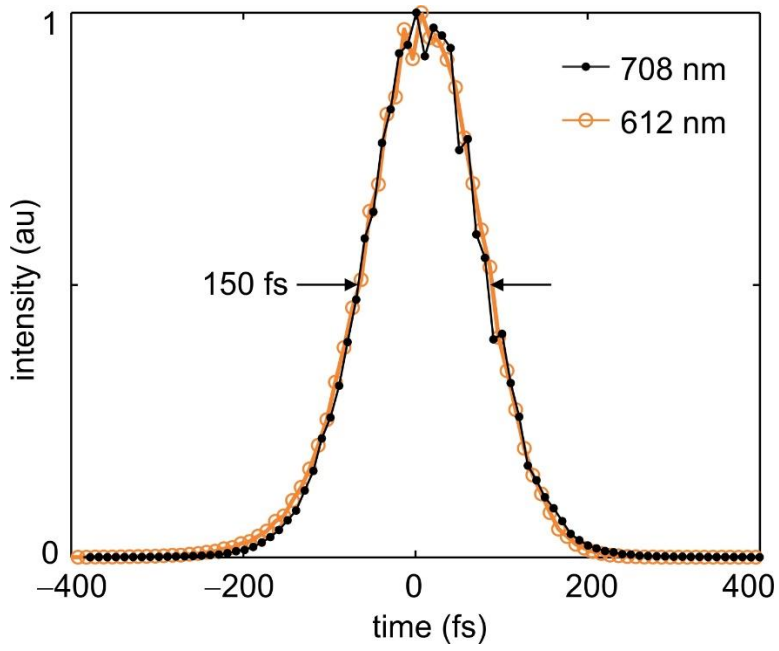

Figure 5.3 Cross-correlations of pump (black dotted) and probe (open orange circles) pulses.

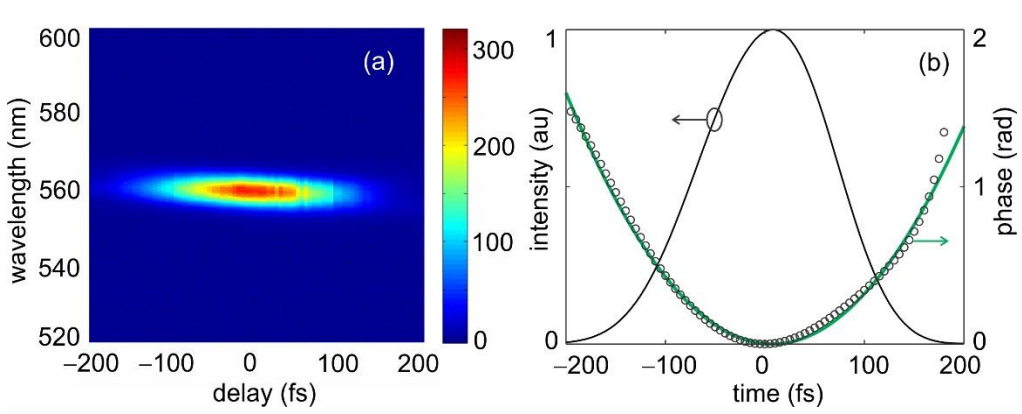

Figure 5.4 (a) Measured XFROG trace, (b) retrieved temporal (black solid) and phase profiles (open circles), together with a quadratic fit (green solid).

The residual pulse broadening can be entirely accounted by GDD in the objective lens. Thus, for a Gaussian pulse traveling a distance z in a dispersive medium: $\tau/\tau_0 = 1+(z/L_D)^2$, where $L_D = \tau_0^2/\beta_2$ is the dispersive length and β_2 is the second-order dispersion coefficient[167]. The observed broadening suggests that the pulses are subject to GDD $\equiv \beta_2 z = \tau_0\sqrt{\tau^2-\tau_0^2} \sim 2400$ fs^2 and ~ 2000 fs^2 at 612 nm and 708 nm, which is close to the value of GDD= 2200 fs^2, and 1800 fs^2 that we estimate for the objective lens at the same wavelengths (z = 4 cm, fused silica). In effect, the sliced pulses out of the PCF appear to be transform-limited, with pulse widths limited by the pump laser.

The third-order XFROG measurement, which is shown in Figure 5.4, captures the instrument response function for 4WM measurements and confirms that the residual chirp in the pulses is linear (quadratic phase). The measurement carried out in liquid CS_2 consists of recording the anti-Stokes spectrum as a function of delay of the 610 nm probe pulse, and with coincident pump and Stokes pulses that are fixed in time. In effect, this is a spectrally-resolved tr-CARS measurement in the absence of vibrational resonances; therefore, it measures the instantaneous response of the system. The XFROG trace is shown in Figure 5.4

(a), and the retrieved temporal intensity (black solid) and phase (open circles) profiles using the Femtosoft XFROG software (version 3.2.4), are shown in (b). The temporal phase is predominantly quadratic, as shown by the fit (in green). The fit yields *GDD*= 4300 fs^2, in excellent agreement with the additive *GDD* values (2400 fs^2 + 2000 fs^2) extracted above from the cross-correlation measurements. Thus, compressible, near transform-limited 100 fs pulses, in three colors, with an average power of ~ 100 μW in the sliced pulses are obtained at 76 MHz repetition rate.

5.3 CARS measurements and discussion

The time-frequency profiles of the filtered pulses were designed to interrogate quantum beats among ubiquitous, aromatic C=C stretching modes of organic molecules, which occur near 1600 cm^{-1}. These are the prominent lines seen in the Raman spectra of BPE and styrene, which are shown in Figure 5.5 along with the measured tr-CARS time traces. Note that both Raman and CARS are determined by the third order polarization, $P^{(3)}$. The first measures the imaginary part, $\mathrm{Im}[P^{(3)}]$, in the frequency domain, while the latter measures $|P^{(3)}|^2$ in the time domain[14]. As such, for an ensemble measurement with homogeneously broadened lines, the Raman spectrum contains all of the information necessary to predict the tr-CARS response. With the 708 nm pulse acting as pump and the 798 nm pulse acting as Stokes, the polarization that can be prepared is delimited by the Raman window given by the spectral convolution:

$$W_R(\omega) = \int I_{Pu}(\omega') I_{St}(\omega' - \omega) d\omega' \qquad (5.3.1)$$

The window, which is centered at $\omega_{Pu} - \omega_{St}$ = 1593 cm^{-1} and has a FWHM of 224 cm^{-1}, is superimposed on the Raman spectra (insets in Figure 5.5). The tr-CARS traces are retrieved from the inverse Fourier transform of the window-weighted Raman spectrum:

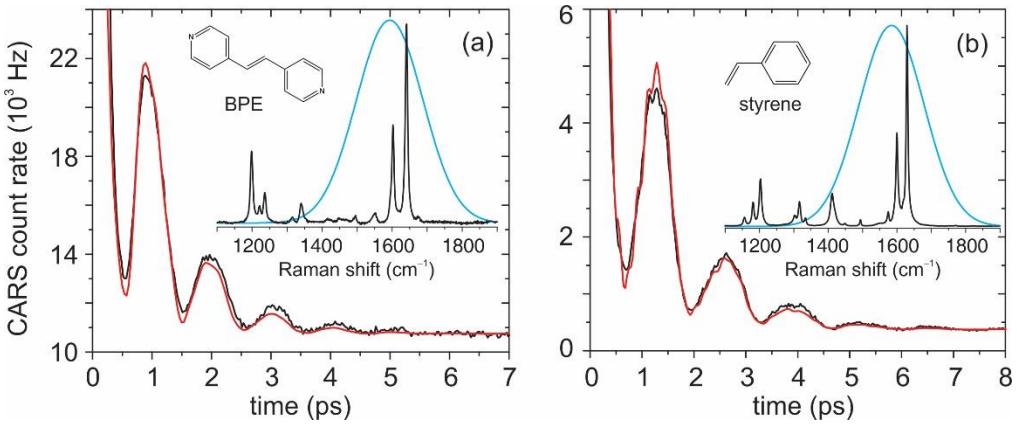

Figure 5.5 Measured (black) and simulated (red) tr-CARS traces for (a) BPE and (b) styrene. The simulations are based on the windowed inverse Fourier transform of the Raman spectra (Eq. (3) of text). The Raman spectra and window function (blue) are shown in the insets.

$$S_{AS}(t) = \left| \int W_R(\omega)\, I_R(\omega) e^{i\omega t} d\omega \right|^2 . \qquad (5.3.2)$$

The comparison of the observed tr-CARS signal and its simulation for BPE and styrene are presented in Figure 5.5 (a,b). Beside the main beats, which occur with a period of 1 ps and 1.3 ps in BPE and styrene, respectively, the styrene time profile in Figure 5.5(b) exhibits a small-amplitude higher-frequency modulation due to the weaker vibrations that appear in the Raman window. Formally, it is the third-order polarization that is detected through the anti-Stokes bandpass filter (BPF4 in Figure 5.1), and the convolution with probe pulse can in principle diminish the depth of modulation in the time trace[117]. Simulations of the effect of probe convolution show that this is a minor effect, consistent with the instrumental response captured by the third order XFROG in Figure 5.4.

A principle advantage of the three-color 4WM was advanced as a background-free detection method, yet the time trace of the signal in Figure 5.5 (a) clearly rides over a background of 10^4 counts, comparable to the signal. This we have verified to arise from a two-photon induced fluorescence in BPE, which coincides with the anti-Stokes window. The baseline of 400 counts in the case of styrene Figure 5.5 (b) is due to scattered stray light, which sets the noise equivalent count rate in the setup. Otherwise, the dynamic range of the signal, $S:N \sim 100$, agrees with the shot noise, $N/N^{1/2}$, where $N \sim 10^4$ is the signal photon count rate. The effect of source noise, due to pulse-to-pulse fluctuations of the nonlinear SC generation in the PCF is not apparent.

5.4 Conclusion

Based on fundamental considerations, namely Eq. (5.1.1) we have argued that ultimate limits in detectivity of ultrafast time-resolved processes in molecular matter is reached through three-color fs lasers operating near or above 100 MHz. We have shown that this can be accomplished in a compact setup, through the use of a PCF, and we have proven the concept by implementing it to carry out tr-CARS measurements. The key finding is that nearly transform-limited 100-fs coherent multicolor pulses can be extracted from a single PCF by controlling the bandwidth and intensity of the pump pulse. The approach is amenable to a variety of adaptations and improvements. The repetition rate is only limited by the pump source, and, given the low requirement on pump power, the repetition rate of the system can be readily increased to 10 GHz using demonstrated passively mode-locked Ti:sapph oscillator technology[168]. And while we demonstrated the operation with prescribed fixed colors and pulse widths, it should be clear that through the use of variable bandpass filters,

the entire PCF spectrum (400-1600 nm) is accessible to generate multiple compressible pulses of different color. To this end, the combination of the PCF and a pulse shaper[169] would greatly add to flexibility and compactness. The development we presented is part of a program aimed at preparing and manipulating quantum coherences on individual molecules.

References

1. Nie, S.; Emory, S. R., Probing Single Molecules and Single Nanoparticles by Surface-Enhanced Raman Scattering. *Science* **1997**, *275*, 1102-1106.
2. Kneipp, K.; Wang, Y.; Kneipp, H.; Perelman, L. T.; Itzkan, I.; Dasari, R. R.; Feld, M. S., Single Molecule Detection Using Surface-Enhanced Raman Scattering (Sers). *Phys. Rev. Lett.* **1997**, *78*, 1667-1670.
3. Paesler, M. A.; Moyer, P. J., *Near-Field Optics : Theory, Instrumentation, and Applications*; Wiley: New York, 1996, p xii, 355 p.
4. Kneipp, K.; Wang, Y.; Kneipp, H.; Itzkan, I.; Dasari, R. R.; Feld, M. S., Population Pumping of Excited Vibrational States by Spontaneous Surface-Enhanced Raman Scattering. *Phys. Rev. Lett.* **1996**, *76*, 2444-2447.
5. Jeanmaire, D. L.; Van Duyne, R. P., Surface Raman Spectroelectrochemistry: Part I. Heterocyclic, Aromatic, and Aliphatic Amines Adsorbed on the Anodized Silver Electrode. *Journal of Electroanalytical Chemistry and Interfacial Electrochemistry* **1977**, *84*, 1-20.
6. Fleischmann, M.; Hendra, P. J.; McQuillan, A. J., Raman Spectra of Pyridine Adsorbed at a Silver Electrode. *Chem. Phys. Lett.* **1974**, *26*, 163-166.
7. Novotny, L.; van Hulst, N., Antennas for Light. *Nat. Photon.* **2011**, *5*, 83-90.
8. Arroyo, J. O.; Kukura, P., Non-Fluorescent Schemes for Single-Molecule Detection, Imaging and Spectroscopy. *Nat Photon* **2016**, *10*, 11-17.
9. Dieringer, J. A.; Lettan, R. B.; Scheidt, K. A.; Van Duyne, R. P., A Frequency Domain Existence Proof of Single-Molecule Surface-Enhanced Raman Spectroscopy. *J. Am. Chem. Soc.* **2007**, *129*, 16249-16256.
10. Michaels, A. M.; Nirmal, M.; Brus, L. E., Surface Enhanced Raman Spectroscopy of Individual Rhodamine 6g Molecules on Large Ag Nanocrystals. *J. Am. Chem. Soc.* **1999**, *121*, 9932-9939.
11. Benz, F., et al., Single-Molecule Optomechanics in “Picocavities”. *Science* **2016**, *354*, 726.
12. Albrecht, M. G.; Creighton, J. A., Anomalously Intense Raman Spectra of Pyridine at a Silver Electrode. *J. Am. Chem. Soc.* **1977**, *99*, 5215-5217.
13. Blackie, E. J.; Ru, E. C. L.; Etchegoin, P. G., Single-Molecule Surface-Enhanced Raman Spectroscopy of Nonresonant Molecules. *J. Am. Chem. Soc.* **2009**, 14466-1472.
14. Mukamel, S., *Principles of Nonlinear Optical Spectroscopy*: Oxford University Press, 1995.
15. Kneipp, K.; Moskovits, M.; Kneipp, H., *Surface Enhanced Raman Scattering, Physics and Applications*; Springer: Berlin, 2006; Vol. 103.
16. Le Ru, E. C.; Etchegoin, P. G., Rigorous Justification of the |E|4 Enhancement Factor in Surface Enhanced Raman Spectroscopy. *Chem. Phys. Lett.* **2006**, *423*, 63-66.
17. Nordlander, P.; Oubre, C.; Prodan, E.; Li, K.; Stockman, M. I., Plasmon Hybridization in Nanoparticle Dimers. *Nano Lett.* **2004**, *4*, 899-903.
18. Aćimović, S. S.; Kreuzer, M. P.; González, M. U.; Quidant, R., Plasmon near-Field Coupling in Metal Dimers as a Step toward Single-Molecule Sensing. *ACS Nano* **2009**, *3*, 1231-1237.

19. Talley, C. E.; Jackson, J. B.; Oubre, C.; Grady, N. K.; Hollars, C. W.; Lane, S. M.; Huser, T. R.; Nordlander, P.; Halas, N. J., Surface-Enhanced Raman Scattering from Individual Au Nanoparticles and Nanoparticle Dimer Substrates. *Nano Lett.* **2005**, *5*, 1569-1574.
20. Hao, E.; Schatz, G. C., Electromagnetic Fields around Silver Nanoparticles and Dimers. *J. Chem. Phys.* **2003**, *120*, 357-366.
21. Atay, T.; Song, J.-H.; Nurmikko, A. V., Strongly Interacting Plasmon Nanoparticle Pairs: From Dipole−Dipole Interaction to Conductively Coupled Regime. *Nano Lett.* **2004**, *4*, 1627-1631.
22. Schatz, G. C.; Van Duyne, R. P., Electromagnetic Mechanism of Surface-Enhanced Spectroscopy. In *Handbook of Vibrational Spectroscopy*, John Wiley & Sons, Ltd: 2006.
23. Moskovits, M., Surface-Enhanced Spectroscopy. *Reviews of Modern Physics* **1985**, *57*, 783-826.
24. Metiu, H.; Das, P., The Electromagnetic Theory of Surface Enhanced Spectroscopy. *Annu. Rev. Phys. Chem.* **1984**, *35*, 507-536.
25. Banik, M.; El-Khoury, P. Z.; Nag, A.; Rodriguez-Perez, A.; Guarrottxena, N.; Bazan, G. C.; Apkarian, V. A., Surface-Enhanced Raman Trajectories on a Nano-Dumbbell: Transition from Field to Charge Transfer Plasmons as the Spheres Fuse. *ACS Nano* **2012**, *6*, 10343-10354.
26. Gersten, J.; Nitzan, A., Electromagnetic Theory of Enhanced Raman Scattering by Molecules Adsorbed on Rough Surfaces. *J. Chem. Phys.* **1980**, *73*, 3023-3037.
27. Kerker, M., Electromagnetic Model for Surface-Enhanced Raman Scattering (Sers) on Metal Colloids. *Acc. Chem. Res.* **1984**, *17*, 271-277.
28. Aravind, P. K.; Metiu, H., The Enhancement of Raman and Fluorescent Intensity by Small Surface Roughness. Changes in Dipole Emission. *Chem. Phys. Lett.* **1980**, *74*, 301-305.
29. Weitz, D. A.; Garoff, S.; Gramila, T. J., Excitation Spectra of Surface-Enhanced Raman Scattering on Silver-Island Films. *Opt. Lett.* **1982**, *7*, 168-170.
30. Wokaun, A.; Gordon, J. P.; Liao, P. F., Radiation Damping in Surface-Enhanced Raman Scattering. *Phys. Rev. Lett.* **1982**, *48*, 957-960.
31. Pettinger, B., Light Scattering by Adsorbates at Ag Particles: Quantum-Mechanical Approach for Energy Transfer Induced Interfacial Optical Processes Involving Surface Plasmons, Multipoles, and Electron-Hole Pairs. *J. Chem. Phys.* **1986**, *85*, 7442-7451.
32. Bernath, P. F., *Spectra of Atoms and Molecules*; Oxford University Press, 2005.
33. El-Khoury, P. Z., et al., The Information Content in Single-Molecule Raman Nanoscopy. *Advances in Physics: X* **2016**, *1*, 35-54.
34. Tallarida, N.; Rios, L.; Apkarian, V. A.; Lee, J., Isomerization of One Molecule Observed through Tip-Enhanced Raman Spectroscopy. *Nano Lett.* **2015**, *15*, 6386-94.
35. Chulhai, D. V.; Chen, X.; Jensen, L., Simulating Ensemble-Averaged Surface-Enhanced Raman Scattering. *The Journal of Physical Chemistry C* **2016**, *120*, 20833-20842.
36. Chulhai, D. V.; Jensen, L., Determining Molecular Orientation with Surface-Enhanced Raman Scattering Using Inhomogenous Electric Fields. *The Journal of Physical Chemistry C* **2013**, *117*, 19622-19631.
37. Shegai, T. O.; Haran, G., Probing the Raman Scattering Tensors of Individual Molecules. *The Journal of Physical Chemistry B* **2006**, *110*, 2459-2461.
38. Ayars, E. J.; Hallen, H. D.; Jahncke, C. L., Electric Field Gradient Effects in Raman Spectroscopy. *Phys. Rev. Lett.* **2000**, *85*, 4180-4183.

39. Acevedo, R.; Lombardini, R.; Halas, N. J.; Johnson, B. R., Plasmonic Enhancement of Raman Optical Activity in Molecules near Metal Nanoshells. *The Journal of Physical Chemistry A* **2009**, *113*, 13173-13183.
40. Lee, J.; Tallarida, N.; Chen, X.; Liu, P.; Jensen, L.; Apkarian, V. A., Tip-Enhanced Raman Spectromicroscopy of Co(Ii)-Tetraphenylporphyrin on Au(111): Toward the Chemists' Microscope. *ACS Nano* **2017**.
41. Valley, N.; Greeneltch, N.; Van Duyne, R. P.; Schatz, G. C., A Look at the Origin and Magnitude of the Chemical Contribution to the Enhancement Mechanism of Surface-Enhanced Raman Spectroscopy (Sers): Theory and Experiment. *J. Phys. Chem. Lett.* **2013**, *4*, 2599-2604.
42. Lombardi, J. R.; Birke, R. L.; Lu, T.; Xu, J., Charge-Transfer Theory of Surface Enhanced Raman Spectroscopy: Herzberg–Teller Contributions. *J. Chem. Phys.* **1986**, *84*, 4174-4180.
43. Kambhampati, P.; Child, C. M.; Foster, M. C.; Campion, A., On the Chemical Mechanism of Surface Enhanced Raman Scattering: Experiment and Theory. *J. Chem. Phys.* **1998**, *108*, 5013-5026.
44. Lombardi, J. R.; Birke, R. L., A Unified Approach to Surface-Enhanced Raman Spectroscopy. *The Journal of Physical Chemistry C* **2008**, *112*, 5605-5617.
45. El-Khoury, P. Z.; Hess, W. P., Vibronic Raman Scattering at the Quantum Limit of Plasmons. *Nano Lett.* **2014**, *14*, 4114-4118.
46. Zhang, R., et al., Chemical Mapping of a Single Molecule by Plasmon-Enhanced Raman Scattering. *Nature* **2013**, *498*, 82-6.
47. Tallarida, N.; Lee, J.; Apkarian, V. A., Tip-Enhanced Raman Spectromicroscopy on the Angstrom Scale: Bare and Co-Terminated Ag Tips. *ACS Nano* **2017**.
48. Fleming, G., *Chemical Applications of Ultrafast Spectroscopy*; Oxford University Press,New York, NY: United States, 1986.
49. Zewail, A. H., Laser Femtochemistry. *Science* **1988**, *242*, 1645.
50. Frontiera, R. R.; Henry, A.-I.; Gruenke, N. L.; Van Duyne, R. P., Surface-Enhanced Femtosecond Stimulated Raman Spectroscopy. *J. Phys. Chem. Lett.* **2011**, *2*, 1199-1203.
51. Keller, E. L.; Frontiera, R. R., Monitoring Charge Density Delocalization Upon Plasmon Excitation with Ultrafast Surface-Enhanced Raman Spectroscopy. *ACS Photonics* **2017**, *4*, 1033-1039.
52. Brooks, J. L.; Frontiera, R. R., Competition between Reaction and Degradation Pathways in Plasmon-Driven Photochemistry. *The Journal of Physical Chemistry C* **2016**, *120*, 20869-20876.
53. Brandt, N. C.; Keller, E. L.; Frontiera, R. R., Ultrafast Surface-Enhanced Raman Probing of the Role of Hot Electrons in Plasmon-Driven Chemistry. *J. Phys. Chem. Lett.* **2016**, *7*, 3179-85.
54. Zhang, Y.; Zhen, Y.-R.; Neumann, O.; Day, J. K.; Nordlander, P.; Halas, N. J., Coherent Anti-Stokes Raman Scattering with Single-Molecule Sensitivity Using a Plasmonic Fano Resonance. *Nat. Commun.* **2014**, *5*, 4424.
55. Steuwe, C.; Kaminski, C. F.; Baumberg, J. J.; Mahajan, S., Surface Enhanced Coherent Anti-Stokes Raman Scattering on Nanostructured Gold Surfaces. *Nano Lett.* **2011**, *11*, 5339-5343.
56. Namboodiri, V.; Namboodiri, M.; Diaz, G. I. C.; Oppermann, M.; Flachenecker, G.; Materny, A., Surface-Enhanced Femtosecond Cars Spectroscopy (Se-Cars) on Pyridine. *Vib. Spectrosc.* **2011**, *56*, 9-12.

57. Voronine, D. V.; Sinyukov, A. M.; Hua, X.; Wang, K.; Jha, P. K.; Munusamy, E.; Wheeler, S. E.; Welch, G.; Sokolov, A. V.; Scully, M. O., Time-Resolved Surface-Enhanced Coherent Sensing of Nanoscale Molecular Complexes. *Sci. Rep.* **2012**, *2*, 891.
58. Liang, E. J.; Weippert, A.; Funk, J. M.; Materny, A.; Kiefer, W., Experimental Observation of Surface-Enhanced Coherent Anti-Stokes Raman Scattering. *Chem. Phys. Lett.* **1994**, *227*, 115-120.
59. Hayazawa, N.; Ichimura, T.; Hashimoto, M.; Inouye, Y.; Kawata, S., Amplification of Coherent Anti-Stokes Raman Scattering by a Metallic Nanostructure for a High Resolution Vibration Microscopy. *J. Appl. Phys.* **2004**, *95*, 2676-2681.
60. Ichimura, T.; Hayazawa, N.; Hashimoto, M.; Inouye, Y.; Kawata, S., Tip-Enhanced Coherent Anti-Stokes Raman Scattering for Vibrational Nanoimaging. *Phys. Rev. Lett.* **2004**, *92*, 220801.
61. Koo, T.-W.; Chan, S.; Berlin, A. A., Single-Molecule Detection of Biomolecules by Surface-Enhanced Coherent Anti-Stokes Raman Scattering. *Opt. Lett.* **2005**, *30*, 1024-1026.
62. Addison, C. J.; Konorov, S. O.; Brolo, A. G.; Blades, M. W.; Turner, R. F. B., Tuning Gold Nanoparticle Self-Assembly for Optimum Coherent Anti-Stokes Raman Scattering and Second Harmonic Generation Response. *The Journal of Physical Chemistry C* **2009**, *113*, 3586-3592.
63. Schlücker, S.; Salehi, M.; Bergner, G.; Schütz, M.; Ströbel, P.; Marx, A.; Petersen, I.; Dietzek, B.; Popp, J., Immuno-Surface-Enhanced Coherent Anti-Stokes Raman Scattering Microscopy: Immunohistochemistry with Target-Specific Metallic Nanoprobes and Nonlinear Raman Microscopy. *Anal. Chem.* **2011**, *83*, 7081-7085.
64. Yampolsky, S.; Fishman, D. A.; Dey, S.; Hulkko, E.; Banik, M.; Potma, E. O.; Apkarian, V. A., Seeing a Single Molecule Vibrate through Time-Resolved Coherent Anti-Stokes Raman Scattering. *Nat. Photon.* **2014**, *8*, 650-656.
65. Novotny, L.; Hulst, N. v., Antennas for Light. *Nat. Photon.* **2011**, *5*, 83-90.
66. Hua, X.; Voronine, D. V.; Ballmann, C. W.; Sinyukov, A. M.; Sokolov, A. V.; Scully, M. O., Nature of Surface-Enhanced Coherent Raman Scattering. *Phys. Rev. A* **2014**, *89*, 043841.
67. Dieringer, J. A.; Lettan, R. B., 2nd; Scheidt, K. A.; Van Duyne, R. P., A Frequency Domain Existence Proof of Single-Molecule Surface-Enhanced Raman Spectroscopy. *J. Am. Chem. Soc.* **2007**, *129*, 16249-56.
68. Arroyo, J. O.; Kukura, P., Non-Fluorescent Schemes for Single-Molecule Detection, Imaging and Spectroscopy. *Nat. Photon.* **2016**, *10*, 11-17.
69. Frontiera, R. R.; Gruenke, N. L.; Van Duyne, R. P., Fano-Like Resonances Arising from Long-Lived Molecule-Plasmon Interactions in Colloidal Nanoantennas. *Nano Lett.* **2012**, *12*, 5989-5994.
70. Zadoyan, R.; Kohen, D.; Lidar, D. A.; Apkarian, V. A., The Manipulation of Massive Ro-Vibronic Superpositions Using Time–Frequency-Resolved Coherent Anti-Stokes Raman Scattering (Tfrcars): From Quantum Control to Quantum Computing. *Chem. Phys.* **2001**, *266*, 323-351.
71. Klingsporn, J. M.; Sonntag, M. D.; Seideman, T.; Van Duyne, R. P., Tip-Enhanced Raman Spectroscopy with Picosecond Pulses. *J. Phys. Chem. Lett.* **2014**, *5*, 106-10.
72. Chen, C. K.; Heinz, T. F.; Ricard, D.; Shen, Y. R., Surface-Enhanced Second-Harmonic Generation and Raman Scattering. *Phys. Rev. B* **1983**, *27*, 1965-1979.
73. Danckwerts, M.; Novotny, L., Optical Frequency Mixing at Coupled Gold Nanoparticles. *Phys. Rev. Lett.* **2007**, *98*, 026104.

74. Renger, J.; Quidant, R.; van Hulst, N.; Novotny, L., Surface-Enhanced Nonlinear Four-Wave Mixing. *Phys. Rev. Lett.* **2010**, *104*, 046803.
75. Wang, Y.; Lin, C.-Y.; Nikolaenko, A.; Raghunathan, V.; Potma, E. O., Four-Wave Mixing Microscopy of Nanostructures. *Adv. Opt. Photon.* **2011**, *3*, 1-52.
76. Zhang, Y.; Wen, F.; Zhen, Y. R.; Nordlander, P.; Halas, N. J., Coherent Fano Resonances in a Plasmonic Nanocluster Enhance Optical Four-Wave Mixing. *Proc. Natl. Acad. Sci. U. S. A.* **2013**, *110*, 9215-9.
77. Gruenke, N. L.; Cardinal, M. F.; McAnally, M. O.; Frontiera, R. R.; Schatz, G. C.; Van Duyne, R. P., Ultrafast and Nonlinear Surface-Enhanced Raman Spectroscopy. *Chem. Soc. Rev.* **2016**, *45*, 2263-2290.
78. Tyler, T. P.; Henry, A.-I.; Van Duyne, R. P.; Hersam, M. C., Improved Monodispersity of Plasmonic Nanoantennas Via Centrifugal Processing. *J. Phys. Chem. Lett.* **2011**, *2*, 218-222.
79. Zeytunyan, A.; Crampton, K. T.; Zadoyan, R.; Apkarian, V. A., Supercontinuum-Based Three-Color Three-Pulse Time-Resolved Coherent Anti-Stokes Raman Scattering. *Opt. Express* **2015**, *23*, 24019.
80. Olmon, R. L.; Slovick, B.; Johnson, T. W.; Shelton, D.; Oh, S.-H.; Boreman, G. D.; Raschke, M. B., Optical Dielectric Function of Gold. *Phys. Rev. B* **2012**, *86*.
81. Malitson, I. H., Interspecimen Comparison of the Refractive Index of Fused Silica. *J. Opt. Soc. Am.* **1965**, *55*.
82. Marhaba, S.; Bachelier, G.; Bonnet, C.; Broyer, M.; Cottancin, E.; Grillet, N.; Lermé, J.; Vialle, J.-L.; Pellarin, M., Surface Plasmon Resonance of Single Gold Nanodimers near the Conductive Contact Limit. *J. Phys. Chem. C* **2009**, *113*, 4349-4356.
83. Xu, Y.-l.; Gustafson, B. Å. S., A Generalized Multiparticle Mie-Solution: Further Experimental Verification. *J. Quant. Spectrosc. Radiat. Transfer* **2001**, *70*, 395-419.
84. Yan, B.; Boriskina, S. V.; Reinhard, B. M., Optimizing Gold Nanoparticle Cluster Configurations (N </= 7) for Array Applications. *J. Phys. Chem. C Nanomater. Interfaces* **2011**, *115*, 4578-4583.
85. Wang, M.; Cao, M.; Guo, Z.; Gu, N., Generalized Multiparticle Mie Modeling of Light Scattering by Cells. *Chin. Sci. Bull.* **2013**, *58*, 2663-2666.
86. Pellegrini, G.; Mattei, G.; Bello, V.; Mazzoldi, P., Interacting Metal Nanoparticles: Optical Properties from Nanoparticle Dimers to Core-Satellite Systems. *Materials Science and Engineering: C* **2007**, *27*, 1347-1350.
87. Pellegrini, G.; Mattei, G.; Mazzoldi, P., Tunable, Directional and Wavelength Selective Plasmonic Nanoantenna Arrays. *Nanotechnology* **2009**, *20*, 065201.
88. Pellegrini, G.; Mazzoldi, P.; Mattei, G., Asymmetric Plasmonic Nanoshells as Subwavelength Directional Nanoantennas and Color Nanorouters: A Multipole Interference Approach. *The Journal of Physical Chemistry C* **2012**, *116*, 21536-21546.
89. Su, K. H.; Wei, Q. H.; Zhang, X.; Mock, J. J.; Smith, D. R.; Schultz, S., Interparticle Coupling Effects on Plasmon Resonances of Nanogold Particles. *Nano Lett.* **2003**, *3*, 1087-1090.
90. Tabor, C.; Murali, R.; Mahmoud, M.; El-Sayed, M. A., On the Use of Plasmonic Nanoparticle Pairs as a Plasmon Ruler: The Dependence of the near-Field Dipole Plasmon Coupling on Nanoparticle Size and Shape. *The Journal of Physical Chemistry A* **2009**, *113*, 1946-1953.
91. Khlebtsov, B.; Melnikov, A.; Zharov, V.; Khlebtsov, N., Absorption and Scattering of Light by a Dimer of Metal Nanospheres: Comparison of Dipole and Multipole Approaches. *Nanotechnology* **2006**, *17*, 1437-1445.

92. Jain, P. K.; Huang, W.; El-Sayed, M. A., On the Universal Scaling Behavior of the Distance Decay of Plasmon Coupling in Metal Nanoparticle Pairs: A Plasmon Ruler Equation. *Nano Lett.* **2007**, *7*, 2080-2088.
93. Yang, W. h.; Hulteen, J.; Schatz, G. C.; Van Duyne, R. P., A Surface-Enhanced Hyper-Raman and Surface-Enhanced Raman Scattering Study of Trans-1,2-Bis(4-Pyridyl)Ethylene Adsorbed onto Silver Film over Nanosphere Electrodes. Vibrational Assignments: Experiment and Theory. *J. Chem. Phys.* **1996**, *104*, 4313-4323.
94. Dey, S.; Banik, M.; Hulkko, E.; Rodriguez, K.; Apkarian, V. A.; Galperin, M.; Nitzan, A., Observation and Analysis of Fano-Like Lineshapes in the Raman Spectra of Molecules Adsorbed at Metal Interfaces. *Phys. Rev. B* **2016**, *93*, 035411.
95. Hugall, J. T.; Baumberg, J. J., Demonstrating Photoluminescence from Au Is Electronic Inelastic Light Scattering of a Plasmonic Metal: The Origin of Sers Backgrounds. *Nano Lett.* **2015**, *15*, 2600-2604.
96. Banik, M. Sers from the Point of View of the Molecule & the Antenna. Ph.D., University of California, Irvine, Ann Arbor, 2014.
97. Keldysh, L. V., Ionization in the Field of a Strong Electromagnetic Wave. *Sov. Phys. JETP* **1965**, *5*, 1307-1314.
98. El-Khoury, P. Z.; Hu, D.; Apkarian, V. A.; Hess, W. P., Raman Scattering at Plasmonic Junctions Shorted by Conductive Molecular Bridges. *Nano Lett.* **2013**, *13*, 1858-1861.
99. Banik, M.; Apkarian, V. A.; Park, T. H.; Galperin, M., Raman Staircase in Charge Transfer Sers at the Junction of Fusing Nanospheres. *J. Phys. Chem. Lett.* **2013**, *4*, 88-92.
100. Sonntag, M. D.; Klingsporn, J. M.; Garibay, L. K.; Roberts, J. M.; Dieringer, J. A.; Seideman, T.; Scheidt, K. A.; Jensen, L.; Schatz, G. C.; Van Duyne, R. P., Single-Molecule Tip-Enhanced Raman Spectroscopy. *The Journal of Physical Chemistry C* **2011**, *116*, 478-483.
101. Steidtner, J.; Pettinger, B., Tip-Enhanced Raman Spectroscopy and Microscopy on Single Dye Molecules with 15 Nm Resolution. *Phys. Rev. Lett.* **2008**, *100*, 236101.
102. Zhang, W.; Yeo, B. S.; Schmid, T.; Zenobi, R., Single Molecule Tip-Enhanced Raman Spectroscopy with Silver Tips. *The Journal of Physical Chemistry C* **2007**, *111*, 1733-1738.
103. Milojevich, C. B.; Mandrell, B. K.; Turley, H. K.; Iberi, V.; Best, M. D.; Camden, J. P., Surface-Enhanced Hyper-Raman Scattering from Single Molecules. *J. Phys. Chem. Lett.* **2013**, *4*, 3420-3423.
104. Maher, R. C.; Etchegoin, P. G.; Le Ru, E. C.; Cohen, L. F., A Conclusive Demonstration of Vibrational Pumping under Surface Enhanced Raman Scattering Conditions. *The Journal of Physical Chemistry B* **2006**, *110*, 11757-11760.
105. Maher, R. C., et al., Resonance Contributions to Anti-Stokes/Stokes Ratios under Surface Enhanced Raman Scattering Conditions. *J. Chem. Phys.* **2005**, *123*, 084702.
106. Kozich, V.; Werncke, W., The Vibrational Pumping Mechanism in Surface-Enhanced Raman Scattering: A Subpicosecond Time-Resolved Study. *The Journal of Physical Chemistry C* **2010**, *114*, 10484-10488.
107. Brolo, A. G.; Sanderson, A. C.; Smith, A. P., Ratio of the Surface-Enhanced Anti-Stokes Scattering to the Surface-Enhanced Stokes-Raman Scattering for Molecules Adsorbed on a Silver Electrode. *Phys. Rev. B* **2004**, *69*, 045424.
108. Maher, R. C.; Cohen, L. F.; Gallop, J. C.; Le Ru, E. C.; Etchegoin, P. G., Temperature-Dependent Anti-Stokes/Stokes Ratios under Surface-Enhanced Raman Scattering Conditions. *The Journal of Physical Chemistry B* **2006**, *110*, 6797-6803.

109. Pozzi, E. A.; Zrimsek, A. B.; Lethiec, C. M.; Schatz, G. C.; Hersam, M. C.; Van Duyne, R. P., Evaluating Single-Molecule Stokes and Anti-Stokes Sers for Nanoscale Thermometry. *The Journal of Physical Chemistry C* **2015**, *119*, 21116-21124.
110. Haslett, T. L.; Tay, L.; Moskovits, M., Can Surface-Enhanced Raman Scattering Serve as a Channel for Strong Optical Pumping? *J. Chem. Phys.* **2000**, *113*, 1641-1646.
111. Maher, R. C.; Galloway, C. M.; Le Ru, E. C.; Cohen, L. F.; Etchegoin, P. G., Vibrational Pumping in Surface Enhanced Raman Scattering (Sers). *Chem. Soc. Rev.* **2008**, *37*, 965-979.
112. Schmidt, M. K.; Esteban, R.; Benz, F.; Baumberg, J. J.; Aizpurua, J., Linking Classical and Molecular Optomechanics Descriptions of Sers. *Faraday Discuss.* **2017**, *205*, 31-65.
113. Banik, M.; Rodriguez, K.; Hulkko, E.; Apkarian, V. A., Orientation-Dependent Handedness of Chiral Plasmons on Nanosphere Dimers: How to Turn a Right Hand into a Left Hand. *ACS Photonics* **2016**, *3*, 2482-2489.
114. Zhang, Y.; Zhen, Y. R.; Neumann, O.; Day, J. K.; Nordlander, P.; Halas, N. J., Coherent Anti-Stokes Raman Scattering with Single-Molecule Sensitivity Using a Plasmonic Fano Resonance. *Nat. Commun.* **2014**, *5*, 4424.
115. Voronine, D. V.; Sinyukov, A. M.; Hua, X.; Munusamy, E.; Ariunbold, G.; Sokolov, A. V.; Scully, M. O., Complex Line Shapes in Surface-Enhanced Coherent Raman Spectroscopy. *J. Mod. Opt.* **2015**, *62*, 90-96.
116. Eesley, G. L., *Coherent Raman Spectroscopy*; Pergamon Press: Oxford, New York, 1981.
117. Zadoyan, R.; Apkarian, V. A., Imaging the Molecular Rovibrational Coherence through Time-Gated, Frequency-Resolved Coherent Anti-Stokes Raman Scattering. *Chem. Phys. Lett.* **2000**, *326*, 1-10.
118. Schatz, G. C.; Ratner, M. A., *Quantum Mechanics in Chemistry*; Dover Publications, 1993.
119. Silva, W. R.; Graefe, C. T.; Frontiera, R. R., Toward Label-Free Super-Resolution Microscopy. *ACS Photonics* **2016**, *3*, 79-86.
120. Schatz, G. C.; Van Duyne, R. P., *Manuscript in preparation.*
121. Latorre, F.; Kupfer, S.; Bocklitz, T.; Kinzel, D.; Trautmann, S.; Grafe, S.; Deckert, V., Spatial Resolution of Tip-Enhanced Raman Spectroscopy - Dft Assessment of the Chemical Effect. *Nanoscale* **2016**, *8*, 10229-39.
122. Trautmann, S.; Aizpurua, J.; Gotz, I.; Undisz, A.; Dellith, J.; Schneidewind, H.; Rettenmayr, M.; Deckert, V., A Classical Description of Subnanometer Resolution by Atomic Features in Metallic Structures. *Nanoscale* **2017**, *9*, 391-401.
123. Leibsle, F. M.; Dhesi, S. S.; Barrett, S. D.; Robinson, A. W., Stm Observations of Cu(100)−C(2×2)N Surfaces: Evidence for Attractive Interactions and an Incommensurate C(2 × 2) Structure. *Surf. Sci.* **1994**, *317*, 309-320.
124. Choi, T.; Ruggiero, C. D.; Gupta, J. A., Incommensurability and Atomic Structure Ofc(2×2)N/Cu(100): A Scanning Tunneling Microscopy Study. *Phys. Rev. B* **2008**, *78*.
125. Leibsle, F. M.; Flipse, C. F. J.; Robinson, A. W., Structure of the Cu{100}-C(2×2)N Surface: A Scanning-Tunneling-Microscopy Study. *Phys. Rev. B* **1993**, *47*, 15865-15868.
126. Ricart, J. M.; Torras, J.; Rubio, J.; Illas, F., Ab Initio Cluster Model Study of Geometry and Bonding Character of Atomic Nitrogen Chemisorbed on the Cu(100) and Ag(100) Surfaces. *Surf. Sci.* **1997**, *374*, 31-43.
127. Ruggiero, C. D.; Choi, T.; Gupta, J. A., Tunneling Spectroscopy of Ultrathin Insulating Films: Cun on Cu(100). *Appl. Phys. Lett.* **2007**, *91*, 253106.
128. Soon, A.; Wong, L.; Delley, B.; Stampfl, C., Morphology of Copper Nanoparticles in a Nitrogen Atmosphere: A First-Principles Investigation. *Phys. Rev. B* **2008**, *77*.

129. Yoshimoto, Y.; Tsuneyuki, S., First-Principles Study of Inter Nitrogen Interaction Energy of Cu(100)−C(2×2)N Surface. *Surf. Sci.* **2002**, *514*, 200-205.
130. Bhattarai, A.; El-Khoury, P. Z., Imaging Localized Electric Fields with Nanometer Precision through Tip-Enhanced Raman Scattering. *Chem. Commun. (Camb.)* **2017**.
131. Schneiderbauer, M.; Emmrich, M.; Weymouth, A. J.; Giessibl, F. J., Co Tip Functionalization Inverts Atomic Force Microscopy Contrast Via Short-Range Electrostatic Forces. *Phys. Rev. Lett.* **2014**, *112*, 166102.
132. Segale, D.; Apkarian, V. A., Dissipative Quantum Coherent Dynamics Probed in Phase-Space: Electronically Resonant 5-Color 4-Wave Mixing on I2(B) in Solid Kr. *J. Chem. Phys.* **2011**, *135*, 024203.
133. Lounis, B.; Bechtel, H. A.; Gerion, D.; Alivisatos, P.; Moerner, W. E., Photon Antibunching in Single Cdse/Zns Quantum Dot Fluorescence. *Chem. Phys. Lett.* **2000**, *329*, 399-404.
134. Basché, T.; Moerner, W. E.; Orrit, M.; Talon, H., Photon Antibunching in the Fluorescence of a Single Dye Molecule Trapped in a Solid. *Phys. Rev. Lett.* **1992**, *69*, 1516-1519.
135. Cheng, J.-X.; Xie, X. S., Coherent Anti-Stokes Raman Scattering Microscopy: Instrumentation, Theory, and Applications. *The Journal of Physical Chemistry B* **2004**, *108*, 827-840.
136. Min, W.; Freudiger, C. W.; Lu, S.; Xie, X. S., Coherent Nonlinear Optical Imaging: Beyond Fluorescence Microscopy. *Annu. Rev. Phys. Chem.* **2011**, *62*, 507-530.
137. Peng, J.; Pestov, D.; Scully, M. O.; Sokolov, A. V., Simple Setup for Hybrid Coherent Raman Microspectroscopy. *J. Raman Spectrosc.* **2009**, *40*, 795-799.
138. Lee, Y. J.; Parekh, S. H.; Kim, Y. H.; Cicerone, M. T., Optimized Continuum from a Photonic Crystal Fiber for Broadband Time-Resolved Coherent Anti-Stokes Raman Scattering. *Opt. Express* **2010**, *18*, 4371-4379.
139. Lee, Y. J.; Cicerone, M. T., Vibrational Dephasing Time Imaging by Time-Resolved Broadband Coherent Anti-Stokes Raman Scattering Microscopy. *Appl. Phys. Lett.* **2008**, *92*, 041108.
140. Kano, H.; Hamaguchi, H.-o., Femtosecond Coherent Anti-Stokes Raman Scattering Spectroscopy Using Supercontinuum Generated from a Photonic Crystal Fiber. *Appl. Phys. Lett.* **2004**, *85*, 4298-4300.
141. Shi, K.; Li, P.; Liu, Z., Broadband Coherent Anti-Stokes Raman Scattering Spectroscopy in Supercontinuum Optical Trap. *Appl. Phys. Lett.* **2007**, *90*, 141116.
142. Paulsen, H. N.; Hilligse, K. M.; Thøgersen, J.; Keiding, S. R.; Larsen, J. J., Coherent Anti-Stokes Raman Scattering Microscopy with a Photonic Crystal Fiber Based Light Source. *Opt. Lett.* **2003**, *28*, 1123-1125.
143. Andresen, E. R.; Paulsen, H. N.; Birkedal, V.; Thøgersen, J.; Keiding, S. R., Broadband Multiplex Coherent Anti-Stokes Raman Scattering Microscopy Employing Photonic-Crystal Fibers. *Journal of the Optical Society of America B* **2005**, *22*, 1934-1938.
144. Hans Georg, B.; Martin, W.; Rainer, B.; Marcel, K.-H.; Jürgen, L.; Maxim, E. D.; Wolfram, S.; Karsten, K., Clinical Coherent Anti-Stokes Raman Scattering and Multiphoton Tomography of Human Skin with a Femtosecond Laser and Photonic Crystal Fiber. *Laser Physics Letters* **2013**, *10*, 025604.

145. Baldacchini, T.; Zadoyan, R., In Situ and Real Time Monitoring of Two-Photon Polymerization Using Broadband Coherent Anti-Stokes Raman Scattering Microscopy. *Opt. Express* **2010**, *18*, 19219-19231.
146. Pegoraro, A. F.; Ridsdale, A.; Moffatt, D. J.; Jia, Y.; Pezacki, J. P.; Stolow, A., Optimally Chirped Multimodal Cars Microscopy Based on a Single Ti:Sapphire Oscillator. *Opt. Express* **2009**, *17*, 2984-2996.
147. Ivanov, A. A.; Alfimov, M. V.; Zheltikov, A. M., Wavelength-Tunable Ultrashort-Pulse Output of a Photonic-Crystal Fiber Designed to Resolve Ultrafast Molecular Dynamics. *Opt. Lett.* **2006**, *31*, 3330-3332.
148. Sidorov-Biryukov, D. A.; Serebryannikov, E. E.; Zheltikov, A. M., Time-Resolved Coherent Anti-Stokes Raman Scattering with a Femtosecond Soliton Output of a Photonic-Crystal Fiber. *Opt. Lett.* **2006**, *31*, 2323-2325.
149. Tu, H.; Boppart, S. A., Coherent Fiber Supercontinuum for Biophotonics. *Laser & Photonics Reviews* **2013**, *7*, 628-645.
150. Liu, Y.; King, M. D.; Tu, H.; Zhao, Y.; Boppart, S. A., Broadband Nonlinear Vibrational Spectroscopy by Shaping a Coherent Fiber Supercontinuum. *Opt. Express* **2013**, *21*, 8269-8275.
151. Dudovich, N.; Oron, D.; Silberberg, Y., Single-Pulse Coherently Controlled Nonlinear Raman Spectroscopy and Microscopy. *Nature* **2002**, *418*, 512.
152. Kumar, S.; Kamali, T.; Levitte, J. M.; Katz, O.; Hermann, B.; Werkmeister, R.; Považay, B.; Drexler, W.; Unterhuber, A.; Silberberg, Y., Single-Pulse Cars Based Multimodal Nonlinear Optical Microscope for Bioimaging. *Opt. Express* **2015**, *23*, 13082-13098.
153. Lim, S.-H.; Caster, A. G.; Leone, S. R., Single-Pulse Phase-Control Interferometric Coherent Anti-Stokes Raman Scattering Spectroscopy. *Phys. Rev. A* **2005**, *72*, 041803.
154. von Vacano, B.; Motzkus, M., Time-Resolved Two Color Single-Beam Cars Employing Supercontinuum and Femtosecond Pulse Shaping. *Opt. Commun.* **2006**, *264*, 488-493.
155. Li, H.; Harris, D. A.; Xu, B.; Wrzesinski, P. J.; Lozovoy, V. V.; Dantus, M., Coherent Mode-Selective Raman Excitation Towards Standoff Detection. *Opt. Express* **2008**, *16*, 5499-5504.
156. Furusawa, K.; Hayazawa, N.; Kawata, S., Two-Beam Multiplexed Cars Based on a Broadband Oscillator. *J. Raman Spectrosc.* **2010**, *41*, 840-847.
157. Pope, I.; Langbein, W.; Watson, P.; Borri, P., Simultaneous Hyperspectral Differential-Cars, Tpf and Shg Microscopy with a Single 5 Fs Ti:Sa Laser. *Opt. Express* **2013**, *21*, 7096-7106.
158. Pestov, D., et al., Optimizing the Laser-Pulse Configuration for Coherent Raman Spectroscopy. *Science* **2007**, *316*, 265.
159. Volkmer, A.; Book, L. D.; Xie, X. S., Time-Resolved Coherent Anti-Stokes Raman Scattering Microscopy: Imaging Based on Raman Free Induction Decay. *Appl. Phys. Lett.* **2002**, *80*, 1505-1507.
160. Lee, Y. J.; Liu, Y.; Cicerone, M. T., Characterization of Three-Color Cars in a Two-Pulse Broadband Cars Spectrum. *Opt. Lett.* **2007**, *32*, 3370-3372.
161. Hildner, R.; Brinks, D.; van Hulst, N. F., Femtosecond Coherence and Quantum Control of Single Molecules at Room Temperature. *Nature Physics* **2010**, *7*, 172.
162. Dudley, J. M.; Gu, X.; Xu, L.; Kimmel, M.; Zeek, E.; O'Shea, P.; Trebino, R.; Coen, S.; Windeler, R. S., Cross-Correlation Frequency Resolved Optical Gating Analysis of Broadband Continuum Generation in Photonic Crystal Fiber: Simulations and Experiments. *Opt. Express* **2002**, *10*, 1215-1221.

163. Newport Corporation Application Note, Supercontinuum Generation in Scg-800 Photonic Crystal Fiber. http://www.newport.com/file_store/Optics_and_Mechanics/AppsNote28.pdf
164. Nkt Photonics Application Note, Supercontinuum Generation in Photonic Crystal Fibers. http://www.nktphotonics.com/files/files/Application_note_-_Supercontinuum%20-%20General.pdf.
165. Zadoyan, R., Baldacchini, T., Carter, J., Kuo, C.-H., Ocepek, D. In *Cars Module for Multimodal Microscopy*, In SPIE BiOS, 79030Z, International Society for Optics and Photonics: 2011.
166. Herrmann, J.; Griebner, U.; Zhavoronkov, N.; Husakou, A.; Nickel, D.; Knight, J. C.; Wadsworth, W. J.; Russell, P. S. J.; Korn, G., Experimental Evidence for Supercontinuum Generation by Fission of Higher-Order Solitons in Photonic Fibers. *Phys. Rev. Lett.* **2002**, *88*, 173901.
167. Akhmanov, S. A., Vysloukh, V. A., Chirkin, A. S. , *Optics of Femtosecond Laser Pulses*; AIP-Press, 1992, p 366.
168. Bartels, A.; Heinecke, D.; Diddams, S. A., Passively Mode-Locked 10 Ghz Femtosecond Ti:Sapphire Laser. *Opt. Lett.* **2008**, *33*, 1905-1907.
169. Lozovoy, V. V.; Pastirk, I.; Dantus, M., Multiphoton Intrapulse Interference. Iv. Ultrashort Laser Pulse Spectral Phase Characterization and Compensation. *Opt. Lett.* **2004**, *29*, 775-777.